Effects of the Polymeric Binder System in Slurry-Based Three Dimensional Printing of Ceramics

by

Richard K. Holman

B.S. Materials Science and Engineering
The University of Tennessee, Knoxville, 1996

Submitted to the Department of Materials Science and Engineering in Partial Fulfillment of the Requirements for the Degree of

Doctor of Philosophy
in Ceramics

At the
Massachusetts Institute of Technology

June 2001

Signature of Author: _____
Department of Materials Science and Engineering
May 25, 2001

Certified by: _____
Professor Michael J. Cima
Sumitomo Electric Industries Professor of Materials Science and Engineering
Thesis Supervisor

Accepted by: _____
Professor Harry L. Tuller
Professor of Ceramics and Electronic Materials
Chairman, Departmental Committee on Graduate Students

Effects of the Polymeric Binder System in Slurry-Based Three Dimensional Printing of Ceramics

by

Richard K. Holman

Submitted to the Department of Materials Science and Engineering
on May 25, 2001 in Partial Fulfillment of the
Requirements for the Degree of Doctor of Philosophy
in Ceramics

ABSTRACT

The factors dictating the minimum feature size in Slurry-based Three Dimensional Printing (S-3DP^{TM}) of ceramics have been examined, focusing on effects related to the polymeric binder system polyacrylic acid (PAA, MW 60000) and its interaction with the ceramic powder bed. Methods for retrieving structures characteristic of the minimum feature, referred to as the "binder primitive," and for characterizing the size and shape of the binder primitive have been developed. Impact-related spreading of the printed binder droplets has been found to play little or no role on the primitive structure. Two dominant factors controlling primitive width were however identified. The first is wetting-induced spreading of the printed binder solution on the surface of the powder bed. The spreading process is halted prior to completion by infiltration of the printed liquid into the pore space. The role this factor plays thus depends on wetting properties and the relative rates of spreading and infiltration. The spreading and infiltration rates were modeled, and a means of predicting the maximum extent of spreading was developed. The second factor controlling minimum feature size is adsorption of the polymeric binder molecules from solution onto the surface of the ceramic particles during infiltration of the printed binder solution. This effectively filters the polymer from solution, resulting in a progressive decrease in concentration as the binder solution penetrates deeper into the pore space of the powder bed, which serves to limit the primitive size. This was confirmed via the generation of adsorption isotherms for PAA on Al_2O_3, SiO_2, and TiO_2 surfaces and correlating adsorption to measured primitive size in each of these systems, and by correlating the trend of primitive size with specific surface area of the powder in the high affinity Al_2O_3 – PAA system. A general model for predicting the combined effects of spreading and adsorption in the PAA-Al_2O_3 system was developed, and suggestions for future directions based on this research have been made.

Thesis Supervisor: Prof. Michael J. Cima

Title: Sumitomo Electric Industries Professor of Materials Science and Engineering

Table of Contents

Index of Figures

Index of Tables

For Lana, for all your love and for always being there.

Acknowledgements

First and foremost I would like to thank my wonderful wife, Lana. She has been a constant source of love, support, and inspiration, and has been understanding above and beyond the call of duty during the trying times here at MIT. I only hope that I can one day repay her.

I would like to extend my heartfelt thanks to my thesis advisor, Professor Michael Cima. His guidance and support have helped me not only accomplish my research goals, but have also helped my development as a scientist. His insights never failed to help me gain a better understanding of the complex phenomena associated with this thesis work.

I of course owe a debt of thanks to my thesis committee members. Professor Emanuel Sachs helped me to "broaden my horizons" and see things from a standpoint that otherwise wouldn't have occurred to me as a materials scientist. Special thanks are owed to Professor Richard Smith, who was very understanding and willing to come on board at such a late date.

I will always remember the good times with my fellow researcher (and great friend) Scott Uhland. We made a good team, and accomplished a remarkable amount in our work together. Thanks for the help, the advice, and the friendship (and the bachelor party).

I could not have gotten by without the help of my good friend Mike Read. He is a remarkably intelligent person, a great scientist with a keen intellect (just don't ask him about mechanical behavior). Thanks for the help, the advice, and the invaluable discussions. I'll miss the daily coffee runs together. Good luck to you in the future.

Ryan Kershner and I have developed a great friendship during my time at MIT. Thanks for all the fun times, the help and discussions, the workout sessions, the German consultations, and most importantly for being my best man.

I should also thank the other members of the 3DP™ team, who have been a tremendous resource throughout my research. In particular I wish to thank Jim Serdy, without whom 3DP™ would not be where it is today. His excitement for his work is contagious, and he is never too busy to help a student in need. My fellow students and scientists in the Ceramics Processing Research Laboratory have also been a great asset during my time at MIT. I have developed a lot of great friendships that I hope to maintain throughout my life. Thanks to Sherry Morrisette for her help and advice, to Mindy Tupper for letting me keep at least one corner of the office, to Lenny Rigione for all his help and photographic discussions, to Barbara Layne for helping me accomplish all the little things that usually get overlooked, to John Centorino for his help and practical advice, and to all the others I've failed to mention.

I would be remiss if I didn't mention all my good friends at MIT, who acted as a support structure and could always get my mind off my work. Thanks to Hartmut Rudmann, Simone Jais, Catherine Bishop, Dan Farber, Urs Schoenholzer, and Rob Bernstein. And Urs, thanks for all your advice (and of course for proofing my thesis!).

Last but not least, thanks to my parents, Roger Holman and Kay Sloan. Without you, I wouldn't even be here. I love you guys. And thanks to Carlton and Jane Collier (and of course Puddy), for taking me into your family and treating me like one of your own.

Chapter 1: Introduction

1.1 Motivation

The utilization of ceramic components in a vast number of engineering applications is limited in large part by the inability to reliably produce complex-shaped and/or fine-featured structures with high green density and a uniform microstructure using conventional forming techniques. Many traditional processes can produce only limited geometries due to the inability to produce overhanging structures or thin sections. Some also suffer from density gradients (resulting in warpage during densification) or require high polymer additive contents (leading to warpage, defects, residual carbon, etc. after burnout.) This in turn negatively affects yield, driving up costs. In the case of both structural and electronic ceramics, the microstructure often plays a critical role in the ultimate performance of the device utilizing the ceramic component. Thus high density and a uniform green structure is not only desirable but may be mandatory. Post fabrication processing (for example shaping) must also be minimized or eliminated to keep costs down. Ceramic components are often passed over due to these issues in favor of materials that are easier to fabricate (and thus less expensive), even at the cost of performance, weight etc. What is needed is a process that can produce fully dense ceramic components with fine features, high dimensional control, a uniform microstructure, and without the shape limitations of traditional forming techniques.

1.2 Traditional Ceramic Forming Techniques

The following sections outline several traditional ceramic forming techniques, with attention given to the advantages and disadvantages of each. In particular, their ability (or lack thereof) to produce high quality complex-shaped ceramic components will be addressed. Each of these processes has been reviewed extensively in the literature.[1-13]

1.2.1 Pressing

Two main types of pressing operations can be defined: uniaxial pressing and isostatic pressing. Pressure is used in both types to compact ceramic powder in a mold or die containing the powder, so that the component shape is defined by the mold or die used. Typically the stock material consists not of individual particles, but rather of large agglomerated granules of particles usually produced by spray drying, and may contain binders and plasticizers. The properties of these granules have a substantial impact on the quality of the resulting pressed component.

Dry pressing involves applying compaction pressure uniaxially to powder contained within a die. The pressure can be applied either by a single punch from the top or bottom into a stationary die, or by two punches (one on each end), each of which is free to travel within a stationary die. This process is simple and quick and can easily be automated, allowing for very high volume production. It does however suffer from a number of drawbacks. Shape complexity is severely limited due to the uniaxial nature of the pressing operation, which precludes the production of overhanging structures and necessitates relatively low height to width ratios. Non-uniform packing of the powder during filling and stress distributions during pressing due to die shape and friction with the die walls (as well as between particles) can lead to density gradients and residual stresses in the green compact. This in turn causes non-uniform shrinkage during subsequent firing operations, leading to shape distortions, residual stresses, or even cracking. Thus, highly accurate shapes may require a final machining step.

Isostatic pressing involves the application of equal pressure on all sides of the mold (i.e. isostatic pressure). This is accomplished by filling a flexible mold (i.e. a rubber bag) with the ceramic powder, evacuating and sealing the bag, and immersing it in a fluid that is then pressurized. Applying isostatic pressure eliminates one source of the density gradients found in dry pressing, but the shape complexity is still limited, particularly when internal geometries are important. The final shape accuracy of the green compact is also quite poor in general, making this process applicable for highly accurate components only when a final green machining step is planned, which in turn increases processing time and cost.

1.2.2 Injection Molding

The first step in injection molding is dispersing a ceramic powder in a polymeric matrix, or binder. Green injection molded components contain a very high polymer content, from 35 to 50% or more by volume[4]. The polymer matrix has a relatively high viscosity, so dispersion is achieved mechanically via mixing. This mixture may also contain plasticizers, lubricants, et cetera. The dispersion is heated above the softening point of the polymeric vehicle and is extruded through a gate into a chilled mold, where the polymeric matrix solidifies to form a rigid green body. Extremely complex components can be formed via injection molding, however the process has several major drawbacks. Non-uniform shrinkage during cooling or warpage during removal can result in distortion of the green body. Considerable residual stresses or cracking can occur due to the variation in cooling rate through the thickness of the section. Likewise, if the molten core of a thick section becomes sealed from the input gate by solidification, shrinkage in the core during solidification can cause residual stresses, void formation, deformation, or cracking. Weld lines may form along the intersection of two flow fronts, resulting in a flaw in the green component (and possibly leading to cracking.) The abrasive nature of the ceramic particulate phase leads to wear of the injection molding tooling, requiring expensive wear-resistant tooling and/or periodic replacement of high wear areas. The high polymer content also leads to problems at the organics-removal stage. Problems encountered during de-binding (usually via thermal degradation) include part distortion, cracking or blistering, void formation, residual carbon/char, excessively long de-binding times, etc.

1.2.3 Slip casting

Slip casting relies on the capillary extraction of the dispersing medium in a slurry through the walls of a porous (typically plaster) mold. The flow of liquid through the mold wall results in consolidation of ceramic particles at the interface, i.e. "colloidal filtration." As solvent continues to flow through the wall, the thickness of the consolidated layer grows. This continues until either the entire thickness has solidified, or until the desired thickness of

ceramic is achieved, at which point the remaining liquid slurry is poured off leaving a hollow green ceramic shell in the shape of the mold.

Typical slip casting slurries have low viscosity and high solids loading (as high as 60 vol.%.)[5] A wide particle size distribution is also necessary to achieve the extremely high solids loadings necessary for high green density and minimal casting time. The highest and most uniform densities are obtained from well-dispersed slurries. This however can lead to excessively long casting times due to the resistance to fluid flow through the cast material, particularly with fine powders and or thick sections (cast thickness increases as the square root of time.) Thus partially flocculated slurries are sometimes employed, giving faster casting times and more plastic green bodies (beneficial for final trimming), but resulting in lower density and in density gradients.[6]

The ability of slip casting to produce complex-shaped components is quite good, although drying shrinkage while still in the mold can cause cracking if the mold itself restricts shrinkage. Another major limitation is the inability to consistently produce fine features/thin sections, because they are difficult to remove from the mold without damage. Erosion of the plaster molds also limits the dimensional precision possible as well as mold life. The need for a wide particle size distribution in the slurry can lead to sedimentation effects during the long casting times required, resulting in density gradients that may lead to cracking during drying or firing. Finally, a given plaster mold can only be used to produce ~2 components per day because of casting time and the time needed to remove the absorbed water from the mold after casting.[8]

1.2.4 Tape Casting

Tape casting is a process used to form thin ceramic films by spreading a ceramic dispersion onto an impermeable substrate via a doctor blade, where it solidifies by drying. The first work was actually done on a porous substrate, however this is not the standard practice today.[9] Organic solvents are typically used to allow for rapid drying, and sufficient polymer content to give the tape strength and flexibility is required. Large, thin ceramic tapes can be formed easily, with thicknesses of 250 μm to 1 mm or more routinely produced, and films as thin as 5 μm possible.[13] Stamping of the tape after forming permits the production of

more complex 2D structures. While ideally suited to a number of electronic ceramic applications such as multi-layered capacitors, packages, inductors, and fuel cells,[13] the 2D nature of the process precludes it as an option for producing complex 3D structures. In addition, non-uniformities may be produced through the thickness of the tape as a result of drying from only one surface, resulting in deformation or cracking during sintering.

1.2.5 Green machining

Final machining of the green ceramic is often needed to achieve the necessary dimensional tolerances in ceramic components produced via the methods discussed above. While effective, green machining is still somewhat limited in the geometric complexity possible, in particular when internal structures are required. The necessity of a green machining step also adds time and cost to the production of the component (although not so much as post-fire machining, which may represent 70 to 80% of the total final cost.) [14]

1.3 Solid Freeform Fabrication

Solid freeform fabrication (SFF) techniques have been developed in an attempt to address many of the shortcomings of traditional ceramic forming techniques outlined in the previous sections. A number of SFF techniques exist, and while they vary widely in the specifics of the individual processes, they share a few common characteristics. SFF components are built up piecewise in a layer by layer manner. Individual 2D planar cross sections of the component are built and laminated consecutively, however the means of forming these layers and the methods of lamination vary. The information for these planar sections is extracted via software from a 3D CAD model of the target component, and fed to the layer-pattering control software. It should be clear that ideally this type of fabrication will allow for essentially unlimited geometrical complexity, and the resolution will in theory be limited mainly or entirely by the resolution of the layer patterning method (which may consist of laser lithography, extrusion, inkjet printing, etc.) and the layer thickness possible in a given SFF technique.

SFF techniques have so far been relegated to the role of rapid prototyping, where their utility is clear. SFF allows for the quick and cheap production of working models for

visualization, which is useful for planning, design, sales, etc. Where prototypes may have traditionally taken weeks or longer to prepare (and required expensive new tooling, CNC machining, or much manual labor), SFF techniques allow a turnaround of as little as one day, with existing equipment, working from no more than a 3D CAD model. This can be particularly useful in research and development, where mock-ups of a proposed system can be examined, analyzed, fit together with other components of the system, etc. allowing the identification of potential problems before the installation of expensive production facilities and tooling.

SFF is now however attempting to make in-roads into a new area, i.e. manufacturing. While SFF techniques may never compete with traditional methods for large, high volume components of static design, SFF can make an impact in a number of areas: geometrically complex components impossible via conventional techniques; when traditional techniques cannot produce the required microstructural properties (e.g. high uniform density, complex compositional gradients, etc.); and when frequent design changes would require expensive new tooling and long delays, among others. Most SFF techniques also allow various materials and multiple components to be produced on the same piece of equipment, with little or no modifications. The next few sections outline a number of the most well developed SFF techniques for ceramics and examine their specific advantages and limitations.

1.3.1 Stereolithography (SLA)

A schematic of a "stereolithography apparatus," or SLA, is shown in Figure 1.1. Stereolithography was one of the first SFF techniques developed. In the ceramics variant, a bath containing a suspension of ceramic particles in a UV-curable monomer serves as the source material. Solids loading is typically 50-60% by volume.[16] An individual 2D cross section is traced out on the surface of the bath with a laser based on data extracted from the solid CAD model, crosslinking the resin in the shape of the component section. To add structural integrity and avoid migration of the layer/component in the liquid bath, a support structure (which must later be removed) is also formed; this is particularly important when overhanging structures are required.[17] The completed layer is then lowered into the bath by one layer thickness (typically 150-200 μm[16]), and a knife edge is passed over the component

to ensure coverage of the component with the fluidic build material and a uniform layer thickness. The next layer is then scanned with the laser, with the cured thickness controlled by the laser power (but affected by particle size and solids loading.)[16] The laser power is chosen to get good stitching between layers. The cured component is removed from the vat upon completion of all layers. The large content of polymer resin must at this point be removed prior to final sintering.

While SLA can produce surface finish equal to or better than any other SFF process, it has a number of major drawbacks, in addition to the aforementioned need for support structures. The UV-curable monomers used can be quite toxic and may be expensive.[18] The high polymer content (as much as 60 vol.%) presents challenges at the organics removal stage, as discussed in the section on injection molding. Warpage of the green components can also be an issue, as is the high complexity of the equipment required.[19]

1.3.2 Laminated Object Manufacturing (LOM)

Laminated object manufacturing involves the lamination of cohesive layers of material, which are cut to shape via a laser. A schematic of the process is shown in Figure 1.2.[20] The build material was originally paper, and as such allowed only conceptual models. The process has since been expanded to ceramics by using green tape cast ceramic layers (typically ~55 vol.% ceramic) as the build material. To build an LOM component, the layer of green ceramic tape is rolled out onto a substrate. A laser then cuts the contour of the perimeter of the component based on data extracted from the 3D CAD file, defining the layer geometry. The surrounding (non-component) material is also sliced into cubes to facilitate later removal. This can be a decided advantage compared to stereolithography, since the non-component material acts as a support for overhangs and thin sections. Removal of this material however represents an additional manual step and can be difficult when internal structures/cavities are involved.

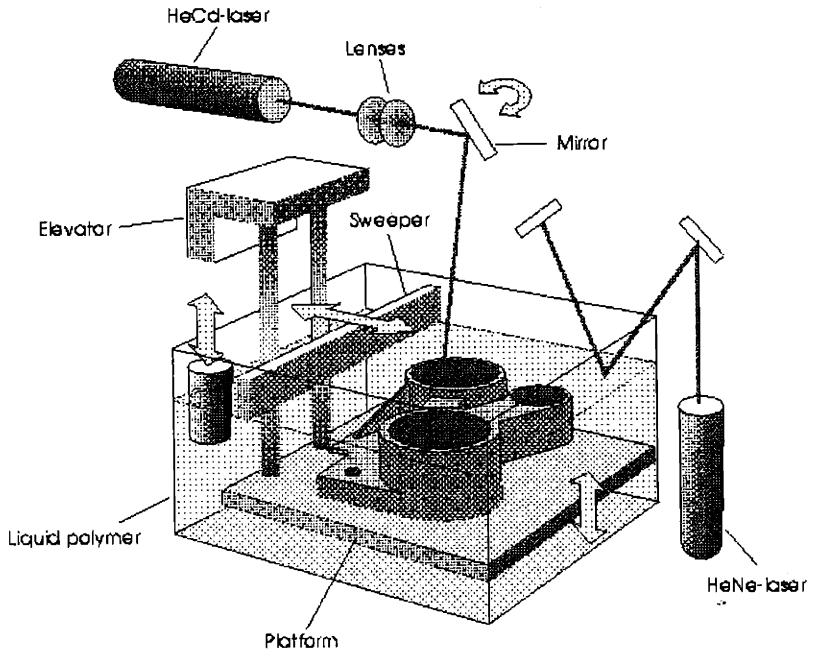

Figure 1.1: Schematic of the stereolithography apparatus, or SLA.[15]

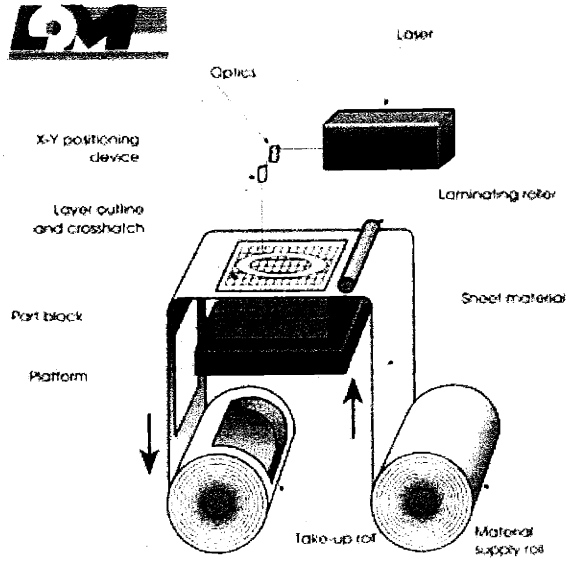

Figure 1.2: Schematic of the Laminated Object Manufacturing (LMO) process.[20]

The next layer of ceramic tape is then rolled out, and lamination to the previous layer is achieved by heating and light pressure; application of a solvent to the previous layer prior to rolling out of the new layer has also been practiced to reduce problems with lamination between layers.[21] The laser then cuts the next cross section into the layer. The laser cuts only the current layer, so high part complexity is possible.[22] This process is repeated until the entire component has been produced.

LOM has a number of processing issues that may limit its applicability for high quality, fine ceramic components. Lamination defects between layers have proven to be problematic.[18,19] This has required the use of a post-processing step wherein quasi-isopressing of the finished green component is carried out in a bed of powder during an initial binder burnout step.[21,23] Final binder burnout is carried out as a separate step, followed by sintering. The component layers are made of green tape cast ceramic, and as such LOM suffers from the same binder burnout issues as tape casting. Poor surface finish and difficulty with hollow components are also issues.[19]

A closely related process to LOM is Computer-Aided Manufacturing of Laminated Engineering Materials, or CAM-LEM, shown schematically in Figure 1.3. The key difference is that the layers are cut *prior* to lamination, rather than after. This allows the removal of interior material prior to stacking, facilitating the formation of complex interior channels and cavities, and angling of the laser to produce smoother contours.[19,25] This of course means that a support material is required for overhanging structures, typically in the form of an organic "fugitive" material that is later burned out.[25] Burnout of the binder from the green ceramic tape remains an issue as well. The system also requires a robotic system capable of accurately registering layers during the stacking process.

1.3.3 Fused Deposition Modeling (FDM)

Fused Deposition Modeling involves the deposition of a molten ceramic-loaded polymer filament along a path defined by the control software. The bead of molten material is extruded from a nozzle and quickly solidifies to form a rigid filament. The extrusion head traces the perimeter of the cross section of the component in a vector motion, followed by a raster fill of the interior.[26] The next layer of the component is then

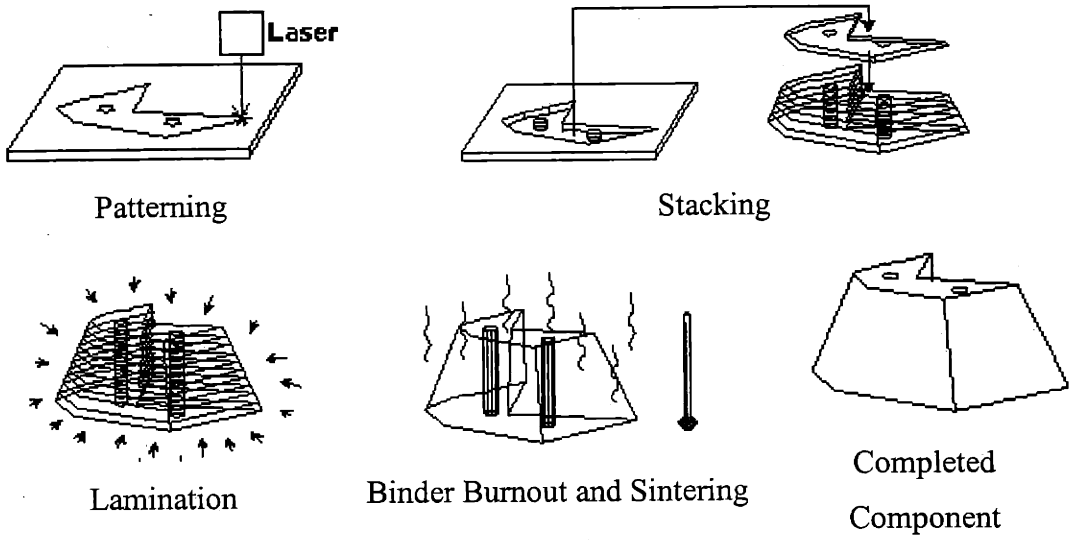

Figure 1.3: Schematic of the CAM-LEM process.[24]

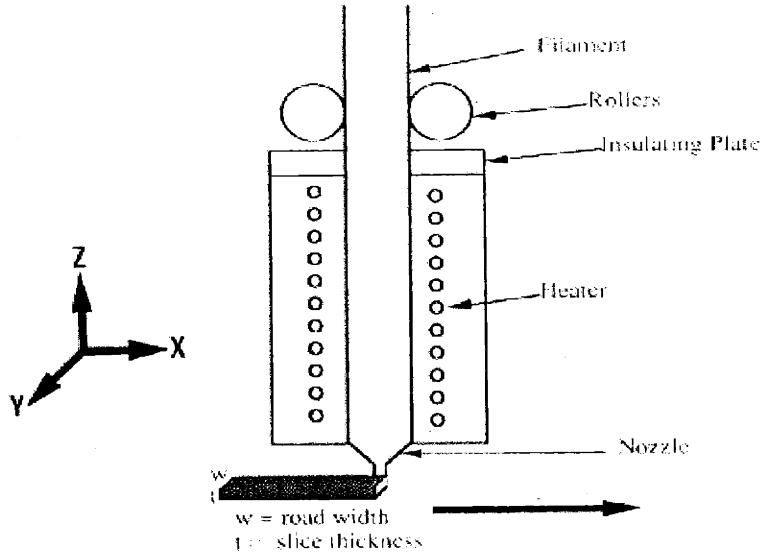

Figure 1.4: Schematic of the FDM filament extrusion head.[27]

deposited, etc., until the entire component has been formed. The stock material is a polymer mixture containing a high volume fraction of ceramic particles (~55 vol.%), as well as plasticizer, wax to modify viscosity, and a "tackifier" to improve bonding to previously deposited passes and layers.[19,26] The extrusion head is illustrated schematically in Figure 1.4.

The FDM process deposits only the material necessary to form the component, i.e. there is no waste material. This does however preclude the formation of large overhangs, unless some sacrificial second material is deposited in the cavities to act as a support material. The resolution of this process is also greatly limited, as the extruded bead is typically ~1.8 mm in diameter.[17,19,26] The high polymer content adds the associated problems at the binder burnout stage.[18] The ultimate sintered densities of FDM components are also somewhat low for many technical ceramic applications (~97-98% of theoretical.)[19,26,28]

1.3.4 Selective Laser Sintering (SLS)

Selective laser sintering involves scanning a laser over the surface of a bed of loose powder, drawing the image of the cross-section of the component under construction. The laser energy causes localized heating, fusing the particles together and as such forming a 2D layer of the component. The component is then lowered by one layer thickness, a new layer of powder is spread, and the process is repeated until the entire component is formed. This is illustrated schematically in Figure 1.5. Initially implementing polymer particles, the process has been extended to ceramics by using polymer coated ceramic particles as feed material.[18,19,22] Low melting ceramic or metal additives have also been used as the binding material.[29,30] The un-fused powder surrounding the component acts as support material, allowing overhangs to be constructed.

SLS unfortunately suffers from a number of critical drawbacks. The fired components have very low density owing to the use of loose powder as the stock material. Final densities of 53-65% of theoretical have been reported (in the absence of subsequent HIP'ing or infiltration treatments.)[19,28] The surface finish of SLS components is also inferior to a number of other SFF processes because of the unintentional sticking of powder in the boundary region to the fused component.[17,19]

1.3.5 *Three Dimensional Printing (3DP™):*

The Three Dimensional Printing Process, or 3DP™, is a SFF technique developed at MIT. Two main variants exist, differing only in the method of layer formation: the traditional 3DP™ process, and the slurry-based 3DP™ process, which is the subject of this thesis. The traditional 3DP™ process (Figure 1.6) uses a vibrating roller to spread loose powder from a reservoir over a piston in order to form a layer. A 2D image of the component cross-section is extracted from a 3D CAD file, and a binder is printed into the loose powder layer in the image of this 2D section by what is essentially an inkjet printhead. This locally binds the particles only in the region of the component, while the surrounding un-printed material acts as a support structure for thin sections and overhangs. The piston on which the part rests is then lowered, a new layer of powder is deposited, and the next 2D section is printed, etc. until the entire component has been built. The completed part is then removed from the bed of loose powder and extraneous powder is blown away.

This technique is quite versatile, having been used to create polymer, metal, and ceramic components with a wide range of binder systems, including polymers (solutions and suspensions), colloidal silica, etc.[32,33,34,35,36] The spreading of dry powder to form layers allows for simple and rapid layer formation and quick component retrieval, however it unfortunately also places some severe limitations on the process. Only rather large particles or agglomerates can be used[37,38] (typically ~20 or 30 μm), as small particles (~1 μm or less) do not flow well due to van der Waals interaction between the particles, making them difficult to spread. The green density of parts made by dry spreading of layers is also quite low (typically ~34% of theoretical with ceramic systems.)[32] These conditions may be satisfactory for a number of applications (e.g. porous casting moulds, or where infiltration or some other post processing can be employed for densification), however they preclude the use of the dry powder process for the vast majority of performance ceramic components where high density (~99% of theoretical), defect free monolithic structures are required. A high green density

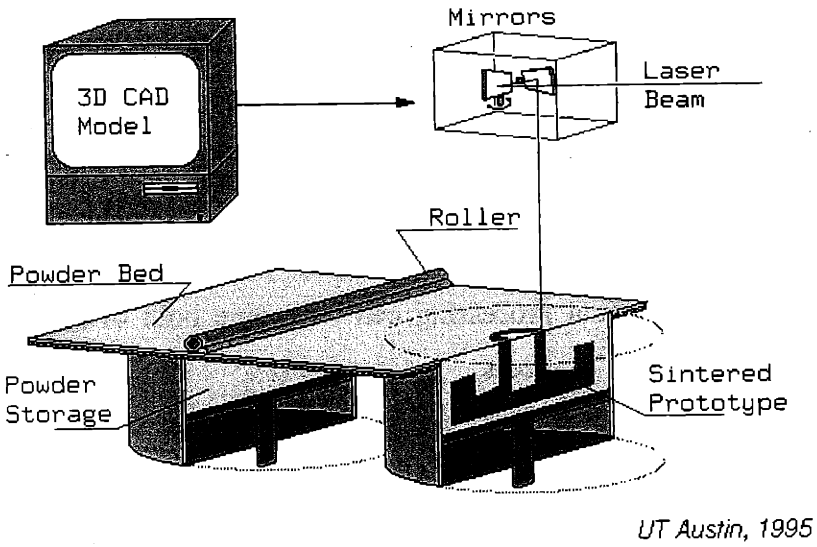

Figure 1.5: Schematic of the SLS process.[31]

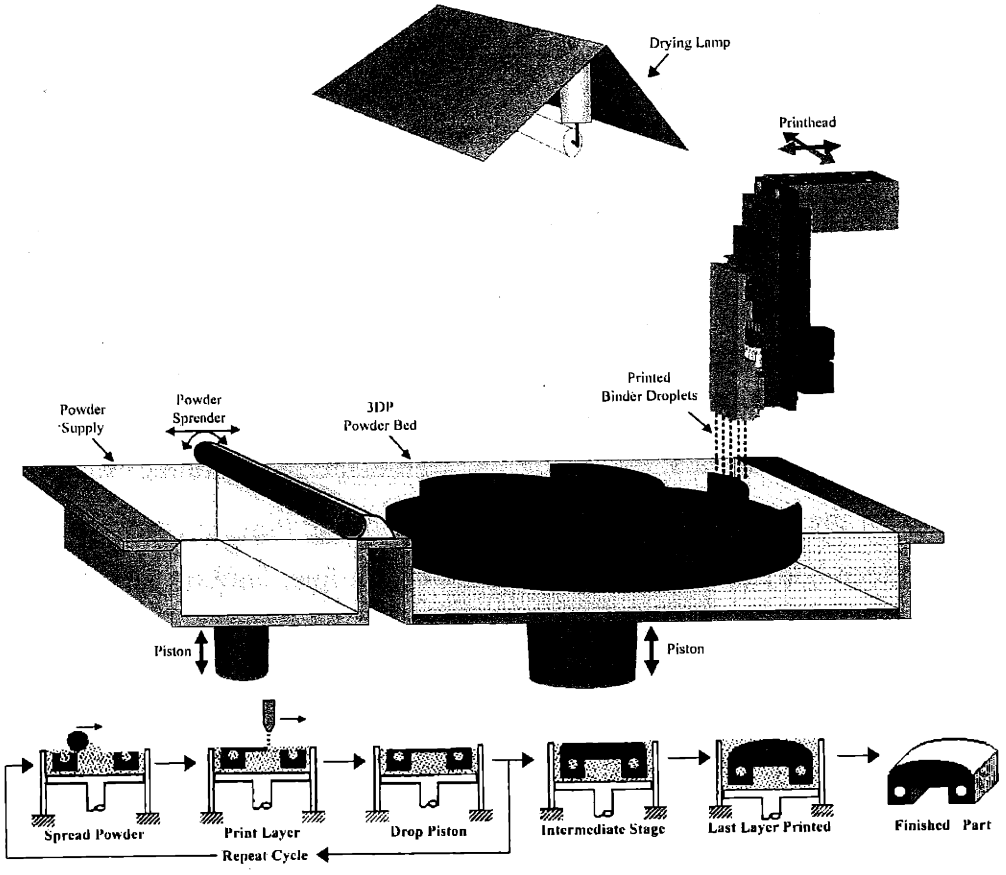

Figure 1.6: Schematic of the traditional (dry-powder) 3DP™ process.

and a micron-scale particle size are necessary to directly fire a green body to near-theoretical density with no large pores.[39,40,41] Micron-scale particles are advantageous because of their higher specific surface energy, which is the driving force for sintering; fine particles also result in shorter distances over which atoms must diffuse during densification, leading to more rapid sintering rates, known as the "scaling law."[42] Low green density can also result in thermodynamically stable large pores, which can be strength limiting defects in structural ceramics. The use of colloidal processing can overcome both of these limitations of the traditional (dry powder) 3DP™ process.

1.3.6 Slurry-Based Three Dimensional Printing

The slurry-based 3DP™ process was developed to overcome the shortcomings of the traditional process in the formation of ceramic components, namely to produce uniform, high density green components composed of micron-scale particles capable of being fired to full density from the green state in a single firing step with no intermediate processing. Colloidal processing puts this goal within reach.[8,43]

Colloidal processing involves the stabilization of a dispersion of particles (in this case ceramic) in a liquid medium. Particles are small (typically $\propto 1$ μm) to minimize settling/sedimentation, which requires rather large inter-particle repulsive forces to minimize flocculation. These forces are either electrostatic due to charges developed on the particle surfaces, steric due to adsorption of polymers on the particle surface, or a combination of the two (stabilization with polyelectrolytes.) The repulsive forces also allow for considerable rearrangement during consolidation/casting in well-dispersed ceramic slurries, and the capillary forces on the particles upon casting and drying provide further densification. The result can be a green body in excess of 60% dense with a fine, uniform microstructure under proper processing conditions. Colloidal processing has in recent years been incorporated into the 3DP™ process at the layer formation stage, the result being the slurry-based 3DP™ process, or S-3DP™.

S-3DP™ has been described in detail by Grau,[44] and is shown schematically in Figure 1.7. Individual green layers are formed by rastering a jet of ceramic slurry (typically ~30 vol.% ceramic in a water or water-alcohol vehicle) over a substrate. The individual jetted

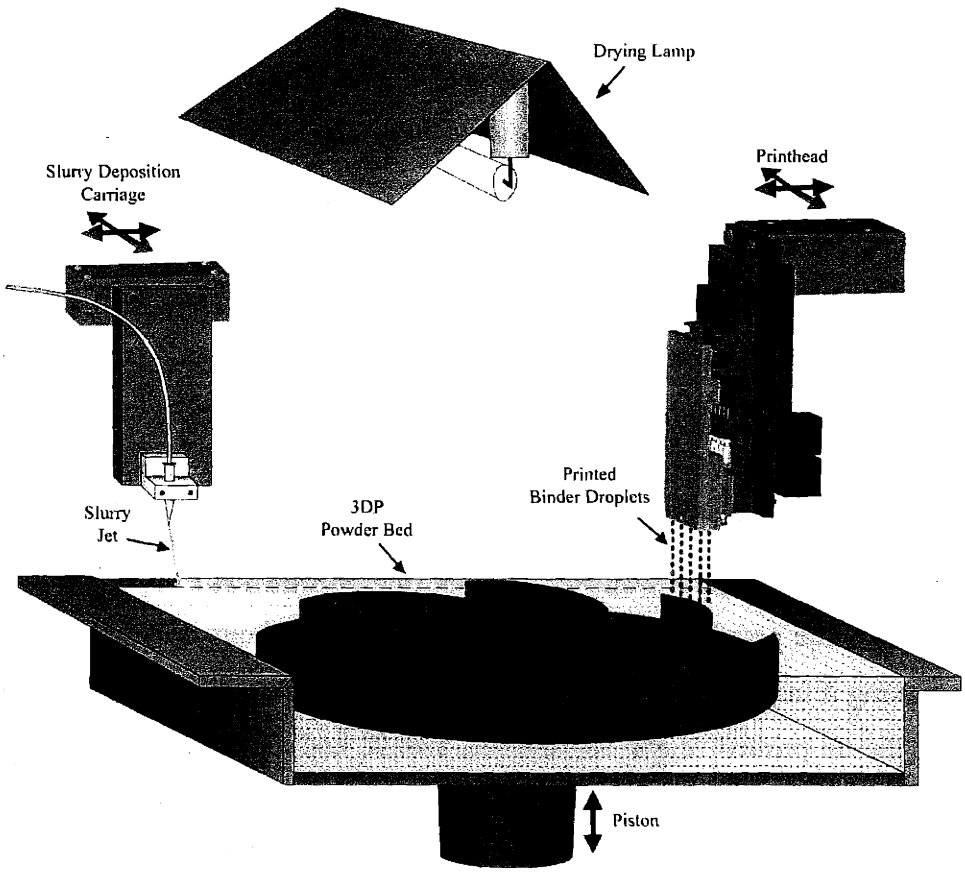

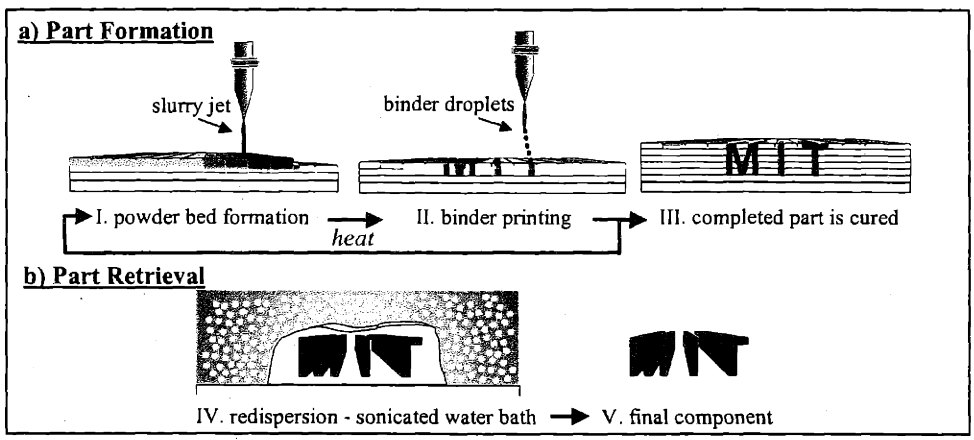

Figure 1.7: Schematic of the Slurry-Based 3DP™ (S-3DP™) Process.

beads slip cast and stitch to one another and to the previous layer. The green layer thickness is determined by the slurry solids loading, the volumetric flow rate of slurry, the spacing between raster lines, and the cast (green) density of the layer. A drying step removes the excess solvent/dispersing medium. The binder printing step is then carried out and is identical to that used in traditional (dry powder) 3DP™. The surrounding green powder bed acts as a support structure for thin sections and overhangs, as in traditional 3DP™. The S-3DP™ process has been used to form uniform layers from 10 to 100μm thick, of Al_2O_3, TiO_2, SiO_2, Si_3N_4, $BaTiO_3$, WC/WC-Co, and Ag, using particles from 0.3 to 2 μm, and with green densities in excess of 60% of theoretical. The binder system currently used is a solution of polyacrylic acid, PAA (MW 60000), from 2 to 5 vol.%, either aqueous or in ethanol. Glycerol is added to the solution as a crosslinker. The printed green components are contained in the slip cast block of green ceramic (the powder bed) upon completion of the building process. The powder bed is heated to 150°C for an hour in Argon to crosslink the PAA, thus making it insoluble. The entire block is then submersed in water (or in some cases ethanol), and the un-printed region redisperses, swells, and sloughs off, leaving the printed component. Polyethylene glycol (PEG, MW 400) is added to the ceramic slurry to aid in this redispersion process. Minor sonication removes any residual powder contained in internal structures.

This modification of the 3DP™ process has allowed for the production of green components with high density and uniform microstructures, resulting in high quality, fully dense fired components, as seen in Figure 1.8 and Table 1.1. However a major stumbling block to its widespread application still exists, namely the minimum feature size possible. The push in much of the ceramics industry, and in particular electronic ceramics, is for miniaturization, with ever-stricter requirements on resolution. The minimum feature size in S-3DP™, on the other hand, has been ~320 μm or larger in the print plane. The goal of this thesis is to develop an understanding of the processes which control the size and shape of the S-3DP™ building block, and in turn use this knowledge to develop a strategy for improving resolution in the S-3DP™ process.

1.4 Structure of Thesis

The remainder of this thesis examines the processes involved in defining the minimum feature size in S-3DP™. Chapter 2 introduces the binder "primitive," the primary building block in S-3DP™ and discusses the processes that could be dominant in determining its size and shape. Chapter 3 examines the role of droplet impact on the ultimate structure of the primitive. Several theoretical models of impact are presented, and the feasibility of controlling the primitive width by controlling impact is discussed. Chapter 4 examines the balance between spreading of the liquid on the powder bed surface and the rate of solution infiltration into the powder bed. Chapter 5 explores chemical adsorption processes that occur during infiltration with some combinations of polymeric binder and ceramic surface; these processes can have a huge (and heretofore unexpected) effect on primitive size and shape. Chapter 6 contains a summary of the results of this thesis work and suggestions for the future.

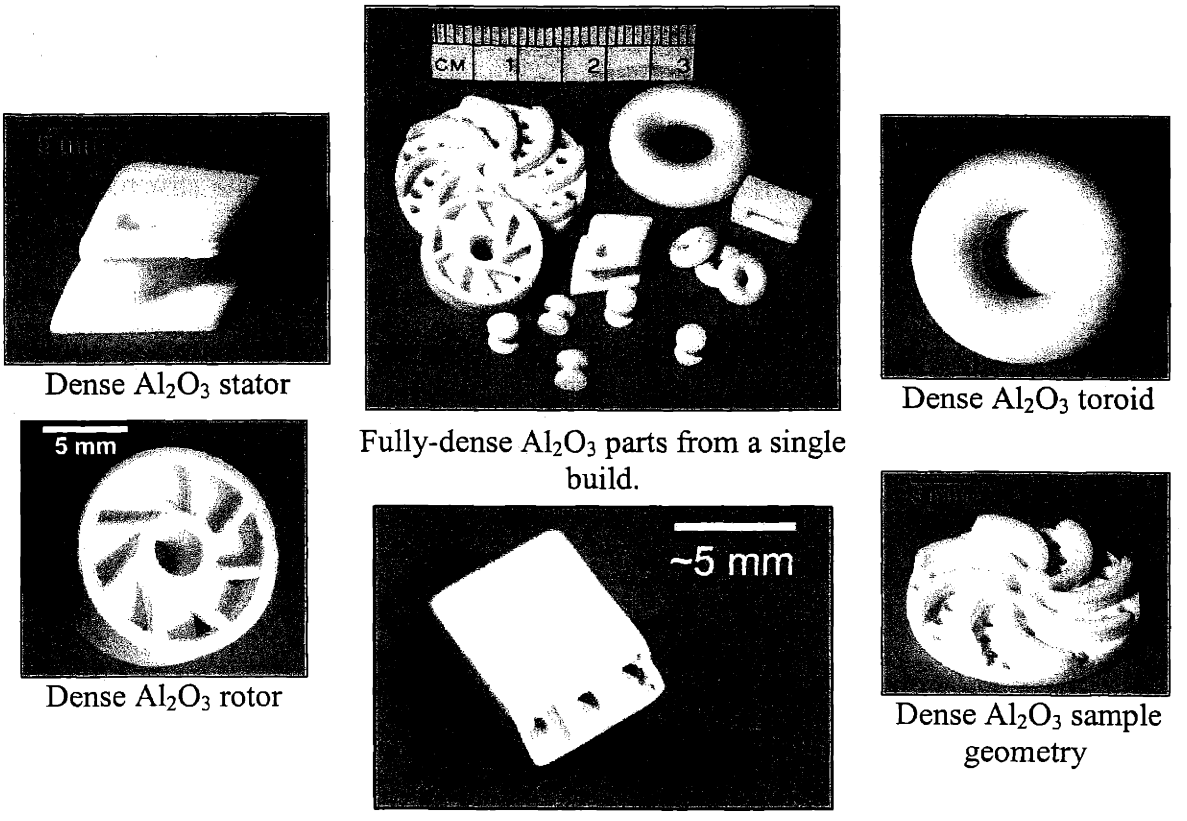

Figure 1.8: Examples of S-3DP™ components.

Property	Value
Particle Size (μm)	0.3 - 2
Green Layer Height (μm)	20 - 100
Green Density	50 - 61%
Fired Density	98 - >99%
Linear Shrinkage on Firing	17 – 19 %

Table 1.1: Properties of green and fired S-3DP™ components.

Chapter 2: The Binder Primitive, Building Block of a 3DP™ Component

The primary building block in components produced by 3DP™ is the binder line primitive, or simply the primitive. It is defined as the structure formed in a green S-3DP™ powder bed when a single bead of overlapping droplets of binder solution is deposited and infiltrates. This chapter introduces the binder primitive and discusses its effect on resolution in S-3DP™. The first section outlines methods for binder deposition. This is followed by a discussion of primitive formation and the role of the primitive in determining resolution and surface finish. The last section examines a real-world case where knowledge of the primitive size allowed tailoring of process parameters to improve surface finish in a target S-3DP™ component.

2.1 Binder Deposition Methods

Deposition of the binder solution in 3DP™ is by one of two methods: continuous jet (CJ) printing or droplet-on-demand (DoD) printing. These methods vary both in the manner in which droplets are formed and in the parameters of the printing process (print rate, droplet velocity, etc.) A description of these two printing styles (as used in 3DP™) is presented next, followed by a discussion of the binder line primitive and its characterization.

2.1.1 Continuous Jet Printing

Continuous jet printing gets its name from the fact that a continuous stream of binder solution is utilized. The electrically grounded solution passes through a ruby orifice and is broken up into droplets at the Rayleigh frequency by piezo action; the amplitude of the agitation is chosen such that break-off of the stream into individual droplets occurs within the length of the charging cell (Figure 2.1a.) The droplets then pass between the plates of the deflection cell, across which a high potential is applied (~700-1000 V DC.) Deposition is turned on and off by selectively charging and deflecting the droplets into a catcher assembly, as follows. Zero potential is applied to the charging cell when the printhead is in the "on" state; the droplets remain uncharged and as such pass unperturbed through the field emanating from the deflection plates and strike the powder bed. When the printhead is in the "off" state

(i.e. no binder should be deposited), a potential is applied to the charging cell (~110 V DC.) This drives free charges from the segment of the stream that has entered the charging cell (the stream is still contiguous, and so remains grounded), producing a net charge on the solution. Droplet break-off then occurs within the cell, resulting in droplets with a net charge. These are then deflected by the field across the deflection plates into a catcher system that pumps the binder into a reservoir located off the printhead for recovery. The standard 40 μm orifice results in ~80 μm droplets traveling at 9-10 m/s, although droplets as small as 50 μm have been produced reliably with a 30 μm orifice.

The CJ method has the advantage of rapid printing rates, reliability, and simplicity of operation. The continuous stream of droplets (typically formed at 25-60kHz) results however in relatively large printhead traverse speeds (~1.5m/s) to keep the volume of binder solution deposited at the desired level. CJ printing is thus in general suitable only for raster-style printing (Figure 2.1b.) Tracing of the section outline (vector style printing), which would result in smoother perimeters, is precluded by the high accelerations that would be produced when turning corners at 1.5m/s. This in turn limits the shape accuracy possible along component faces not parallel to the axis of printhead travel (roughness and "stair stepping" occur because of the finite spacing between raster passes.) A large degree of droplet overlap occurs because of the high droplet generation rate, so that the printed liquid behaves more like a continuous bead of liquid rather than individual discreet droplets. Almost all S-3DP™ components to date have been formed using CJ printing.

2.1.2 Droplet-on-Demand Printing

Droplet-on-demand printing involves the generation of a droplet of binder solution only when needed (hence the name.) DoD is only now being implemented in S-3DP™. The MIT DoD head is shown in Figure 2.2a. A droplet is ejected from this printhead by applying a voltage across the thickness of a piezo-ceramic tube, causing it to contract, or "squeeze", an interior tube within which the binder solution passes. This pressure pulse results in the ejection of a single droplet of binder solution from the orifice. The current orifice size is 70 μm, however the droplet size is controlled by the waveform and duration of the voltage pulse

applied to the piezo. Droplets as small as 50 μm in diameter have been successfully produced using this printhead.

The ability to control the droplet generation rate allows low printhead traverse speeds to be used. This in turn allows the adoption of a vector-style of printing, wherein the perimeter of the section being printed is traced, followed by a raster-style fill of the interior (Figure 2.2b). This can result in smoother edges (in the layer plane) by eliminating the stair stepping found on faces not parallel to the axis of travel in CJ printing. Variable traverse speeds are also possible (higher when travelling in a straight line, slower when negotiating a turn.) The droplet generation rate is unfortunately currently so low for reasons of jet stability (limited to ~1kHz), that very low print speeds relative to CJ printing must be used to deposit sufficient binder solution. The printed droplets also behave more like discreet droplets (rather than a continuous bead of liquid as in CJ printing) because of the low generation rates.

2.2 Binder Primitive Size and Shape

It has been stated earlier that the binder line primitive represents the building block in a S-3DP™ component, and as such is a measure of the resolution in S-3DP™. A complete S-3DP™ component can be viewed as an array of single line primitives stitched together to make a cohesive structure (Figure 2.3). It is apparent that the size and shape of this primitive will ultimately determine the minimum feature size obtainable in the X, Y, and Z directions, as well as the surface finish of the component walls, all of which are critically important in making fine ceramic components such as microwave frequency filters for telecommunications, which have been a recent focus of work performed in conjunction with TDK USA Corp., and have features ~500 μm in size.

Typical line primitives have been quite large, ~320-350 μm wide x ~35-40 μm thick in Al_2O_3 beds with a particle size of 1 μm (nominal, HPA 1.0, Ceralox) resulting in an aspect ratio (width to height) of nearly 10, as seen in Figure 2.4. Smaller primitives are required if very small features are to be produced, and a more spherical primitive may be desirable at times to improve the surface finish of vertical walls while keeping the layer thickness

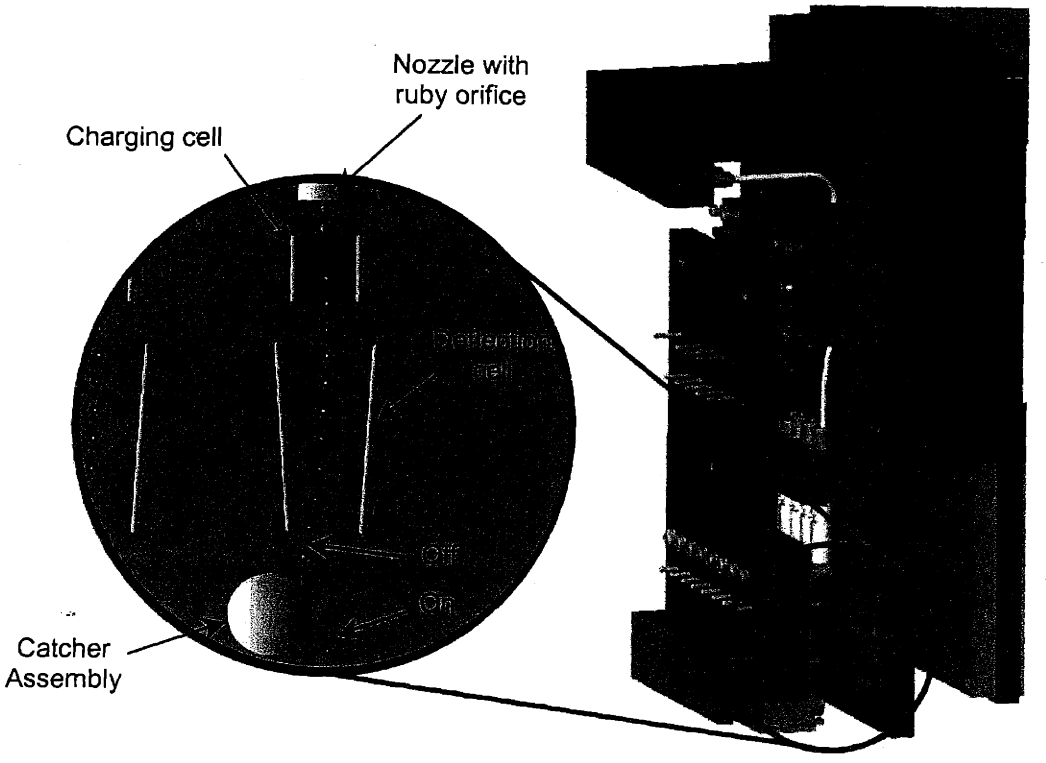

a.)

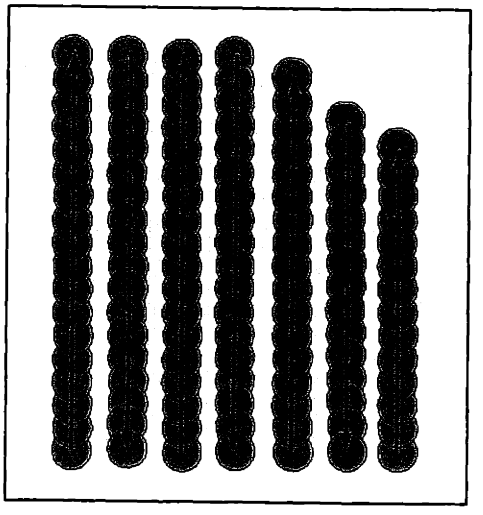

b.)

Figure 2.1: Schematics of a.) the 3DP™ continuous jet printhead and b.) droplet placement in the associated raster-style of printing.

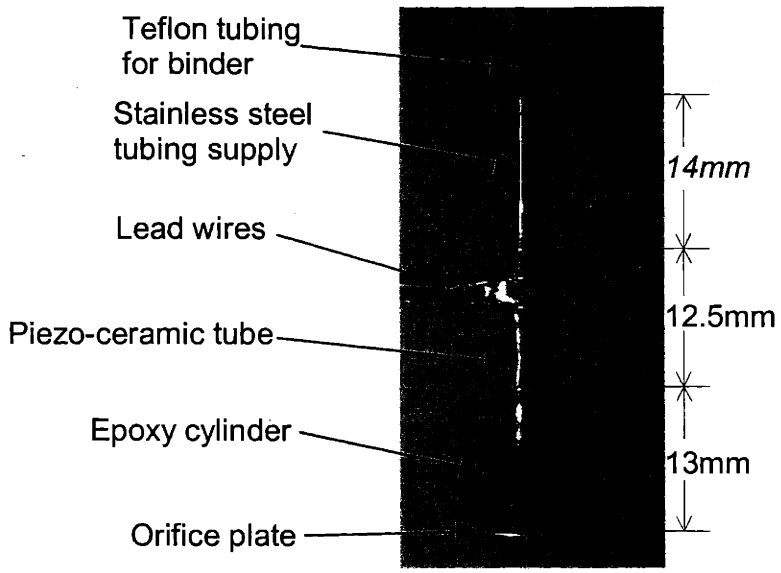

a.)

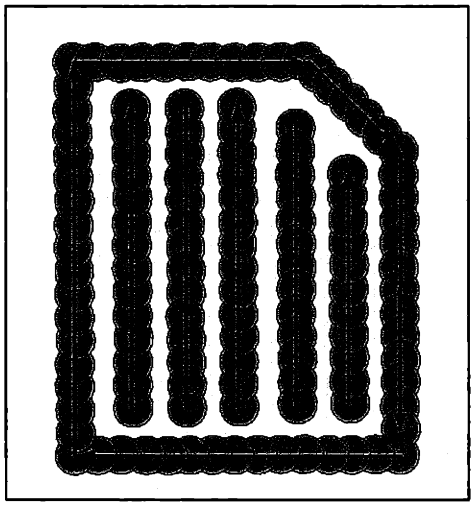

b.)

Figure 2.2: a.) The MIT DoD printhead and b.) droplet placement in the associated vector style of printing (with raster fill). (Photo courtesy H. Tsuchiya)

manageably large. The advantage of improving resolution (i.e. decreasing the minimum feature size) is obvious. S-3DP™ must keep up with the drive to finer features occurring in a variety of fields (most notably electronic ceramics.) Surface finish is equally important for reasons illustrated schematically in Figure 2.5. Surface roughness can (and often does) represent the strength-limiting factor in structural ceramic bodies (Figure 2.5a.) A smooth surface is essential for fit and where a seal is necessary when the component must be incorporated into a larger system in both electronic and structural applications (Figure 2.5b.) Surface roughness can be especially detrimental to electronic ceramics when metallization is to be applied to the surface (Figure 2.5c); the added current path and scattering result in increased losses.

It thus becomes important to determine what physical and chemical processes are the controlling factors in determining primitive size (width and height), which naturally determines the primitive shape, above and beyond simply decreasing the amount of binder deposited. Knowledge of the key parameters could allow not only the ultimate minimization of the primitive size when the limits of the deposition techniques have been reached, improving resolution in the S-3DP™ process, but could also allow the tailoring of the primitive shape to produce the optimum structure for a given geometry or application.

2.2.1 Previous Work

A considerable amount of work has been done in examining the binder deposition process in 3DP™. The majority has dealt however with printing into loose powder beds[47] (i.e. the traditional loose powder spreading 3DP™ technique), where ballistics are a major focus of the work. This is not an issue in the S-3DP™ process because of the cohesive nature of the powder bed. V. Knezevic examined primitives in cohesive slip cast powder beds.[48] His work focused on the effects of droplet generation frequency and droplet overlap on the size and profile of a primitive. T. Arthur studied primitive size in spray-deposited powder beds (the slurry is essentially "air-brushed" onto the substrate to form a layer.)[49] Her work was mainly concerned with droplet velocity and binder dose (the amount of binder solution deposited per unit length, as described later in this chapter). J. Grau examined layer

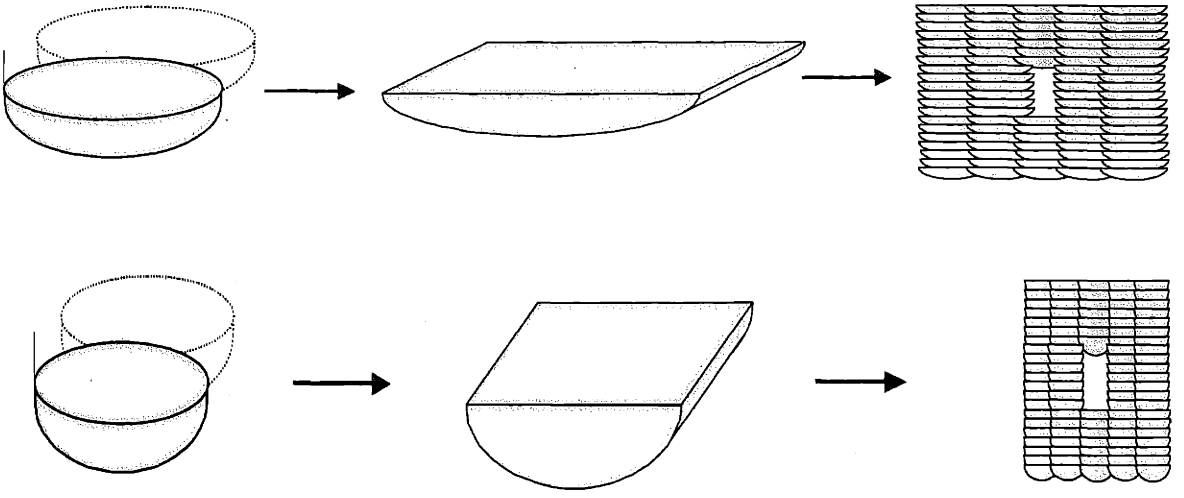

Figure 2.3: Schematic of high (top) and low (bottom) aspect ratio single line primitives (in cross section) and a component made up of primitives.

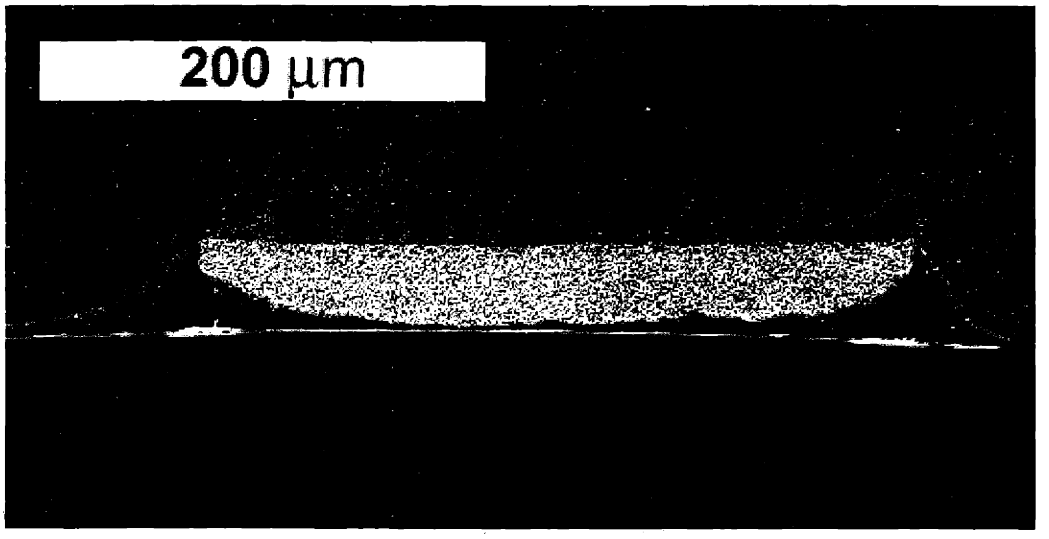

Figure 2.4: Cross section of a green single line primitive (2.4 vol.% PAA 60000 solution in nominally 1μm Al_2O_3, Ceralox HPA 1.0) in an epoxy matrix; the raster direction is into the page.

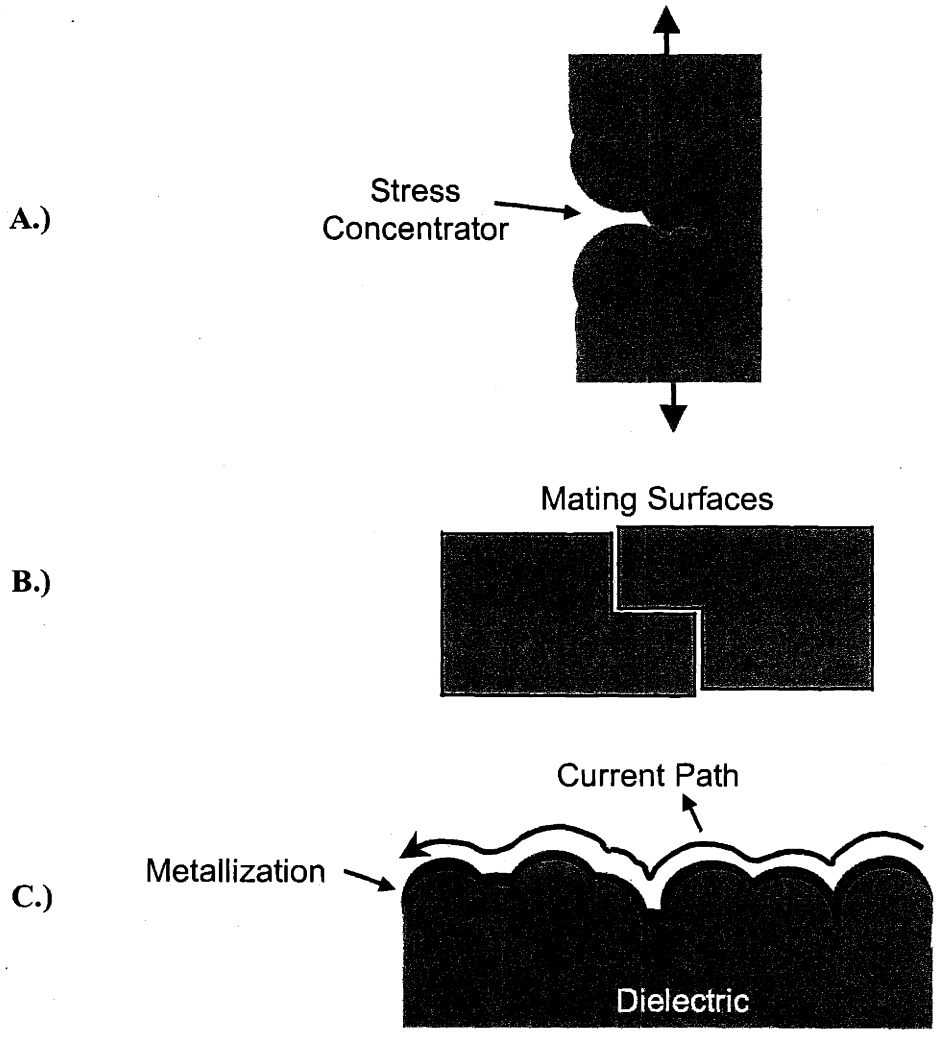

Figure 2.5: Surface roughness issues in ceramic components (see text for description).

formation, interactions between the binder and subsequently deposited ceramic slurry, and a number of binder systems and their infiltration kinetics.[44] S. Uhland determined the physical and chemical processes involved in the redispersion process in S-3DP™.[39] This allowed him to tailor the slurry formulation to optimize redispersion, making the retrieval of printed primitives much easier and more reliable. This work has laid an excellent foundation upon which to build, however, much remains before the factors affecting the binder deposition and infiltration processes can be fully understood and used to tailor the printing process to produce a given primitive structure.

2.2.2 Binder Primitive Formation

The process of primitive formation can be thought of in three stages (which may or may not be separate to varying degrees), as represented schematically in Figure 2.6a. First, the binder droplets impact the surface of the powder bed and dynamically spread, or "splat." The droplets may hit a bead of just-deposited binder solution or a dry powder bed surface depending on what printing regime (droplet generation rate and printhead traverse speed) is utilized (Figure 2.6b.) The former is characteristic of CJ printing, while DoD printing can conceivably work in either regime. The impact process occurs in a time scale on the order of micro-seconds.[45,46] Spreading or de-spreading can then occur (unless the impact splat width happens to correspond to the equilibrium spreading width given by the contact angle.) The third stage is infiltration of the printed liquid into the porous powder bed, and all the processes involved therein. This stage has been observed to be on the order of 10's of milliseconds in 1 μm Al_2O_3 powder beds, which is corroborated by Grau[44]. Determining which of these processes is the dominant factor controlling the shape and size development of the binder primitive in different printing regimes (or if all play a hand in the final shape), as well as understanding which variables are important in each process and why, will allow an informed tailoring of the binder and slurry chemistries and printing conditions to produce the desired primitive structure.

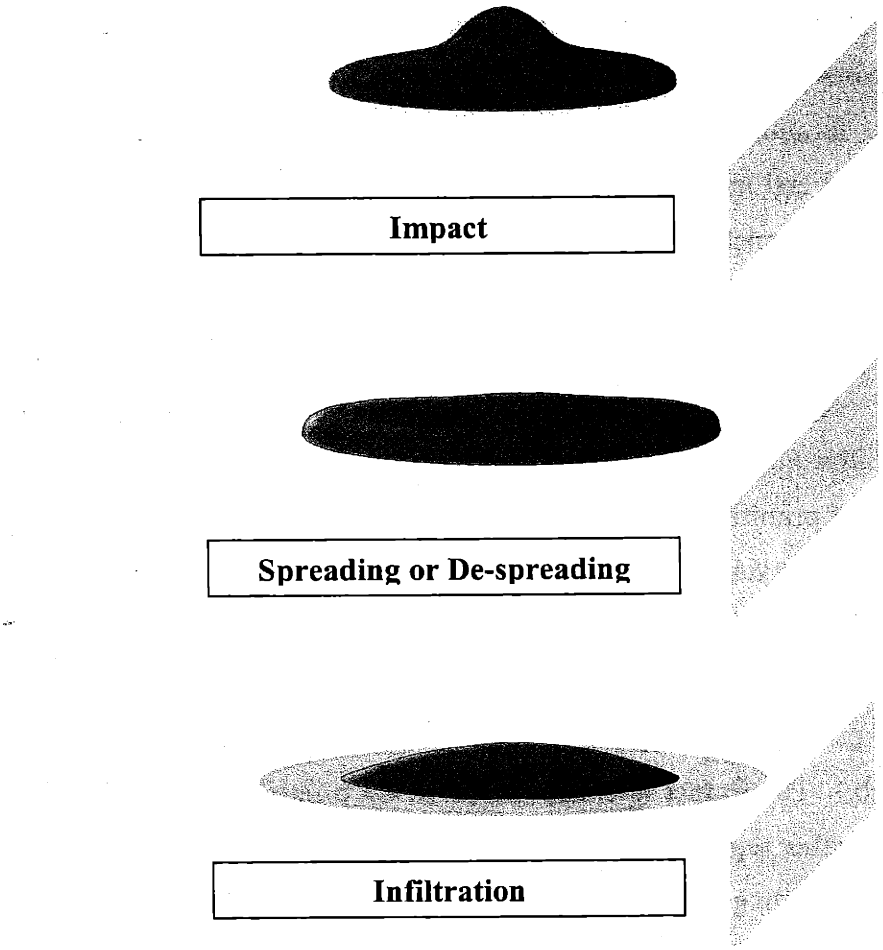

a.)

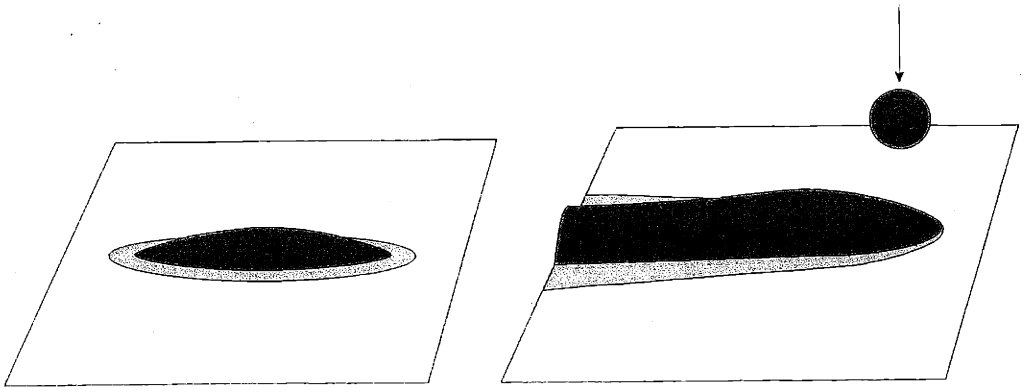

b.)

Figure 2.6: Schematic representation of a.) the stages of droplet deposition and b.) isolated drop versus multiple drop deposition.

2.2.3 *Experimental Procedure for Primitive Analysis*

The procedure for characterizing the primitive structure (size and shape) is as follows. Primitives are formed by printing a single raster line of binder solution under a given set of conditions into an S-3DP™ green powder bed. Table 2.1 contains a list of standard printing conditions used in these studies for continuous jet printing of line primitives into S-3DP™ Al_2O_3 powder beds. The primitives are then cured using the standard process outlined in Chapter 1. Redispersion is carried out in de-ionized water. The powder bed swells and is washed away with a stream of DI water. The redispersed primitives are then transferred from the substrate onto a screen. Any remaining powder or redispersed slurry is washed away through the screen, again with a stream of DI water. The primitives are transferred to an absorbent surface (a paper towel) and dried in an oven at ~80°C for 20 minutes. A support block is then prepared by coating a sample-mounting clip with a thin layer of quick cure epoxy. Short sections of the primitives (~1cm in length) are mounted one by one onto the clip using a small, sharp-pointed probe (slightly moistened at the tip to allow capillary action to hold the primitive in place). The primitives are mounted such that the printing direction is perpendicular to the edge of the clip. Twelve primitives per printing condition are typically mounted to ensure that at least ten survive to give a reasonable average of the dimensions. The block and primitives are mounted in a low viscosity infiltrating epoxy under vacuum, with the primitives oriented perpendicular to the surface (i.e. in cross section.) The cured mount is then polished to a 1μm diamond finish.

The cross-sectioned primitives are examined in a scanning electron microscope. Images are captured and are analyzed using image analysis software (ImageTool for Windows v. 2.00, from the University of Texas Health Science Center in San Antonio, TX.) The width is measured, and the thickness is taken from an average of five equally spaced points across the primitive. The cross sectional area is then taken as a measure of the primitive volume (volume per unit length.) For a given set of conditions, 10 primitives are examined in this way and the results are averaged.

2.2.4 *Primitive Size Quantification and Comparison*

Comparisons of primitive cross sectional area are given conveniently in terms of a "primitive saturation ratio," which compares the primitive cross section to some ideal value based on liquid volume and available pore space (i.e. the packing fraction of the green powder bed). This in turn facilitates comparisons between systems or particle sizes where small green density variations may occur. The "ideal" saturation of 100% represents the case where the printed solution infiltrates and just fills the available pore space. The actual primitive saturation may be less than 100% due to fingering/drainage of the solution through the pore space, so that the pore space is not completely filled with liquid (resulting in a primitive cross section that is larger than the "ideal" primitive), or greater than 100% because of the effects of chemical interactions between the polymer and ceramic (which will be examined in depth in Chapter 5.)

The amount of binder deposited is given in terms of the "binder dose," which is the volume of binder deposited per unit print length, i.e. the liquid cross section *prior* to infiltration. Binder dose is given by the following equation:

$$A_B = \frac{Q}{V} \qquad \text{Eqn. 2.1}$$

where:

A_B = binder dose

Q = volumetric flow rate of the binder solution

V = binder printhead raster speed

Dividing the binder dose by the pore fraction in the powder bed gives the volume per unit length of powder bed that would be necessary to *just fill* the available pore space with liquid at a dose A_B. The primitive saturation is then simply the ratio of this volume per unit length to the actual primitive cross sectional area (volume per unit length.) Primitive saturation is thus given by the following equation:

$$S_P = \frac{A_B}{A_P \bullet X_p} \bullet 100\% \qquad \text{Eqn. 2.2}$$

Nominal Alumina Particle Size (μm):	1
Slurry Solids Loading (vol.%):	30
Slurry Flow Rate (g/min):	4.1
Slurry Deposition Raster Speed (cm/s):	150
Slurry Raster Line Spacing (μm):	250
Green Layer Thickness (μm):	55
Binder Solution Solids Loading (vol.%):	2.4
Binder Solution Flow Rate (cm^3/min):	0.65
Binder Printhead Raster Speed (cm/s):	150
Binder Droplet Diam. (μm, with 40 μm nozzle):	80
Binder Dose (μm^2):	7270

Table 2.1: Typical operating parameters used in continuous jet S-3DP™ of Al_2O_3.

where:

S_P = primitive saturation

A_p = actual cross sectional area of the primitive

X_p = pore fraction in the primitive/powder bed

It is upon the basis of primitive saturation that meaningful comparisons between print runs and materials systems will be made throughout this thesis.

2.2.5 Case Study - Practical Implications Beyond Resolution

Comparisons of saturation and size are useful from a scientific standpoint when characterizing the processes that dictate primitive structure (which constitutes the bulk of this thesis), but the actual size numbers are also invaluable from a practical standpoint. The individual primitives making up a printed component must overlap sufficiently in the X-Y plane to form a cohesive layer, and in the Z-direction to prevent delamination of layers in the component. In addition, simply selecting a layer height that gives enough overlap for stitching may be inadequate; minimization of the effects of primitive shape (i.e. the rounded edges) is desirable if the optimum surface finish is to be obtained (as represented schematically in Figure 2-3.) Greater overlap of the primitives helps to mask the discreet nature of the primitives by decreasing the undercut produced by the rounded edges. An ill-advised selection of printing parameters (such as spacing between binder lines or layer height) can result in a rough surface in the best case, or a component that completely falls apart upon redispersion in the worst case. Thus printing parameters must be tailored based on information gathered from the examination of actual primitives, as has been demonstrated in the case of $BaTiO_3$-based microwave frequency filters built in collaboration with TDK USA Corp.

Figure 2.7 contains a schematic of the target RF filter. Dimensional requirements are clearly strict, and surface roughness must be minimized to remain within tolerances and to minimize losses in operation. The material is called MR2, a proprietary $BaTiO_3$-based material developed by TDK Corp. for the production of these filters. The primitive thickness was found to be ~150 μm in MR2 (much thicker than in typical Al_2O_3 beds.) The working

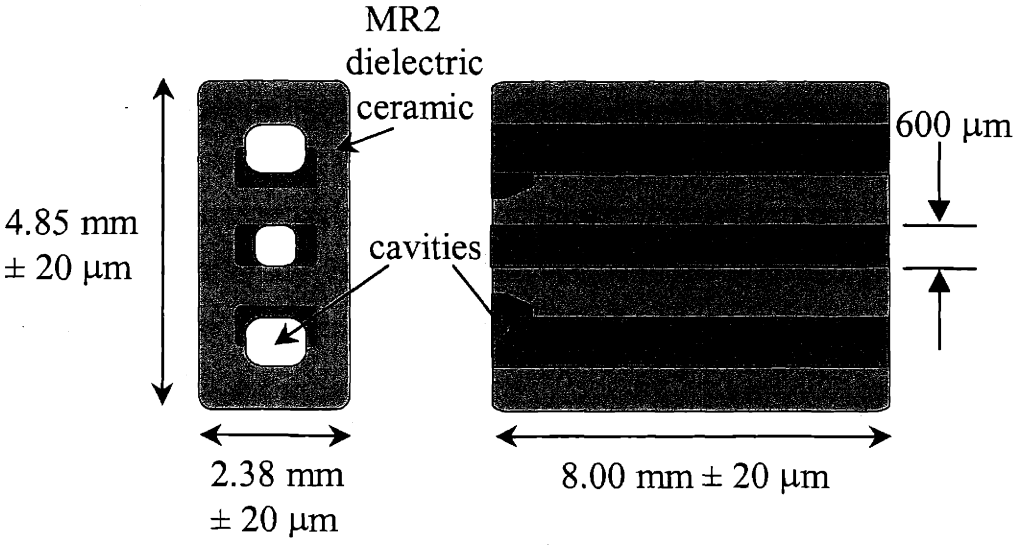

Figure 2.7: Schematic of the microwave frequency band pass filter.

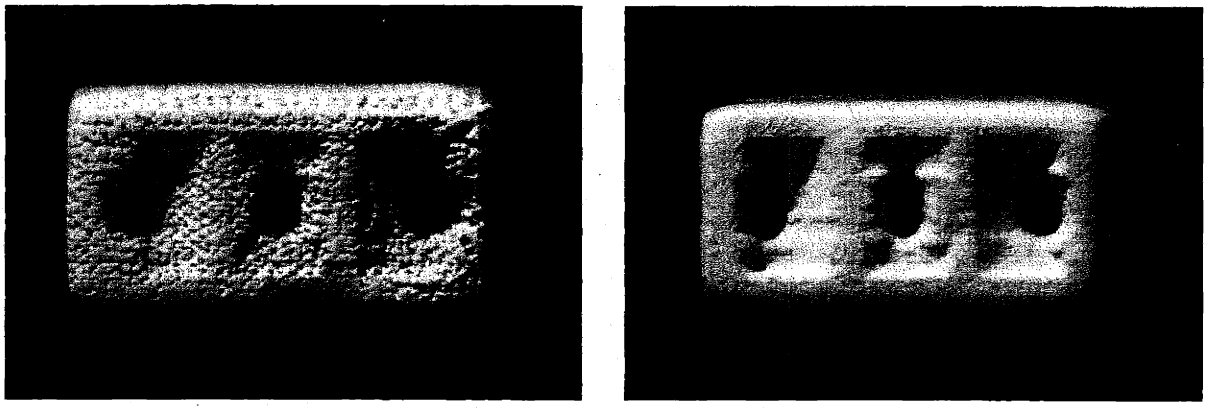

Figure 2.8: Green S-3DP™ microwave filters produced with a layer height of a) 80 μm and b) 55 μm.

green layer thickness was then set at 80 μm based on this information. This resulted in sufficient stitching between layers to produce green printed filters strong enough to survive retrieval and subsequent handling. The surface finish however was unacceptable, as seen in Figure 2.8a. The reason for this can be traced to the shape of the primitive. Insufficient overlap allowed the tapered edge geometry of the primitive to be realized in the final surface of the component; the roughness is essentially the individual primitives emerging from the surface. The layer thickness was therefore decreased to 55 μm (less than half the primitive thickness). The increased layer-to-layer primitive overlap resulted in a vast improvement in surface finish, as seen in Figure 2.8b.

Chapter 3: Droplet Impact

Droplets of binder solution formed by CJ printing in S-3DP™ travel at ~10 m/s. This necessitates consideration of the impact of the droplet with the substrate and the resulting dynamic spreading and splashing as a possible factor affecting the width of binder primitives. A number of models that attempt to predict impact behavior (extension of the liquid upon droplet impact) are examined in this chapter. Actual liquid extension is then examined on both dense substrates and on S-3DP™ powder beds under various conditions, and conclusions about the role of impact in determining primitive width are made. The width of the liquid extension in turn has an indirect effect on primitive depth.

3.1 Models of Droplet Impact

A number of researchers have looked at the impact of droplets with a rigid surface.[45,46,50] Models of the extension of the liquid upon impact invariably involve two dimensionless parameters, the impact Reynolds number (Re) and the Weber number (We):

$$Re = \frac{\rho U d}{\eta} \qquad \text{Eqn. 3.1}$$

$$We = \frac{\rho U^2 d}{\gamma} \qquad \text{Eqn. 3.2}$$

where:

ρ = liquid (binder solution) density

U = droplet velocity

d = droplet diameter

η = liquid viscosity

γ = liquid surface tension

The Reynolds number is a dimensionless ratio relating the inertial energy of the droplet to the viscous losses, while the Weber number similarly relates inertial energy to surface energy.

The parameter that is often examined is the "ratio of spreading", $\frac{D^*}{d}$, where

D^* = maximum diameter of "splat" upon completion of impact

d = initial droplet diameter (before impact)

The ultimate result is that essentially four parameters control the impact: solution viscosity, droplet velocity, droplet mass, and solution surface tension. The droplet velocity and mass contribute to its kinetic energy and so higher values favor greater extension on impact; the viscosity of the solution serves to damp some of the kinetic energy, and so retards the liquid extension; and the added energy of forming new liquid surface also restricts the extension. This is examined in detail in the following two sections.

3.1.1 Model of Asai et al.

Asai et al. report in their study of ink droplets impacting paper that the ratio of spreading is *entirely dependent* on Re and We, irrespective of surface (they experimented with copy paper, bond paper, and plastic film.)[45] The study examined droplets from 44 to 81 μm in diameter traveling at 2.5 to 20 m/s, with viscosities from 2.0 to 7.5 cP, and surface tensions between 50 and 54 dyne/cm (similar to the conditions encountered in 3DP™.) They use a correlation formula to predict the ratio of spreading assuming the droplet spreads to a disk of maximum diameter D^* and minimum height h^*, the impact surface is flat and level, and the contact angle is 90°. From the balance of energy and volume before and after impact,

$$\frac{\pi\rho d^3 U^2}{12} + \pi\gamma d^2 = E_k + F_k + \gamma S^* \qquad \text{Eqn. 3.3}$$

$$S^* = \frac{\pi D^{*2}}{4} + \pi D^* h^* \qquad \text{Eqn. 3.4}$$

$$\frac{\pi d^3}{6} = \frac{\pi D^{*2} h^*}{4} \qquad \text{Eqn. 3.5}$$

where:

E_k = kinetic energy after impact/spreading, assumed to be zero

F_k = energy dissipation during impact (viscous losses)

S^* = surface area of droplet at maximum extension (assumes a cylindrical disk of diameter D^* and height h^*)

The terms on the left side of Eqn. 3.3 are the kinetic energy of the droplet and the surface energy of the droplet prior to impact, respectively. The terms on the right side are the kinetic energy after impact (zero), the viscous losses during extension of the liquid, and the surface energy after impact. Eqn. 3.5 is simply conservation of volume, i.e. the droplet volume before impact is equal to the cylindrical disk volume after impact. They then make the simplifying assumption that $1<\frac{D^*}{d}<3$ (limiting the range of impact conditions for which the model will be applicable), resulting in the following:

$$\frac{S^*}{\pi d^2} \approx 1 + 0.36\left(\frac{D^*}{d} - 1\right)^2 \qquad \text{Eqn. 3.6}$$

$$\frac{D^*}{d} \approx 1 + 0.48We^{0.5}X \qquad \text{Eqn. 3.7}$$

where:

$$X \equiv \left[1 - \frac{E_k + F_k}{\pi\rho d^3 U^2/12}\right]^{0.5} \qquad \text{Eqn. 3.8}$$

They further assume that X has the form:

$$X = e^{-aWe^b Re^c} \qquad \text{Eqn. 3.9}$$

The values of a, b, and c were determined empirically, yielding the following correlation formula for the ratio of spreading:

$$\frac{D^*}{d} = 1 + 0.48We^{0.5}e^{-1.48We^{0.22}Re^{-0.21}} \qquad \text{Eqn. 3.10}$$

Table 3.1 shows typical values of the pertinent variables under operating conditions found in ceramics 3DP™. Substituting these values into Eqn. 3.10 results in a ratio of spreading of 2.36, giving a maximum splat diameter D* of 190 μm for an initial droplet diameter of 80 μm. It is important to point out that this is for a single droplet, whereas in continuous jet 3DP™ many droplets overlap. Thus, a complete theory must account for the fact that all but the first droplet hit previously deposited liquid. A transition to DoD printing could however facilitate single droplet printing (where the previous droplet has fully infiltrated before the subsequent drop impacts the powder bed), for which the above model will be a more accurate representation. This model should in any case allow prediction of the trends expected when varying the pertinent parameters involved. Figures 3.1 a–d illustrate how the splat diameter varies as a function of the viscosity, surface tension, droplet velocity, and droplet size, respectively as predicted by Eqn. 3.10. It should also be pointed out that while the initial development assumes a contact angle of 90°, Eqn. 3.10 was empirically fit to data having contact angles less than 90° by Asai et al. Of particular interest is the fact that their results for impact width appeared to be independent of the actual surface onto which was printed, producing comparable results on plain paper, coated paper, and plastic film.

3.1.2 Model of Chandra and Avedisian

Chandra and Avedisian used n-heptane in their study of droplet impact and were largely concerned with the effect of temperature.[46] Their experiments were at a fixed droplet velocity of 0.93 m/s, a Weber number of 43, and an impact Reynolds number of 2300 (quite far from the conditions encountered in slurry-based ceramics 3DP™, as seen in Table 3.1.) They again determine the ratio of spreading, which they term β, based on a pre- and post-impact energy balance ($\beta = D/d$, while $\beta_{max} = D^*/d$, where D is the instantaneous diameter of the spreading liquid disk, and D* is the maximum value as described previously in this section.) The kinetic and surface energies prior to impact are the same as used by Asai et al. above (terms 1 and 2, respectively, on the left side of Eqn. 3.3.) The kinetic energy after impact at D* is assumed to be zero (the liquid has stopped moving), and the surface energy after impact is given as follows:

$$E_{S2} = \frac{\pi D^{*2} \gamma}{4}(1 - \cos\theta) \qquad \text{Eqn. 3.11}$$

where θ is the contact angle of the liquid; the surface energy of the solid before impact has been subtracted from both sides of the energy balance and the surface area at the edges of the "disk" has been neglected in arriving at Eqn. 3.11. The inaccuracy of the surface area assumption could be considerable if the droplet is not relatively flat after impact (by a factor of two in the limit of a hemispherical cap). The energy dissipated by viscous losses, F_k, is approximated as

$$F_k = \int_0^{t_c} \int_V \phi dV dt \approx \phi V t_c \qquad \text{Eqn. 3.12}$$

where ϕ is a dissipation factor given by

$$\phi = \eta\left(\frac{\partial v_i}{\partial x_j} + \frac{\partial v_j}{\partial x_i}\right)\frac{\partial v_i}{\partial x_j} \approx \eta\left(\frac{U}{h}\right)^2 \qquad \text{Eqn. 3.13}$$

and

V = volume

t = time

h = height of spreading liquid

v_i = velocity component in direction i

t_c = time scale of the impact

The partial derivatives in Eqn. 3.13 represent shear in the various directions, and the lateral velocity of the liquid front is assumed to equal the initial downward droplet velocity. t_c is approximated as the time taken for the droplet to move from a height $h = d$ to $h = 0$, so that

$$t_c \approx d/U \qquad \text{Eqn. 3.14}$$

Jet Velocity (m/s)	9
Surface Tension γ (N/m)	0.072
Smooth surface Contact Angle θ	30
Viscosity η (Pa-s)	0.0025
Binder Density ρ (kg/m^3)	1010
Droplet Diameter (μm)	80
Pore Radius (μm)	0.7
Impact Re	291
We	91

Table 3.1: Typical values of parameters encountered in S-3DP^{TM}.

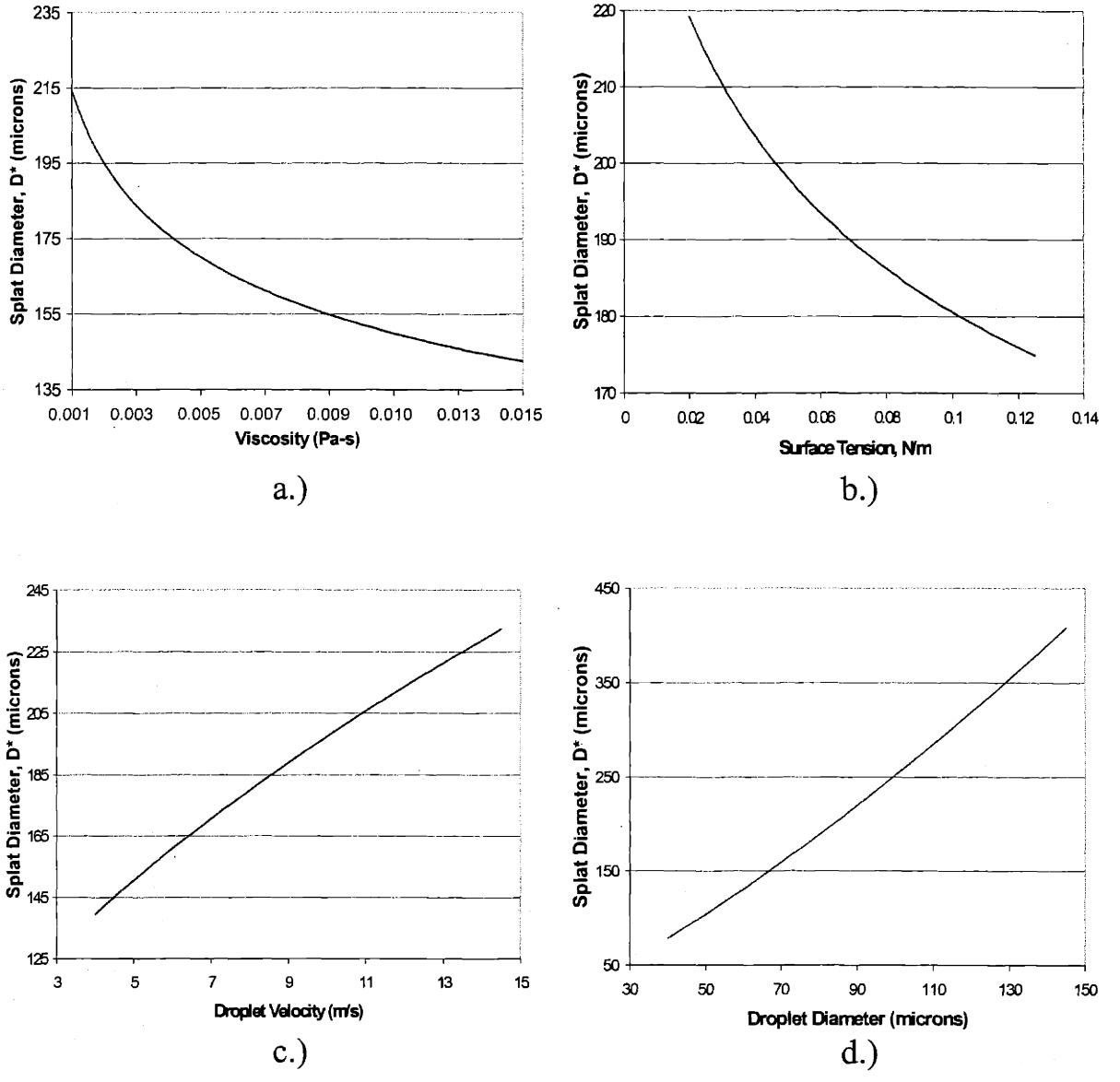

Figure 3.1: Variation of splat size with droplet parameters (from Eqn. 3.10). Only one parameter is being varied in each curve, with the others set at the standard values.

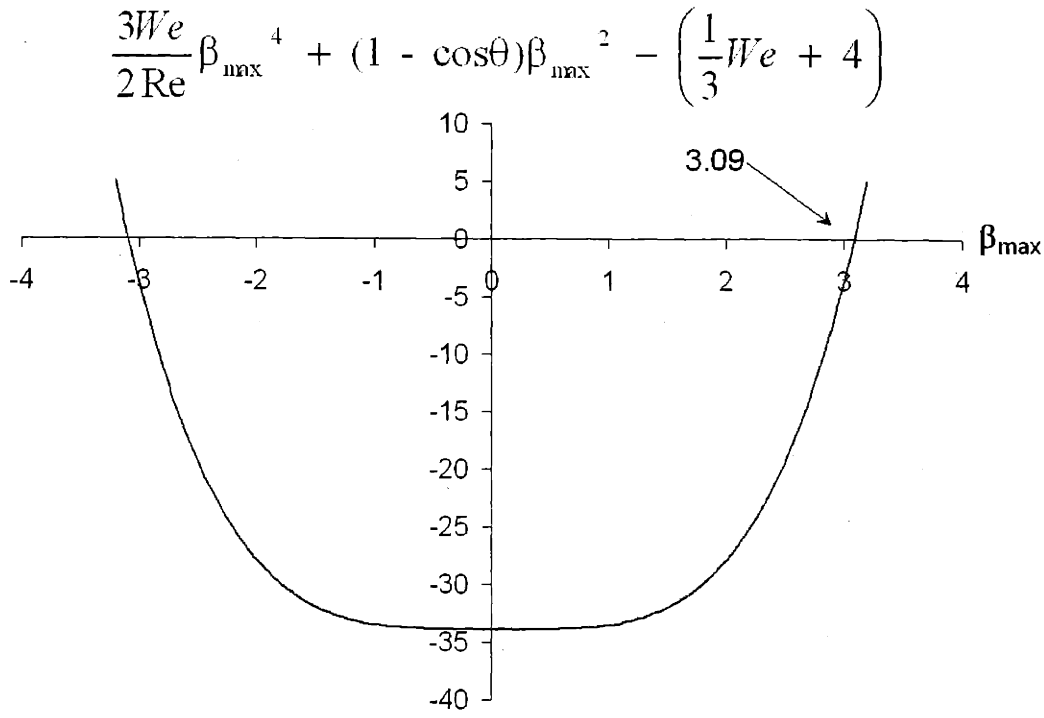

Figure 3.2: Plot of Eqn. 3.17 showing solutions.

The volume of the disc of liquid is

$$V \approx \frac{\pi D^{*2}}{4} h \qquad \text{Eqn. 3.15}$$

Thus

$$F_k \approx \frac{1}{4}\pi\eta\frac{U}{h} dD^{*2} \qquad \text{Eqn. 3.16}$$

They then equated the energies before and after impact, resulting in[46]

$$\frac{3We}{2Re}\beta_{max}^{4} + (1 - \cos\theta)\beta_{max}^{2} - \left(\frac{1}{3}We + 4\right) \approx 0 \qquad \text{Eqn. 3.17}$$

Eqn. 3.17 is plotted in Figure 3.2 for the conditions in Table 3.1. The intercepts are at +/- 3.09, so that $\beta_{max} = 3.09$. This yields a maximum droplet splat diameter of 247 μm, which is at least comparable to the results based on Eqn. 3.10 (the predicted widths actually overestimated their experimental data somewhat as well.) t_c for these conditions is ~10 μs, giving an approximate value for the time scale involved that is in agreement with the observations of Asai et al.[45] If droplet impact is in fact an important factor in the ultimate primitive size, it is important to characterize what role it plays under S-3DP™ conditions.

3.1.3 Modified Impact Model

The Model of Chandra and Avedisian is developed for a dense surface. The powder bed in S-3DP™ is of course porous, and as a result the relative amounts of liquid and solid surface are different than that assumed in Section 3.1.2. Thus the following modified form was developed from the basic energy balance for a droplet impacting a porous substrate.

The fraction of the solid surface actually comprised of solid is approximated as being equal to the fractional green density, X_g. Thus the surface energy before impact is the sum of the surface energy of a droplet of radius r_{drop} and the surface energy of the area of solid

surface that *will be covered* by the liquid after the droplet achieves its maximum extension, r_{max}:

$$E_{S1} = 4\pi r_{drop}^2 \gamma_{LV} + X_g \pi r_{max}^2 \gamma_{SV} \qquad \text{Eqn. 3.18}$$

The kinetic energy E_{K1} of a droplet of volume V_{drop} traveling at a velocity U prior to impact is given by the following equation:

$$E_{K1} = \frac{1}{2}\rho V_{drop} U^2 \qquad \text{Eqn. 3.19}$$

The kinetic energy of the liquid at the completion of impact is again assumed to be zero. The solid surface represented by the second term in Eqn. 3.18 has been replaced by solid-liquid interface. Two surfaces actually contribute to the total liquid-vapor surface, the top surface of the spherical liquid cap as well as the liquid along the liquid-substrate interface that occurs at the pores on the powder bed surface. Thus the total surface energy after impact is as follows:

$$E_{S2} = X_g \pi r_{max}^2 \gamma_{SL} + (1 - X_g)\pi r_{max}^2 \gamma_{LV} + 2\pi r_{max}^2 \frac{1 - \cos\theta}{\sin^2\theta}\gamma_{LV} \qquad \text{Eqn. 3.20}$$

The first term in Eqn. 3.20 is the contribution from the solid-liquid interface, the second term is from the liquid-vapor interface in the pore space, and the last term is from the surface of the spherical cap. The form of the viscous energy loss E_{VL} is taken to be that used in the development of Chandra and Avedisian, namely:

$$E_{VL} = 2\pi\eta \frac{U r_{max}^2 r_{drop}}{h} \qquad \text{Eqn. 3.21}$$

which is simply Eqn. 3.16 recast in terms of radii. h is then approximated by the cylindrical equivalent:

$$h = \frac{V_{drop}}{\pi r_{max}^2} \qquad \text{Eqn. 3.22}$$

Again equating the energy before and after impact, collecting terms and simplifying, the following equality results:

$$4 + \frac{We}{3} + X_g \beta_{max}^2 \cos\theta - (1 - X_g)\beta_{max}^2 - 2\beta_{max}^2 \frac{1}{1+\cos\theta} - \frac{3}{2}\frac{We}{Re}\beta_{max}^4 = 0 \qquad \text{Eqn. 3.23}$$

Solving for the roots of the equation results in $\beta_{max} = 2.92$, indicating a maximum splat diameter of 234 μm for an 80 μm droplet. This is of course smaller than the dense surface value of Chandra and Avedisian because the amount of high energy solid surface that is being covered by the liquid is decreased with a porous surface, with the difference in surface area made up by the presence of a liquid-vapor interface existing at the pore surfaces.

3.2 *Procedure for Characterizing Impact Effects*

Two different approaches to examining the effects of impact on primitive size were utilized simultaneously. High-speed (stroboscopic) photography was utilized to examine the printed binder solution on the powder bed *prior* to infiltration. The liquid bead width on the surface was measured from the resulting images under various conditions to determine their effects on impact. The primitives resulting from these experiments were then cured and retrieved, and their size was evaluated using the techniques outlined in Chapter 2.

3.2.1 Strobe Images of Impact Width

Standard slurry-jetted S-3DP™ powder beds were used in these studies, although their surfaces were buffed smooth to ensure a flat surface on which to print. This removes any effects of surface topography that could otherwise obscure the results. Standard binder solution formulations were typically employed, with some exceptions, as described below. Figure 3.3 is a schematic of the Droplet Impact Observation Station, or DIOS, which was used to capture the images of the printed binder solution. The DIOS was developed in the lab

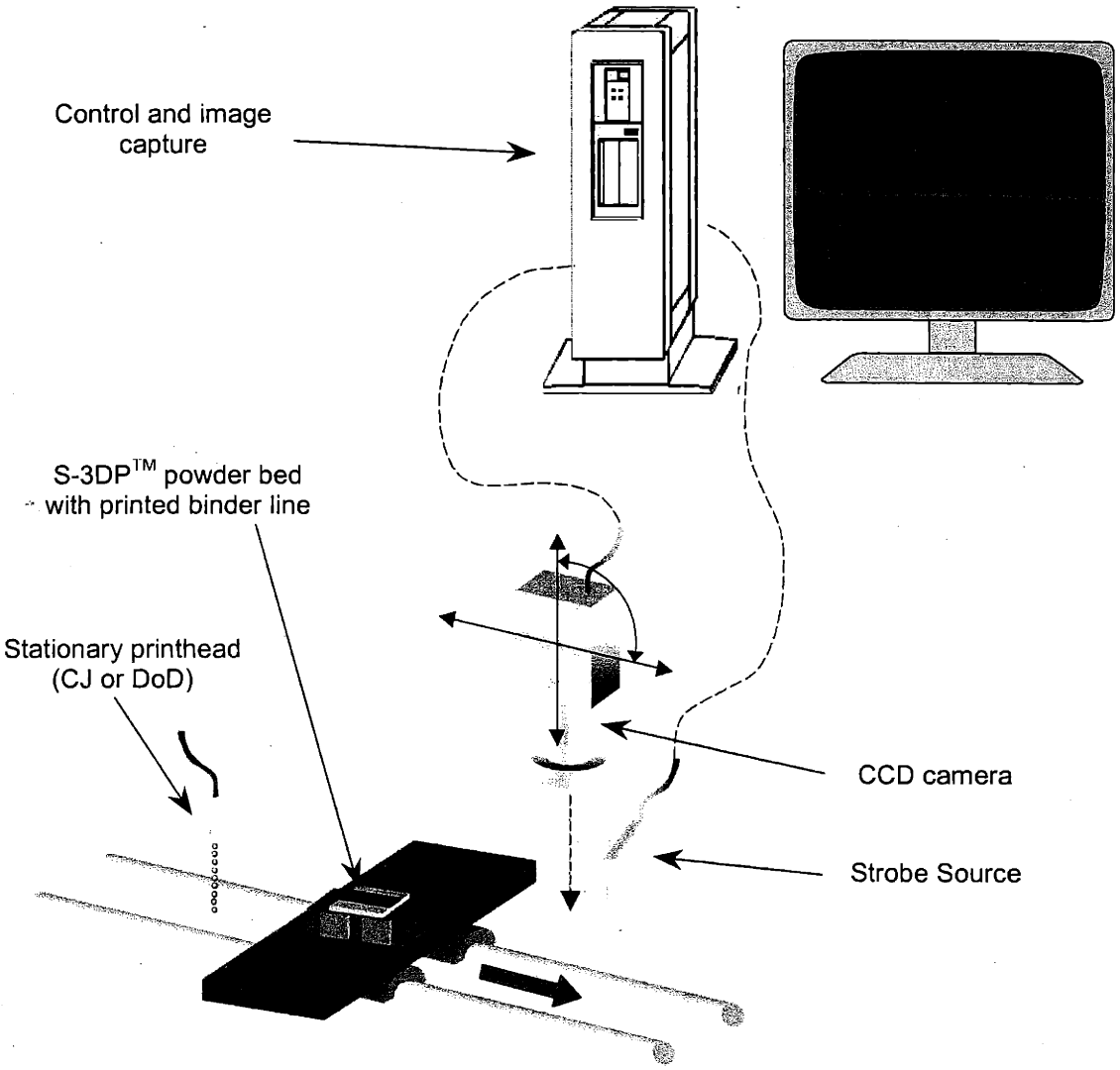

Figure 3.3: Schematic of the Droplet Impact Observation Station (DIOS).

of Professor Emanuel Sachs (Mechanical Engineering, MIT.) The station is composed of the following components: a motorized carriage system to move the powder bed; a printhead assembly (CJ or DoD); a CCD camera for image capture; a strobe lighting system; a PC system and control hardware for controlling the motion of the stage, the firing of the strobes, and the capture of images. The carriage system is a motorized stage that moves on an air bearing. The motor is controlled by the computer via a motion control interface, and position is given by a linear encoder along the length of travel. The interface to the computer is written in Labview™. Powder beds (or other substrates if desired) are mounted on a small 1-axis stage on the carriage and are passed under the binder nozzle to deposit the liquid on the substrate's surface. The carriage velocity is variable (a user-defined parameter.) The strobe then fires when the carriage reaches a pre-determined position along the axis of travel (another user-defined parameter.) The image is then captured by the computer system and written to disk, as well as being displayed on screen. The strobe system actually has two strobes, one green and one blue, and the delay (in microseconds) between the firing of each strobe can be independently varied. This allows extraction of the individual color layers from the captured RGB image in software, facilitating the production of a time series of grayscale images with microsecond-scale time steps.

The time lapse between droplet impact and image capture was determined by the distance between the axis of the camera and the printhead. This distance was measured by printing onto a ruler on the carriage (with 0.5 mm tick marks) while simultaneously imaging it in real time. Imaging of the bead of liquid was done at 3 ms after impact (5 mm at 150 m/s) for these impact experiments. This is well after impact should be complete, but shorter than the expected time scale of infiltration in the S-3DP™ Al_2O_3 powder beds (Ceralox HPA 1.0.) The camera must be mounted at an angle for very short times (or to image the actual impact) due to obstruction by the printhead assembly.

Printing solutions were the standard PAA 60000 in DI water with 10 wt.% glycerol (based on PAA solids.) Fluorescein disodium salt (Sigma), a fluorescing material, was added to the binder solutions to aid in imaging of the printed binder solution. Fluorescein is excited in the UV, and emits at 513 nm. The concentration was kept quite low (100 ppm based on the

total solution mass.) The blue strobe of the DIOS produces sufficient amounts of UV to cause appreciable light emission in the fluorescein.

Image analysis was carried out using PhotoShop™ 5.5 (Adobe) and ImageTool. An average width of the liquid on the surface was given by measuring the total area (top-down view) and dividing by the length of the field of view. This minimized the effects of any ripples or other irregularities along the liquid edge. Five images were typically captured per experimental condition, and the results were averaged. Actual primitive size was measured by removal and cross-sectioning, as has been described in Chapter 2.

3.3 *Effects of Viscosity on Impact*

The effect of viscosity on impact is strong in both models presented above. In addition, viscosity variations can be brought about independent of the other operating parameters (which is not necessarily true of droplet size or velocity, both of which involve changing other parameters to keep the binder dose constant.) Thus viscosity modification was explored as the most effective means of altering impact behavior independent of other printing parameters.

3.3.1 Viscosity Modification Via Chemistry

A number of possible thickening additives that were examined are listed in Table 3.2. The table indicates the concentration of thickening agent used, whether heat was required to dissolve the additive, whether or not complete dissolution was achieved, whether any reaction appeared to occur, and the effect on viscosity. Reaction between the components produced thick white precipitates in all but the highest thickener contents, which gelled completely and therefore were unsuitable. The PAA solutions have a starting pH of ~2.5, and so it was proposed that adjusting the pH (increasing it) might be beneficial by making the solution less reactive. This was attempted with several of the HPMC solutions, however adjustments with 1M KOH over a wide range of pH values were unsuccessful. The order of addition of the components also seemed to have little or no effect. Heating to ~85°C allowed complete dissolution of the additive in most cases, however precipitates still appeared upon cooling to

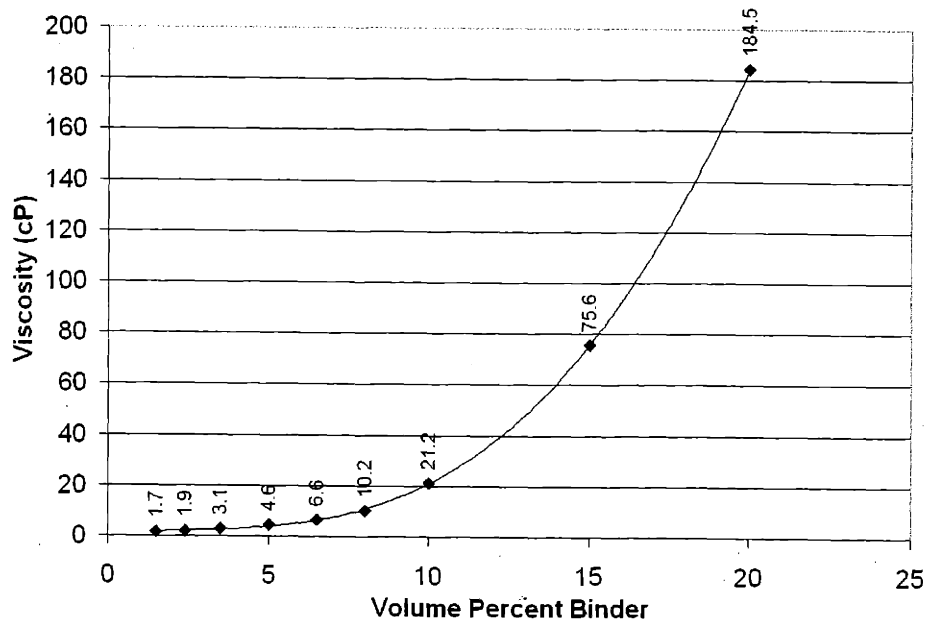

Figure 3.4: Dependence of aqueous binder solution viscosity on PAA 60000 content (solution contains 10 wt.% glycerol on solid PAA basis).

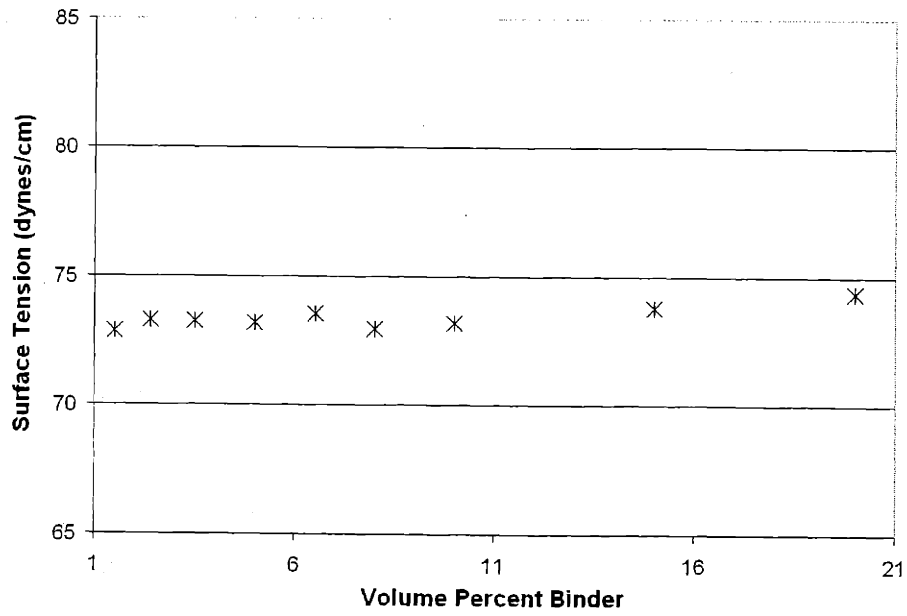

Figure 3.5: Dependence of binder solution surface tension on PAA content.

Thickening Agent	Wt. %	Heating Required?	Complete Dissolution ?	Reaction/ Precipitate ?	Titrated with KOH?	Qualitative Effect on Viscosity
PVP	1	no	-	yes	no	-
HEC	1	yes	yes	no	no	thick gel
HEC	0.25	yes	yes	yes	no	increase
HEC	0.15	yes	yes	yes	no	increase
HEC	0.1	yes	yes	yes	no	increase
HPMC	1	no	yes	no	yes	large increase
HPMC	0.5	yes	no	no	no	-
HPMC	0.5	no	yes	yes	yes	-
HPMC	0.3	no	yes	yes	yes	-
PEG 20M	1	no	yes	yes	no	-
PEG 20M	1	no	yes	yes	no	-
PEG 8000	1	no	yes	yes	no	-

Table 3.2: Thickening agents examined for the PAA binder system. (PVP = polyvinylpyrrolidone, HEC = hydroxyethyl cellulose, HPMC = hydroxypropyl methyl cellulose, PEG = polyethylene glycol.

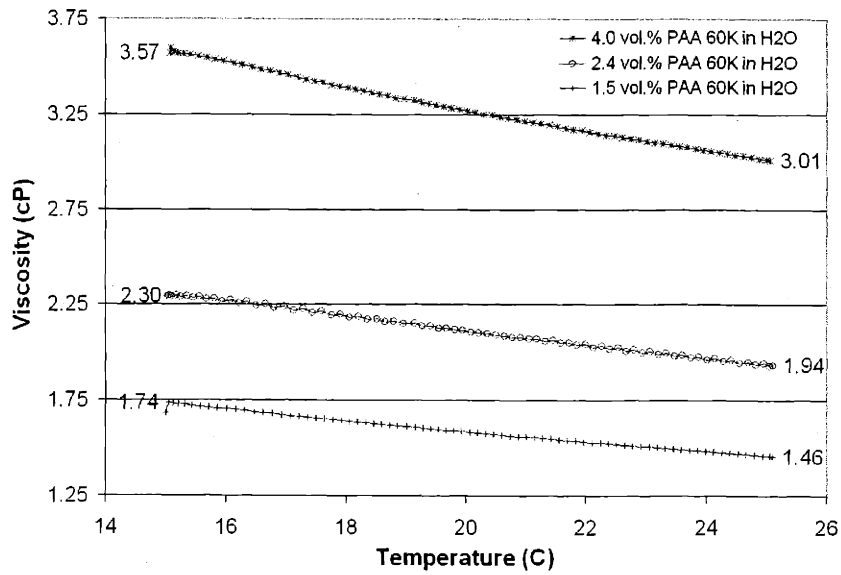

Figure 3.6: Temperature dependence of viscosity in PAA-water solutions.

room temperature. As a result, none of the thickeners examined were deemed suitable as an additive to the PAA system.

Another possibility lies in the dependence of the binder solution viscosity on the polymer content. Solution viscosities were measured using a Paar Physica viscometer in the parallel plate configuration (strain rate control). Figure 3.4 contains viscosity data for water-PAA solutions (with 10 wt.% glycerol on PAA basis) at various PAA contents. The dependence is quite strong, with the viscosity increasing by a factor of 2 in going from 1.5 to 4.0 vol.% PAA. In addition, the surface tension of the solution is unaffected by PAA content in this range, as shown by Figure 3.5. This method does however have the drawback of changing two variables at once (solution viscosity and polymer content in the primitive.)

3.3.2 Viscosity Modification Via Temperature

The viscosity of polymer solutions can have a strong temperature dependence.[51] The viscosity dependence of PAA solutions was measured using a cone and plate viscometer (Paar Physica USA, Inc.), the results of which are shown in Figure 3.6 for 1.5, 2.4, and 4.0 vol.% PAA solutions in DI H_2O. Decreasing the temperature by only 10°C increases the viscosity by nearly 20% in the standard 2.4 vol.% PAA solution. Solution temperature was therefore studied as a means of altering the binder solution viscosity.

The temperature of the binder solution was controlled by submersing a 60 cm length of the binder supply line (and the binder line filter, where residence time is highest) in a temperature-controlled bath. The line leading from the bath was insulated with Styrofoam to minimize heat loss on the way to the nozzle, and the length of line between the bath and the nozzle was kept at a minimum. The binder temperature at the nozzle (i.e. upon exit) was measured prior to printing by inserting a very fine T-type thermocouple into the stream just below the nozzle. The temperature of the binder at the powder bed level was similarly measured. The temperature at the filter outlet (i.e. upon exiting the bath) was also recorded by momentarily stopping the jet and uncoupling the line from the filter.

In order for this method of viscosity control to be fully effective, the printed binder solution must a.) not cool to room temperature during flight, and b.) not cool to the substrate temperature within the time scale of impact. Thus, the heat loss during flight and to the

Property	Water	Air
η (N-s/m^2)	-	182 x 10^{-7} (295K), 187 x 10^{-7} (305K)
k (W/m-K)	0.62 (305K)	0.026 (296K)
C_p (J/g-K)	4.18 (305K)	-
ν (m^2/s)	-	15.36 x 10^{-6} (295K)

Table 3.3: Data used in calculating the convective cooling of a binder droplet in flight.[52]

Measurement Location	Temperature (C)		
Water bath	43	19	1
Filter outlet (exit from bath)	38	-	-
Nozzle	31	21	14
Powder bed level	29	21	14

Table 3.4: Water bath temperature and the resulting binder solution temperatures at various locations along the flow path to the powder bed.

substrate after impact are modeled in the next two sections. The temperature drop of the droplet during flight has also been experimentally determined.

3.3.2.1 Heat Loss During Flight

An analytical solution exists for forced-convective cooling of a sphere. The following development for the cooling of a spherical droplet during flight is taken from reference 52. The droplet is assumed to be water (this should introduce little error at the low binder contents under examination, ~1 - 4 vol.%), and the property data for water and air are also taken from reference 52 and are shown in Table 3.3. The flight time can be taken as the jet velocity at the nozzle (~10 m/s) divided by the distance to the powder bed (~2 cm), or 2 ms (this neglects drag-induced deceleration, however it has been shown that this effect is small and can be neglected with little effect on accuracy[33].) The droplet diameter was assumed to be 80 μm (typical of CJ droplets from a 40 μm nozzle), and the initial droplet temperature was taken to be 30°C with an ambient temperature of 20°C. The Nusselt number (Nu_D) is given by the following equation:

$$Nu_D = 2 + \left(0.4\,Re_D^{1/2} + 0.06\,Re_D^{2/3}\right)Pr^{0.4}\left(\eta_\infty/\eta_S\right)^{1/4} \qquad \text{Eqn 3.24}$$

where:

$$Re_D = \frac{Ud}{\nu} \qquad \text{Eqn. 3.25}$$

Pr = 0.71 (the Prandtl number)

η_∞ = air viscosity at ambient temperature

η_S = air viscosity at droplet surface temperature

ν = kinematic viscosity of air

From the data above and in Table 3.3, $Re_D = 52$, resulting in $Nu_D = 5.2$. The convective heat transfer coefficient, h, at ambient is given by Eqn. 3.26:

$$h = Nu_D \frac{k}{d} \qquad \text{Eqn. 3.26}$$

where k is the thermal conductivity of air at ambient. h from Eqn. 3.26 is 1684 W/m^2-K. The time t to cool the droplet from a given initial temperature T_i to temperature T with the ambient air at temperature T_∞ is given by Eqn. 3.27:

$$t = \frac{\rho V c_p}{h A_S} \ln\left(\frac{T_i - T_\infty}{T - T_\infty}\right) \qquad \text{Eqn. 3.27}$$

where:

ρ = liquid density

c_p = liquid specific heat capacity (at constant pressure)

V = droplet volume

A_S = droplet surface area

Inserting the flight time (2 ms) for t and solving for T, a temperature drop of only 0.6 degrees is estimated by convection.

B. Wu has shown that the evaporative cooling in flight of a 3DP™ binder droplet with chloroform as the solvent was "significantly less than 1°C."[33] Based on the comparable heat of vaporization (44 kJ/mol for water[53] compared to 29 kJ/mol for chloroform[33]), and the much higher vapor pressure of chloroform, the temperature drop due to evaporation in aqueous PAA solutions is expected to be inconsequential. This coupled with the minimal predicted temperature drop from convection during flight indicates that large variations in droplet temperature at impact can be readily achieved by changing the initial temperature of the solution.

Experimental measurements of the droplet temperature at the nozzle and at bed level (before impact) are contained in Table 3.4 for several bath temperatures. Considerable heat transfer can occur en route to the nozzle, resulting in the nozzle temperature being different from the bath temperature. The temperature change between the nozzle and bed level however is quite small, as predicted by the above development. The droplet temperature at contact with the powder bed can thus be effectively controlled via the temperature bath.

3.3.2.2 Heat Loss to Substrate After Impact

It is important that droplet cooling by heat transfer to the substrate does not occur on the time scale of impact if temperature is to be used to vary the liquid's viscosity. The cooling of the printed binder solution in contact with the substrate is a dynamic heat transfer problem on a finite scale, so steady state conditions most certainly do not apply. A forward finite difference method was therefore employed to model the cooling of the solution. A 2D approximation of the system (perpendicular to the axis of travel) was utilized, as seen in Figure 3.7. The liquid was taken as a rectangle 100 cells wide by 10 cells high, initially at a uniform temperature of 30°C. The cell dimension was chosen to be 3 x 3 μm, giving a liquid cross section of 300 x 30 μm. The Al_2O_3 substrate was 480 cells wide by 200 cells high (with the same cell size as the binder), initially at a uniform temperature of 20°C, the same as the ambient. The substrate is much larger than the liquid to keep edge effects from influencing the results. This is necessary because Al_2O_3 has both a higher thermal conductivity and lower heat capacity than water, and so the substrate must be much larger than the liquid to accommodate the heat flow.

The change in temperature of a node within the interior of either the liquid or the solid is given by a discrete form of the two-dimensional heat equation:[52]

$$\frac{1}{\alpha}\frac{\partial T}{\partial t} = \frac{\partial^2 T}{\partial x^2} + \frac{\partial^2 T}{\partial y^2} \qquad \text{Eqn. 3.28}$$

where:

$$\alpha = \frac{k}{\rho c_p} \text{ , the thermal diffusivity of the material} \qquad \text{Eqn. 3.29}$$

The ambient (air) temperature was held constant at 20°C. The boundary condition of the liquid-air and Al_2O_3-air interfaces is given by convection[52]:

$$-k\left.\frac{\partial T}{\partial x}\right|_{x=0} = h[T_\infty - T(0,t)] \qquad \text{Eqn. 3.30}$$

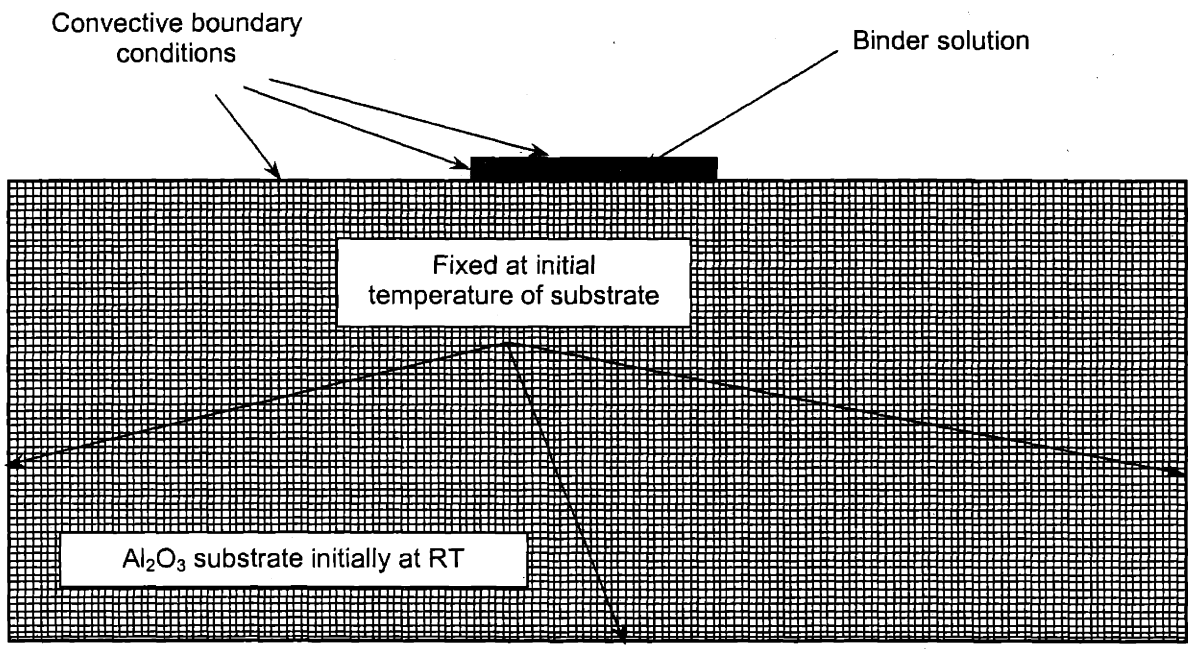

Figure 3.7: Schematic of the geometry and boundary conditions used in the 2D finite difference model of droplet cooling after impact (only every third gridline of the mesh shown.)

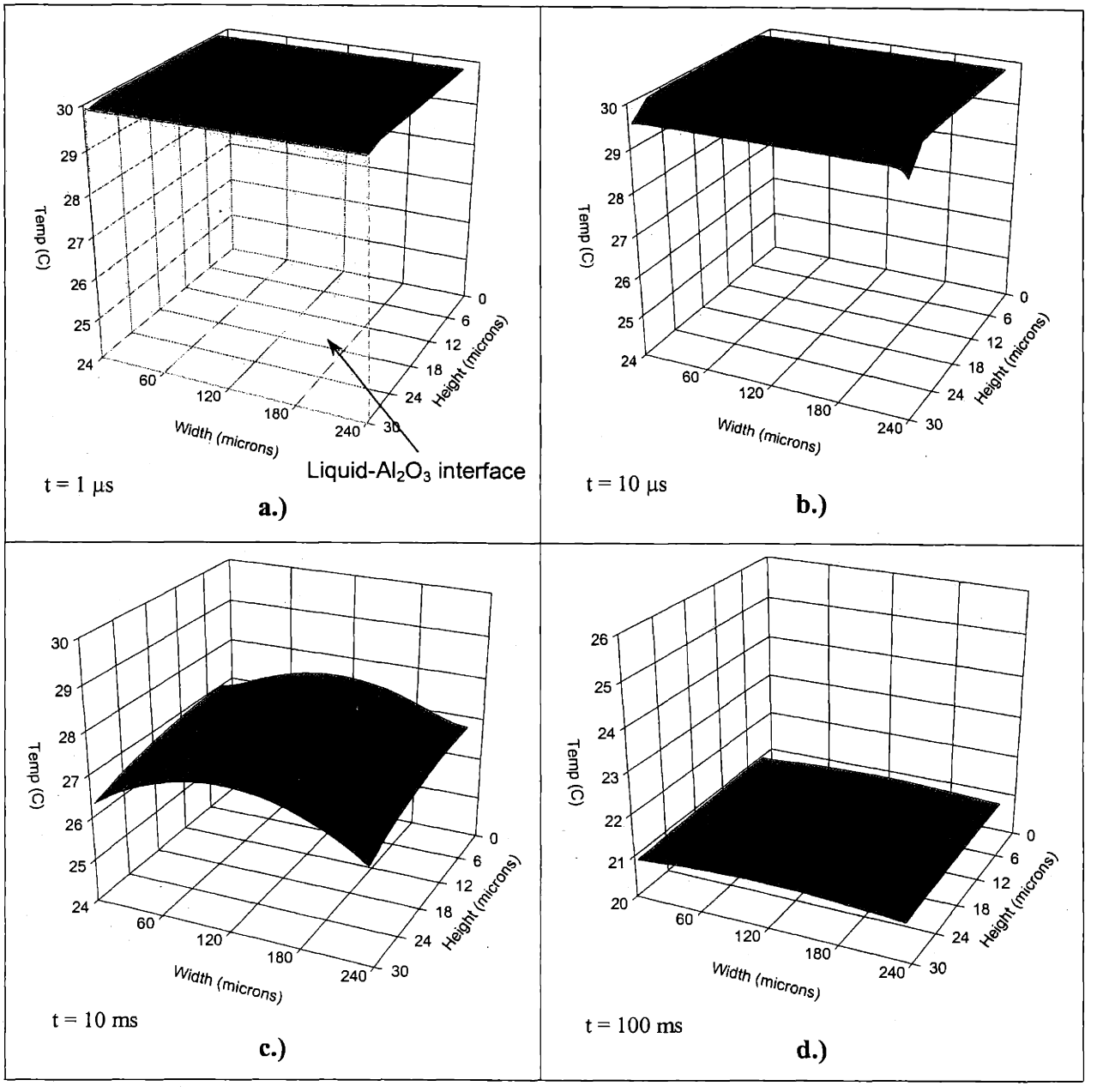

Figure 3.8: Temperature profile across the liquid from the 2D forward finite difference model described in the text a.) 1 μs b.) 10 μs c.) 10 ms and d.) 100 ms after impact (note x and y scales are not equal.)

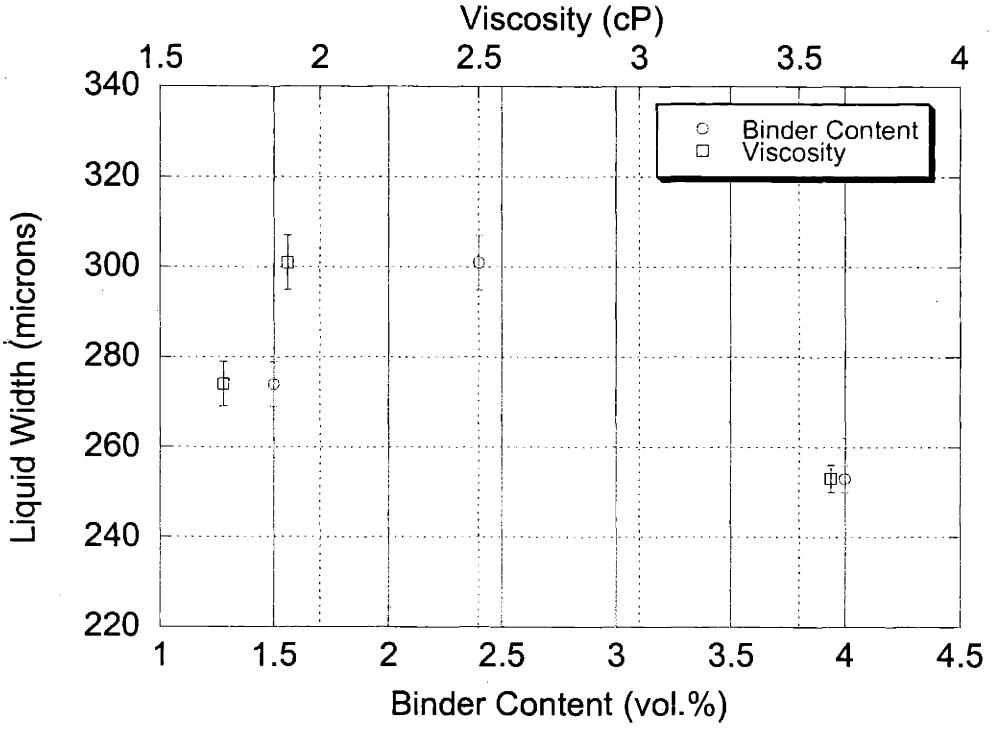

Figure 3.9: Printed PAA-solution bead width on a buffed Al_2O_3 S-3DP™ powder Bed (Ceralox HPA 1.0) 3 ms after impact for various polymer contents; width is also plotted as a function of the resultant viscosity on the second x-axis.

The temperature of the other three boundaries of the substrate is fixed at the initial temperature (i.e. 20°C.) The above forward finite difference model was coded using C^{++}. The time step was chosen as 0.1 μs, which, combined with the 3 μm mesh size, satisfies all stability criteria. The actual code is provided in Appendix 1. Figure 3.8 contains the results of simulations using this method at various total times (times after impact). The shaded region in 3.8a indicates x = 30, i.e. the interface between the liquid and Al_2O_3 substrate (x = 0 is the top surface of the liquid.) The results lead to two interesting observations. Cooling on the time scale of impact, ≤ ~10 μs, is small (<0.5°C) and confined to the surface region. Thus, cooling of the liquid during impact is negligible, so the liquid can be assumed to be at the initial liquid temperature. However, at times on the order of infiltration (~10's of ms), the liquid temperature may be changing considerably, and so the liquid cannot be assumed to be at the initial temperature, but is actually at some (non-uniform) temperature between that of the substrate and liquid initial temperatures. Control of the binder temperature appears to be a valid method of varying the solution viscosity on the time scale of impact from these observations.

3.3.3 Results of Viscosity Control Experiments

1.5, 2.4, and 4.0 vol.% PAA solutions were utilized to examine the effects of solution viscosity on printed line width. These solutions have viscosities of 1.7, 1.9, and 3.6 cP, respectively. The Asai impact model predicts a difference of 20 μm between the splat widths of solutions having viscosities of 1.7 and 3.6 cP. The average binder solution bead width on the surface of an Al_2O_3 S-3DP™ powder bed (Ceralox HPA 1.0, buffed smooth) 3 ms after impact is shown in Figure 3.9 for each of these polymer concentrations. The behavior that would be expected were impact the controlling factor in primitive width (i.e. narrower lines with higher viscosity) is not realized. In fact, no real trend appears to exist. It should be noted that the 1.5 and 4.0 vol.% PAA experiments were carried out on the same day, while the 2.4 vol.% PAA experiments were on a different day. This large day-to-day variation in the extension of the liquid has been observed numerous times by the author. It makes comparing results difficult and may indicate that some other factor is controlling the liquid line width.

The temperature dependence of the viscosity was utilized next to preclude any possible secondary effects of the PAA content on line width. The dependence of the splat width on temperature calculated from the Asai model is shown in Figure 3.10. The splat width is predicted to vary by ~10 μm over the temperature range examined in this study (13 to 31 °C.) Figure 3.11 is a graph showing the average printed binder solution bead width on the surface of Al_2O_3 S-3DP™ powder beds (Ceralox HPA 1.0, buffed smooth) 3 ms after impact. The x-axis of this graph is the date that the observations were made, and the liquid temperature is noted for each data point (temperature measured at the level of the powder bed.) The viscosity of the binder solution at 13, 20, and 31 °C is 2.4, 2.1, and 1.7 cP, respectively. Large variations in liquid width were observed, but the liquid width does not appear to have any clear correlation with the solution temperature (and thus viscosity) based upon this data. Two observations are particularly interesting: the measured liquid width at 20°C was very different on 10/24/00 and 11/06/00 (275 μm versus 235 μm); and the liquid width on a given day (11/06/00) was nearly identical at two different solution temperatures (235 μm at 20°C versus 236 μm at 13°C.) In addition, the day-to-day variations observed are considerably larger than the effects of impact could be expected to account for.

A concern that arose was whether the large day-to-day differences in liquid width were the result of errors or uncertainty in the timing or setup of the strobe experiments. If so, the resulting green Al_2O_3 primitive width after removal should show no correlation to the above liquid width results. Examination of the actual primitive size upon removal from the powder beds used in these experiments does not bear this out, however. Figure 3.12 shows the average primitive width resulting from the binder lines represented in Figure 3.11. The same general trend is seen in both figures, indicating not only that the observed trends in liquid width are not an artifact of the measurement technique, but also that the liquid width observed at 3 ms after impact does in fact correlate directly with the resulting primitive width, and that these widths appear to vary greatly from one day to the next.

Final evidence that impact is not the primary process determining line width in CJ printing was obtained by printing onto two dense polished surfaces, one Al_2O_3 and one SiO_2. The impact (splat) width on these two surfaces should be identical. The width of the printed liquid 3 ms after impact, however, was 186 μm on the polished Al_2O_3 compared to 274 μm on

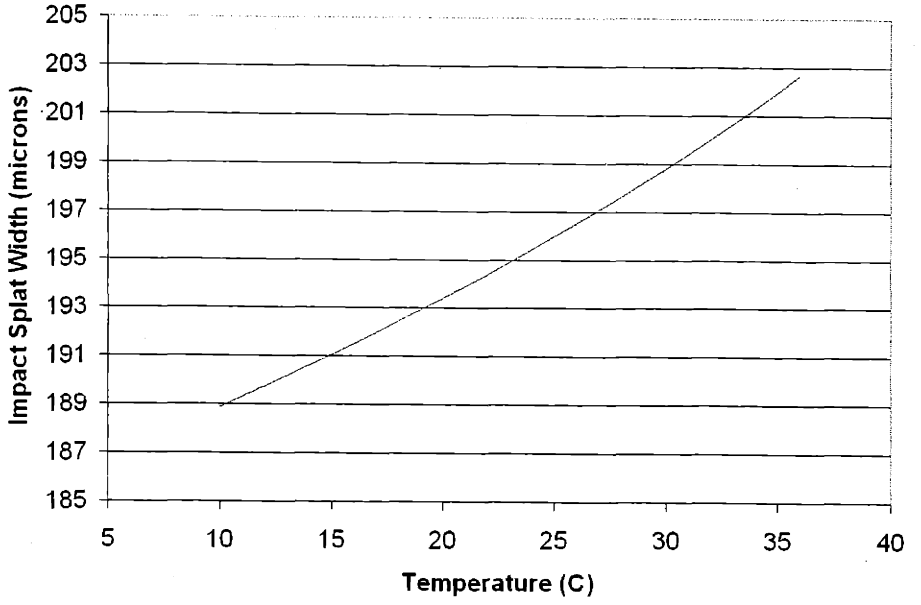

Figure 3.10: Expected dependence of splat width on temperature from the Asai model for a 2.4 vol.% PAA binder solution.

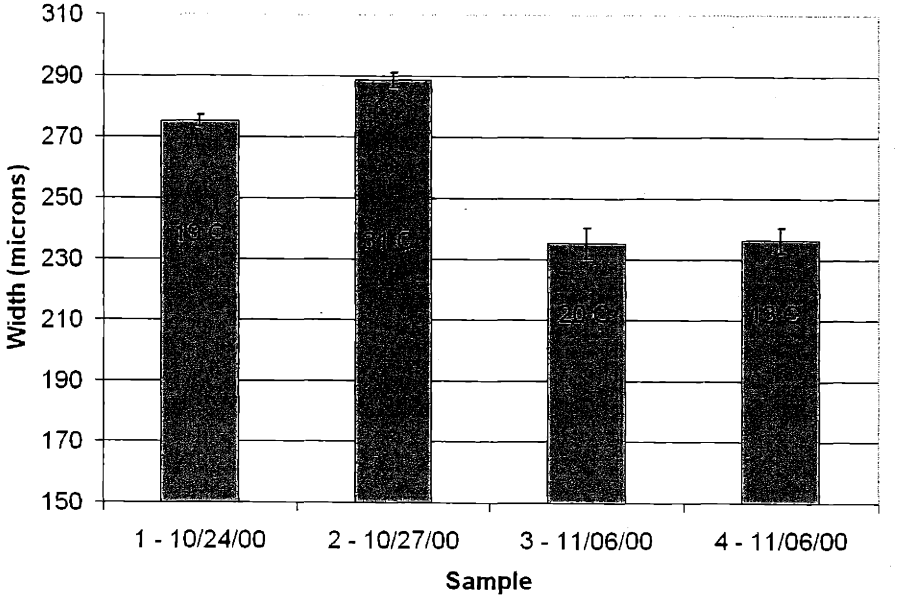

Figure 3.11: The width of the printed bead of liquid on a buffed Al_2O_3 S-3DP^{TM} powder bed 3 ms after impact, labeled with the liquid temperature.

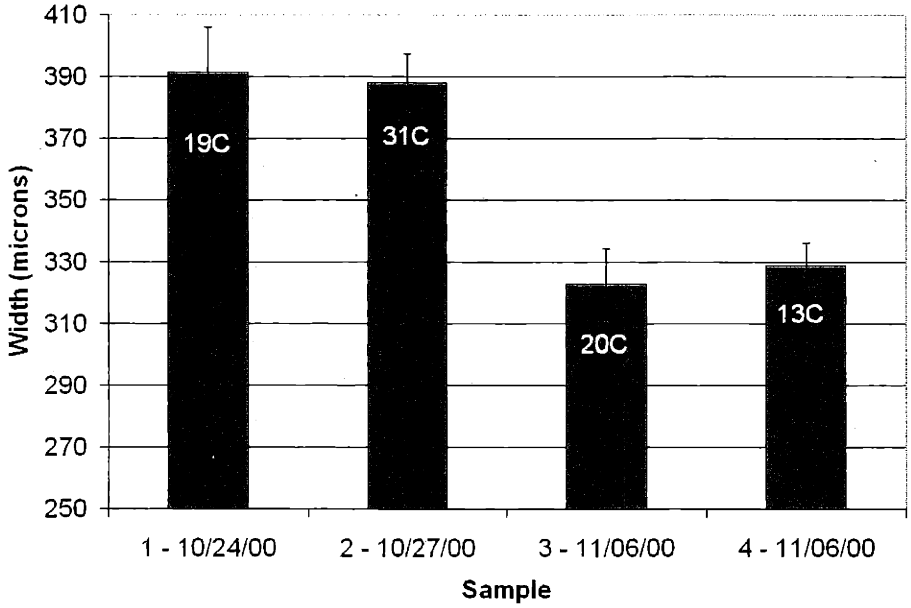

Figure 3.12: Average widths of the retrieved primitives corresponding to the liquid widths shown in Figure 3.11.

the polished SiO_2. Both sets of experiments were run on the same day. The key difference between these two samples is the surface chemistry, and thus the wetting properties. Impact processes, which occur on the timescale of micro-seconds, are strongly dependent upon viscosity and in turn depend on temperature. These parameters were varied, but their effects were found to be insignificant relative to the observed day-to-day variations. The next goal is to determine what processes and parameters could vary sufficiently from day to day to account for the large variations in liquid bead width. One hypothesis is that the wetting properties of the green powder bed may vary both with the age of the bed and with the local humidity, which is not controlled. This is strengthened by the above observations on dense polished Al_2O_3 and SiO_2, where the key difference is their wetting properties. The next chapter explores the role of wetting and spreading of the liquid binder on the bed surface in determining primitive width.

Chapter 4: Wetting and Spreading Phenomena

The results of Chapter 3 led to the hypothesis that spreading of the printed binder solution on the surface of the powder bed prior to and/or during infiltration may determine the primitive width. The wetting properties of the powder beds (both on the surface and within the pore structure) could be changing from day to day due to aging or redistribution of the polyethylene glycol (the redispersion aid), local humidity variations, etc., leading to the unexplained variations in liquid extension found in Chapter 3. This chapter thus explores the role played by wetting and spreading of the binder solution.

4.1 Liquid Spreading

The amount of polymer solution deposited is a known quantity, and it is a simple geometric exercise to calculate the maximum liquid extension (i.e. width) that is expected from the equilibrium contact angle of the liquid on the solid. The calculation for a single droplet has been outlined by Arthur[49], and the maximum extended diameter at equilibrium is given by Eqn. 4.1:

$$D^*_{w,d} = 2 \cdot \left(\frac{3 \cdot V \cdot \sin^3 \theta}{\pi (1 - \cos\theta)^2 \cdot (2 + \cos\theta)} \right)^{1/3} \qquad \text{Eqn. 4.1}$$

where $D_{w,d}^*$ is the maximum extension of the droplet due to wetting, θ is the equilibrium contact angle, and V is the droplet volume. This can then be extended to a printed line by employing the binder dose A_B and modifying the above equation, resulting in Eqn. 4.2:[44,49]

$$D^*_{w,l} = 2 \cdot \left(\frac{A_B}{(\theta - \sin\theta \cdot \cos\theta)/\sin^2\theta} \right)^{1/2} \qquad \text{Eqn. 4.2}$$

$D_{w,l}^*$ has a very strong dependence on the contact angle. Figure 4.1 shows just how sensitive the maximum extension is to variations in θ for the standard printing conditions found in CJ

printing in S-3DP™. It can be seen from these calculations that at low contact angles with a sufficiently slow infiltration time to allow spreading, spreading of the liquid could easily outweigh the effects of impact. It is also clear that small variations in the contact angle with age of the bed or moisture content could result in substantial differences in primitive size if spreading is the dominant factor.

4.1.1 Contact Angle

The contact angle used in the above equations to find equilibrium liquid width on a rough surface is *not* necessarily the same as the angle measured on a smooth polished surface. The effective or apparent contact angle on a rough surface is in general depressed for low ideal contact angles (on a smooth surface), while the opposite is true for high contact angles.[54,55,56] The extent of the variation is also dependent on the type and magnitude of the roughness. The effective contact angle on the powder bed must therefore be estimated, e.g. by the value measured on a rough dense surface.

4.1.2 Infiltration Time

Another factor that must be considered is the effect of the infiltration of the liquid on spreading. The infiltration time of a printed binder line has been observed to be quite long, on the order of 10's of milliseconds. If the infiltration and spreading times of the printed binder solution are comparable, the net result could be the occurrence of partial (but not complete) spreading, i.e. infiltration of the binder solution would sap the supply of liquid before complete spreading had taken place. Thus the extent of liquid extension (and therefore the primitive width) would be very sensitive to changes in the infiltration time (slower infiltration leading to wider binder line width.) The relative importance of this effect can be determined by varying the infiltration time and observing the effect on the extent of liquid spreading.

Extensive work has been done on the capillary infiltration (and thus infiltration rates) of liquids.[57,58] The flow into a porous bed can be modeled by Darcy's law[59]:

$$q = \frac{k}{\eta}\frac{\Delta P}{h} \qquad \text{Eqn. 4.3}$$

where:

q = the volumetric flow of liquid per unit area

k = specific permeability of the powder bed

ΔP = the driving pressure for infiltration

η = the liquid viscosity

The driving pressure for infiltration in the S-3DP™ powder bed is capillary pressure, which is proportional to the inverse of the pore radius, 1/r. The specific permeability, k, is proportional to the square of the pore radius, r^2.[59] The net result is that the infiltration rate is approximately proportional to the pore size, or conversely, the infiltration time t is inversely proportional to the pore size:

$$t \propto \frac{1}{r} \qquad \text{Eqn. 4.4}$$

Quantitative analysis of infiltration rate in real porous bodies using Eqn. 4.3 requires the adoption of an effective pore size.[59,60] The proportionality in Eqn. 4.4 should however hold true regardless of the actual magnitudes of the infiltration times.

The above discussion suggests a relatively simple means of controlling infiltration rate. The pore size in a green S-3DP™ powder bed is directly related to the particle size of the stock powder. By employing chemically identical powders with varying particle size, the infiltration time of the printed binder solution can be independently controlled. Subsequent observations of the liquid behavior on the surface of powder beds of different mean particle size at various times after impact using the strobe imaging station would then allow the determination of the effect of infiltration time on total spreading width of the printed binder solution.

The existence of competitive spreading and infiltration would provide a means for controlling the primitive aspect ratio by tailoring the infiltration rate. The infiltration and spreading times have therefore been characterized, and the effect of infiltration time on liquid spreading has been evaluated.

4.2 *Procedure*

It was first necessary to characterize the contact angle of the binder solution on the substrates used. The spreading of the liquid on the surface of the powder bed was then characterized by producing a time series of images of the liquid line width (i.e. the time between liquid impact and the image was varied.) The infiltration time of the binder solution was then varied by changing the average pore size of the powder bed.

4.2.1 Contact Angle Measurements

Contact angles were measured on both smooth (polished) and rough (as-fired) dense substrates. Al_2O_3 substrates were slip cast from Ceralox HPA 1.0 slurries. The dried discs were planed and buffed smooth, and were sintered for 2 hours at 1600°C. The dense disc was then polished *on one side only* to a 1 μm diamond finish. The other side was left in the as-fired state (referred to henceforth as the "rough" side) to better approximate the surface of a green S-3DP™ powder bed. The samples were washed and heated to 600°C for 4 hours to remove any organics that might be carried over from the polishing process (the rough surfaces were given the same treatment.) They were then washed in DI H_2O and allowed to sit under ambient conditions for at least 3 days to allow the surface to come to equilibrium.

The contact angle measurement was performed optically using a digital SLR with a macro lens attached (Kodak DCS-460 with Nikon 105mm f/2.8 micro lens), and strobe back-lighting was employed (Nikon SB-28 Speedlight) to maximize contrast. 3 μL droplets of 2.4 vol.% PAA binder solution were dropped onto the surface of the substrate using a micro-pipette (the drop was brought into contact with the substrate, which pulled it from the tip of the pipette via capillarity.) There was a delay of approximately 0.5 s between contact of the drop with the surface of the substrate and the actual image (the camera was fired using a cable release.) The contact angle was measured on each side of the droplet using ImageTool and the two numbers were averaged. The results from two (for rough surfaces) or five (for polished surfaces) different droplets were then averaged (due to the lower effective contact angle on the rough surface, only two droplets could fit on the 1" discs used after spreading.)

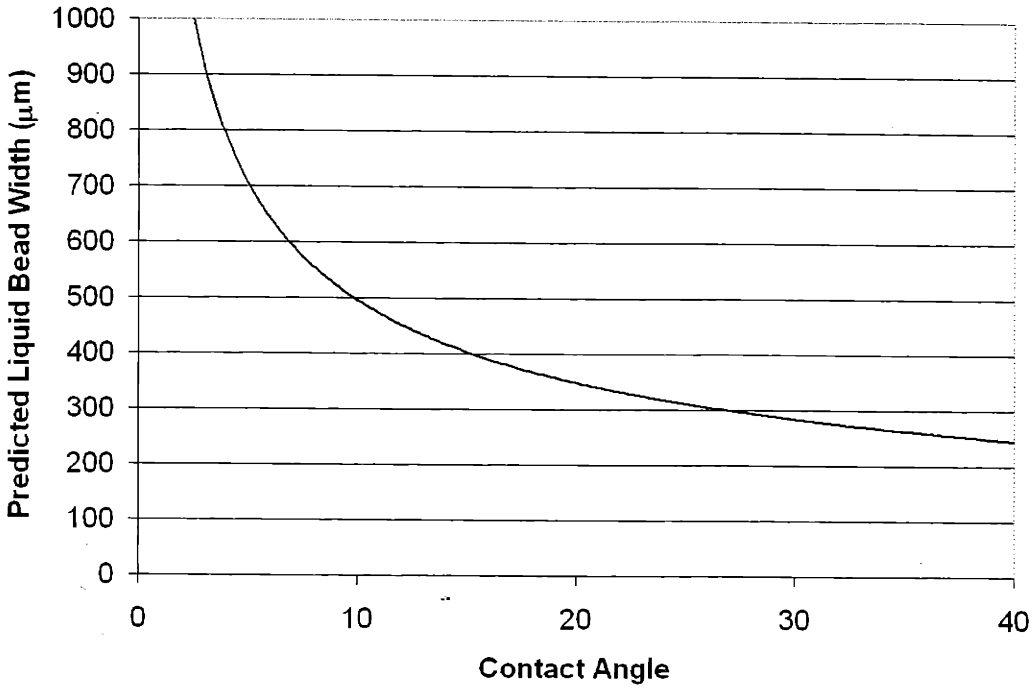

Figure 4.1: Wet line width predicted at equilibrium from Eqn. 4.2 for various contact angles at a binder dose (A_B) of 7268 μm^2.

Stock Powder	Mean Particle Diameter (μm)
HPA 0.5	0.3
HPA 1.0	0.6
SPA-TMXX 3	1.6

Table 4.1: Particle size of Ceralox high purity Al_2O_3 powders used in S-3DP™ slurries after 20 hours of ball milling.

4.2.2 *Time Series of Spreading*

The width of the binder line at various times after impact was measured using the DIOS equipment described in Chapter 3. The delay between impact and image capture was varied by changing the distance between the print head and the camera axis. Measurements were made on standard buffed S-3DP™ powder beds, as well as on dense substrates (both polished and rough.) Single droplet spreading was also measured using a Hewlett Packard DoD inkjet print head.

4.2.3 *Varying Infiltration Time Through Mean Pore Size*

The mean pore size of Al_2O_3 powder beds was varied by using three different particle sizes as starting material for S-3DP™ slurries. The powders used were obtained from Ceralox and had the mean particle sizes (after ball milling 20 hours) shown in Table 4.1. The mean particle size of the powders after milling was measured using an Horiba Particle Size Distribution Analyzer CAPA-700. Standard S-3DP™ powder beds were formed from these powders, and their pore size distribution was measured using Hg intrusion porosimetry (Micromeritics Autopore II 9220.)

The infiltration time for each of these powder beds was estimated from time series images captured as described previously. The receding edges of the liquid could be identified from the specular reflections of the strobe light, and an estimate of the total infiltration time could thus be made.

4.3 ***Results***

This section contains the results of the contact angle measurements and the resultant expected liquid extension at equilibrium. This is followed by the variation of the liquid extension with time after impact. The relation between the powder bed pore size and binder infiltration time is examined next. The experimental results relating liquid extension to infiltration time are then presented.

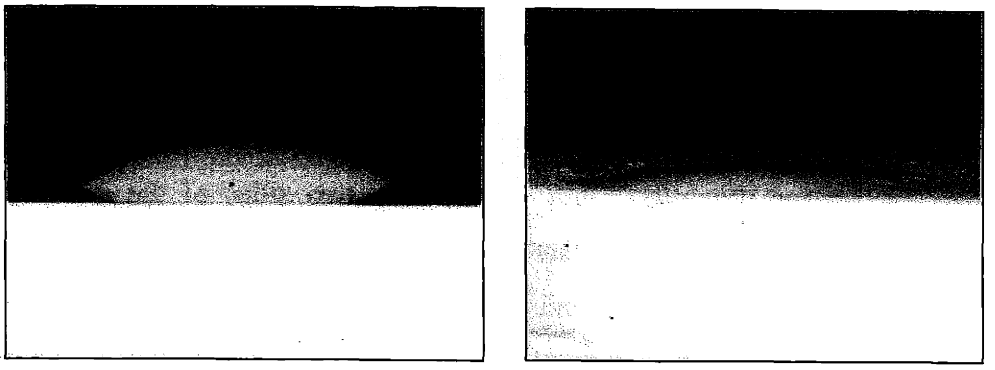

a.) b.)

Figure 4.2: Images of a 2.4 vol.% PAA binder solution drop used for contact angle measurements a.) on a smooth (polished) dense Al_2O_3 surface, and b.) on a rough (as fired) dense Al_2O_3 surface.

Material	Surface Condition	Contact Angle	Predicted Equilibrium Line Width from Spreading (microns)
Al_2O_3	Polished	31	278
Al_2O_3	Rough	10	499
SiO_2	Polished	20	351

Table 4.2: Measured apparent contact angles on dense substrates (binder line dose = 7270 μm^2.)

4.3.1 *Contact Angle Measurements*

Figure 4.2 contains images typical of those used to determine the contact angle of the binder solution on various surfaces. The solution is a 2.4 vol.% PAA binder solution, and the substrate is dense Al_2O_3 (Ceralox HPA 1.0.) The two surfaces in a.) and b.) are identical other than the surface roughness (they are actually two sides of the same disc), clearly illustrating the dramatic effect this factor has on the apparent contact angle. Table 4.2 contains the measured contact angles and the resultant estimated equilibrium spreading widths as determined from Eqn. 4.2 for a printed line of binder. The rough surface should clearly be much more representative of a powder bed surface than a polished surface. The roughness of the actual green powder bed will be higher due to the shrinkage and smoothing that occurs during firing, so the reported rough surface value of the contact angle should be conservatively high. It should be pointed out that the equilibrium width on the rough surface is much larger than the average final primitive width in Al_2O_3 (HPA 1.0) powder beds (~350 μm.) If the rough surface is indeed representative of the powder bed surface, this observation would seem to indicate that the spreading of the liquid does not progress to completion, but rather is interrupted prior to completion by infiltration of the liquid. This would in turn mean that slowing the infiltration would result in a larger liquid line width (greater spreading), up to the limiting case given by Eqn. 4.2, while decreasing the infiltration time would result in a smaller liquid line width down to the limiting case given by the impact (splat) width. The contact angles on polished Al_2O_3 and SiO_2 are also consistent with the liquid spreading hypothesis when viewed in light of the observations of liquid width 3 ms after impact on the respective dense polished surfaces noted in Chapter 3; namely, the liquid width on dense polished SiO_2 was considerably larger than on polished Al_2O_3, as would be expected from the smaller contact angle of SiO_2.

4.3.2 *Liquid Extension with Time*

Figure 4.3 contains a captured strobe image of a CJ printed line of aqueous 2.4 vol.% PAA (10 wt.% glycerol on PAA solids basis) approximately 3 ms after impact with the buffed S-3DP™ Al_2O_3 powder bed (Ceralox HPA 1.0.) Grayscale images lit by separate blue and green strobes were combined to produce the resulting color image, which is the source of the

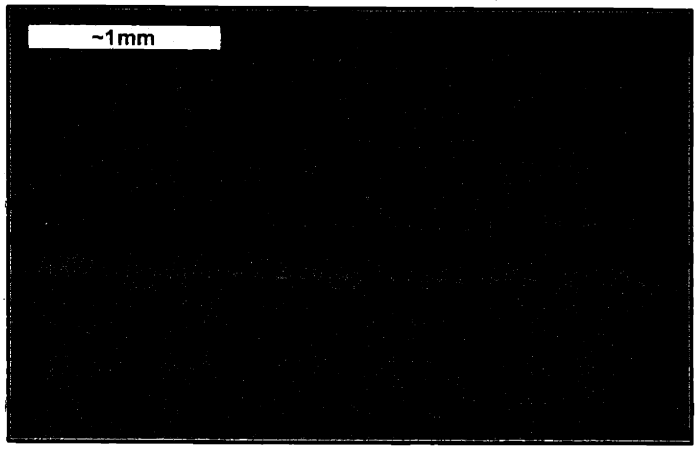

Figure 4.3: CJ printed 2.4 vol.% PAA binder line on the surface of an S-3DP^{TM} powder bed 3 ms after impact.

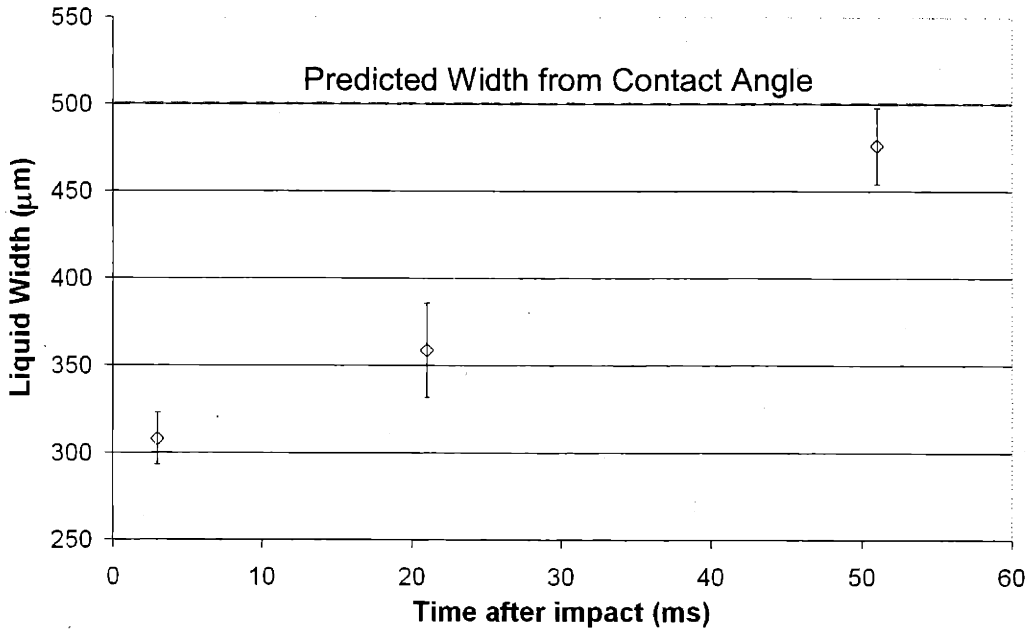

Figure 4.4: Width of a printed 2.4 vol.% PAA binder line on a rough (as-fired) dense Al_2O_3 substrate at various times after impact (see text for a full description).

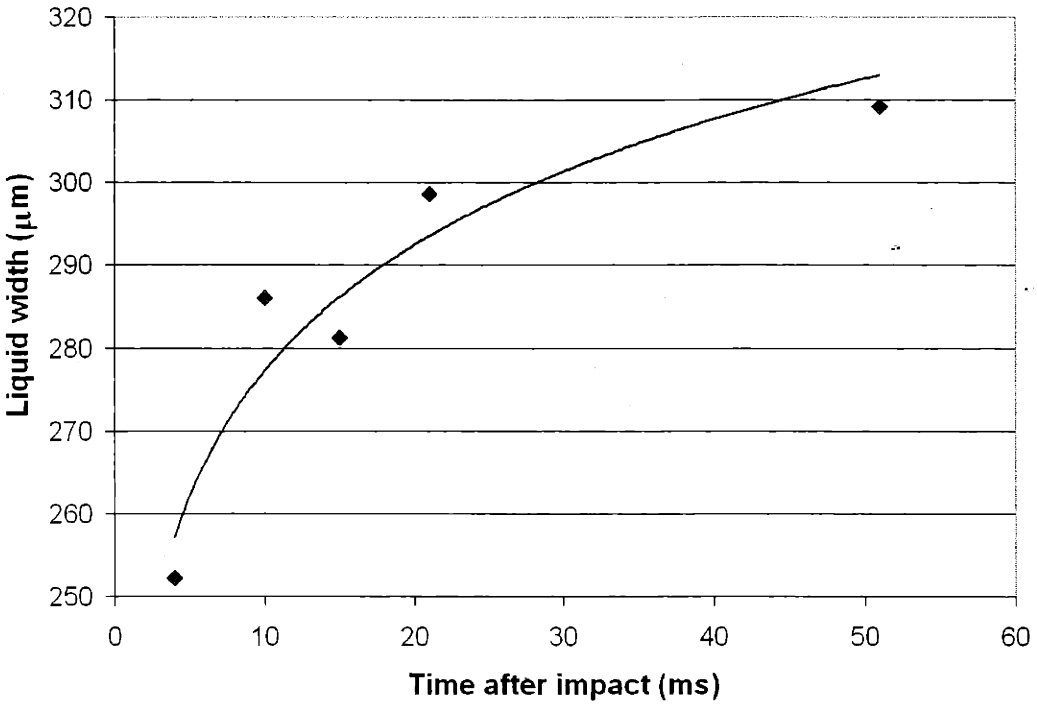

Figure 4.5: Width of a printed 2.4 vol.% PAA binder line on a green Al_2O_3 powder bed at various times after impact (see text for a full description); the curve is drawn to aid visualization.

color cast. The printing conditions were a 0.66 g/min binder flow rate at a droplet generation frequency of 80 kHz (resulting in ~83 μm droplets traveling at ~9 m/s) with a 150 cm/s raster speed (standard CJ printing conditions in S-3DP™.) Figure 4.4 shows the width of a printed binder line at various times after impact on a rough *dense* substrate, similar to those used to measure the contact angle on a rough surface. The liquid extension continues for 10's of ms (or more), long after impact is complete. The width of the printed line on this rough dense surface at 50 ms after impact has already surpassed the observed primitive width in the Al_2O_3 system. Figure 4.5 shows a similar plot on a porous green S-3DP™ powder bed (Ceralox HPA 1.0 Al_2O_3.) The extension is again clearly still progressing 30 ms or longer after impact, indicating that spreading of the liquid is indeed occurring long after impact phenomena are over. The initial spreading rate is quite high, decreasing steadily as infiltration progresses. The width of the liquid at long times approaches the width of actual primitives that have been removed with this system. The width is however still much smaller than the equilibrium spreading width on a rough surface, indicating that the spreading may be stopped short, possibly by infiltration.

4.3.3 Effect of Pore Size on Infiltration Time

Figure 4.6 shows the results of Hg intrusion porosimetry on S-3DP™ powder beds formed from Ceralox HPA 0.5, HPA 1.0, and SPA-TMXX3 high purity Al_2O_3 powders. The mean pore sizes of the powder beds as determined from these analyses are given in Table 4.3, along with the measured infiltration times for binder lines CJ printed under the standard printing conditions given in section 4.3.2. The infiltration time is strongly dependent upon the mean pore size as expected. Figure 4.7 illustrates that the measured infiltration times do indeed exhibit the predicted 1/r dependence on pore size as predicted by Darcy's Law (Eqn.'s 4.3 and 4.4.) Particle size therefore provides an effective means of controlling the infiltration time (through the dependence of pore size on particle size.) The hypothesis that the binder line extension is limited by the infiltration of the liquid can thus be tested using powder beds formed from these three stock powders.

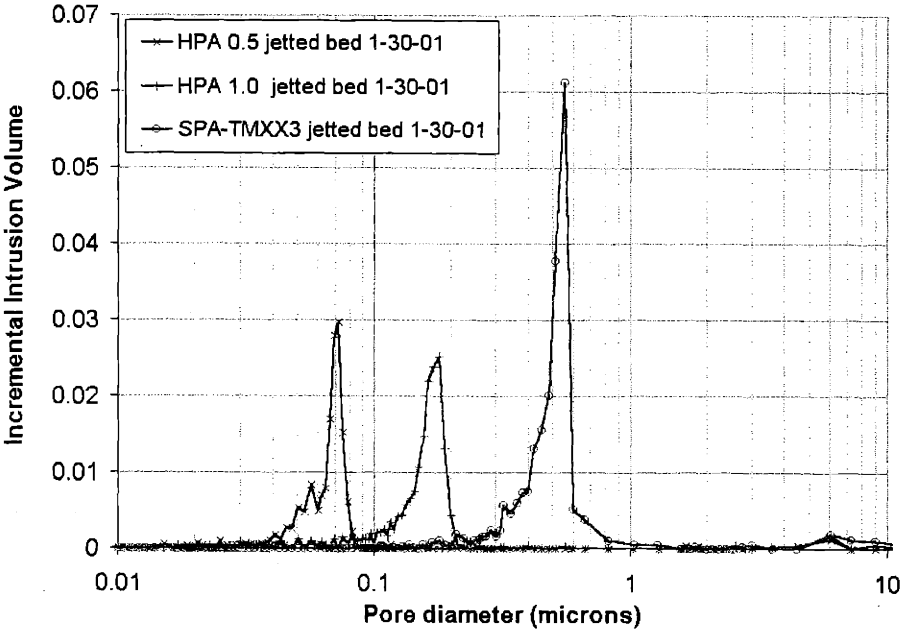

Figure 4.6: Pore size distribution data for S-3DP™ Al_2O_3 powder beds made from Ceralox HPA 0.5, HPA 1.0, and SPA-TMXX3 high purity Al_2O_3 powders.

Sample	Mean Pore Diameter (μm)	Measured Infiltration Time (ms)
HPA 0.5	0.07	100
HPA 1.0	0.17	35
SPA-TMXX3	0.53	8

Table 4.3: Measured infiltration time of a printed binder line on buffed S-3DP™ alumina powder beds with the mean pore sizes given in Figure 4.6 (binder dose = 7270 μm^2.)

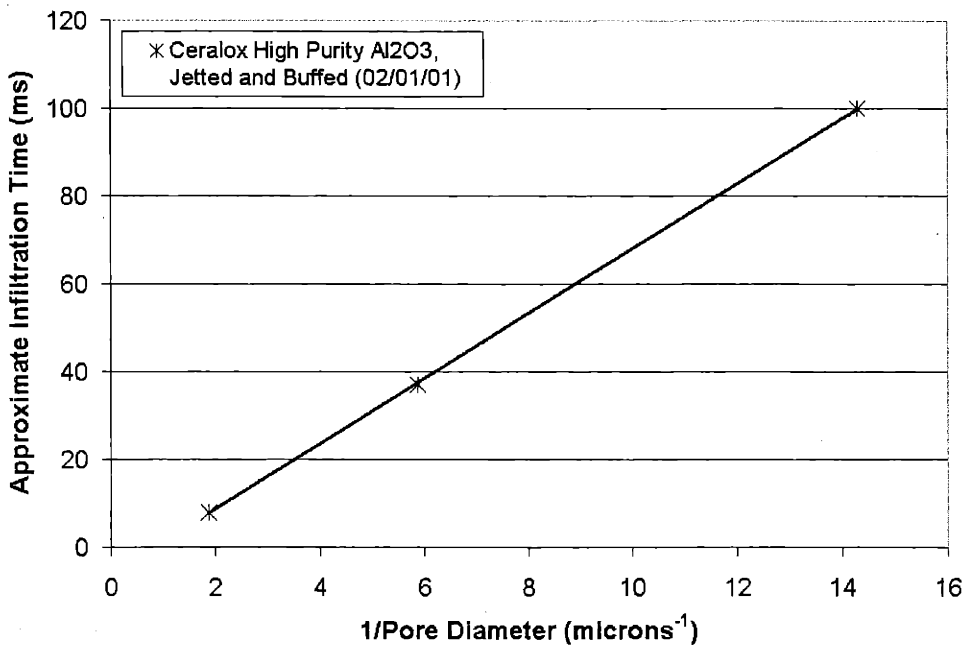

Figure 4.7: Infiltration time dependence on mean pore size of the powder bed, showing the 1/r dependence as predicted.

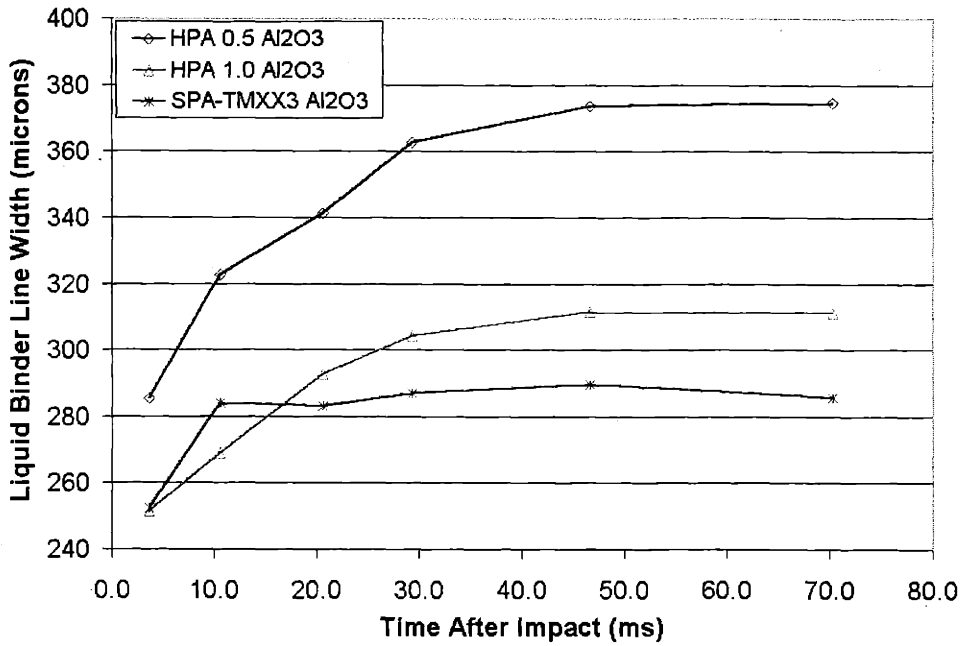

a.)

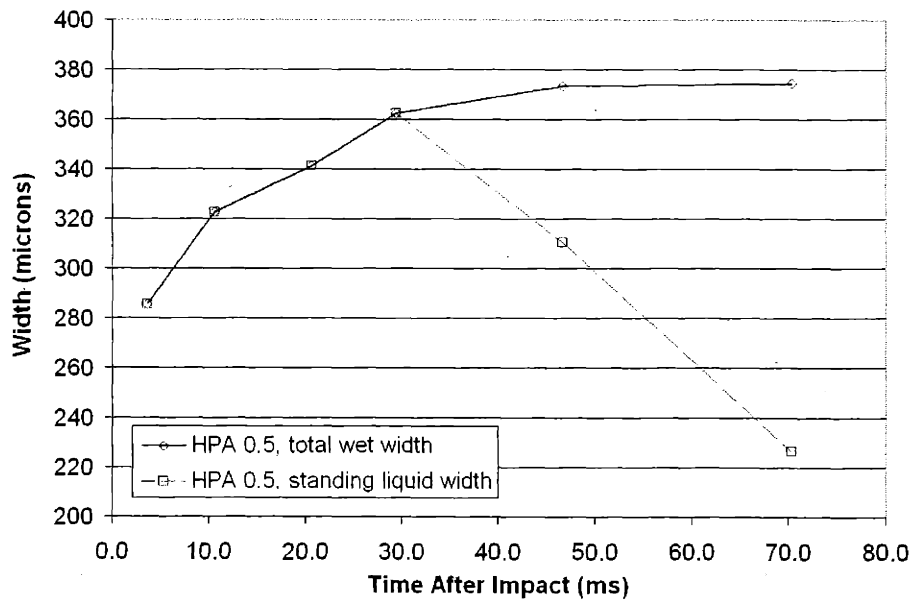

b.)

Figure 4.8: a.) Total wet region width of a printed binder line as a function of time after impact on buffed S-3DP™ powder beds made from HPA 0.5, HPA 1.0, and SPA-TMXX3 Al_2O_3 powders and b.) standing liquid width in HPA 0.5. (lines drawn to aid visualization.)

4.3.4 *Effect of Infiltration Time on Spreading*

The spreading of printed binder lines on the surface of buffed S-3DP™ powder beds made from each of the three stock powders was examined as a function of time after impact. The width at each time was measured using the procedure described previously. All experiments were carried out on the same day to avoid the day-to-day variations discussed in Chapter 3. The results of these experiments are shown in Figure 4.8. If infiltration time is limiting the extension of the liquid, then maximum width of the printed binder line should be largest for the powder bed with the smallest mean pore size and thus longest infiltration time (HPA 0.5), and smallest on the bed with the largest mean pore size and thus shortest infiltration time (SPA-TMXX3.) This is exactly what is observed, as shown in Figure 4.8 a.), which is a graph of the wet region width as a function of time after impact. Spreading of the liquid is halted within 10 ms on the SPA-TMXX3 powder bed due to the rapid infiltration, and as a result the final wet line width is only around 290 μm. The printed liquid bead on the HPA 0.5 bed was observed to continue to spread for ~50 ms, resulting in an ultimate wet line width of 375 μm. The behavior of the HPA 1.0 bed fell between the other two, extending to 311 μm in 35-40 ms. Figure 4.8 b.) shows the variation of the actual *standing* liquid bead width with time on HPA 0.5 (as opposed to 4.8 a., which shows the total width of the wet region.) It can be seen from this figure that the liquid continues to extend up until roughly the point where recession of the liquid occurs due to infiltration, again highlighting the effect of infiltration on printed line width.

A final note should be made about the estimated rough contact angle. It has already been stated that the value on the rough as-fired surface is probably conservatively high. It should also be stated that the roughness of the green powder beds formed from the different particle size powders is not identical, as it will be dependent upon the particle size. This is shown clearly in Figure 4.9. The approximate roughnesses of the powder beds are ~0.5 - 1 μm for HPA 0.5, ~ 1.5 - 2 μm for HPA 1.0, and ~ 4 - 5 μm for SPA-TMXX3. This is a relatively small range of roughness, and the effective contact angle might be expected to decrease slightly with increasing roughness (although the exact behavior is unclear). Thus in the absence of the effects of infiltration time, the lines printed onto the SPA-TMXX3 Al_2O_3

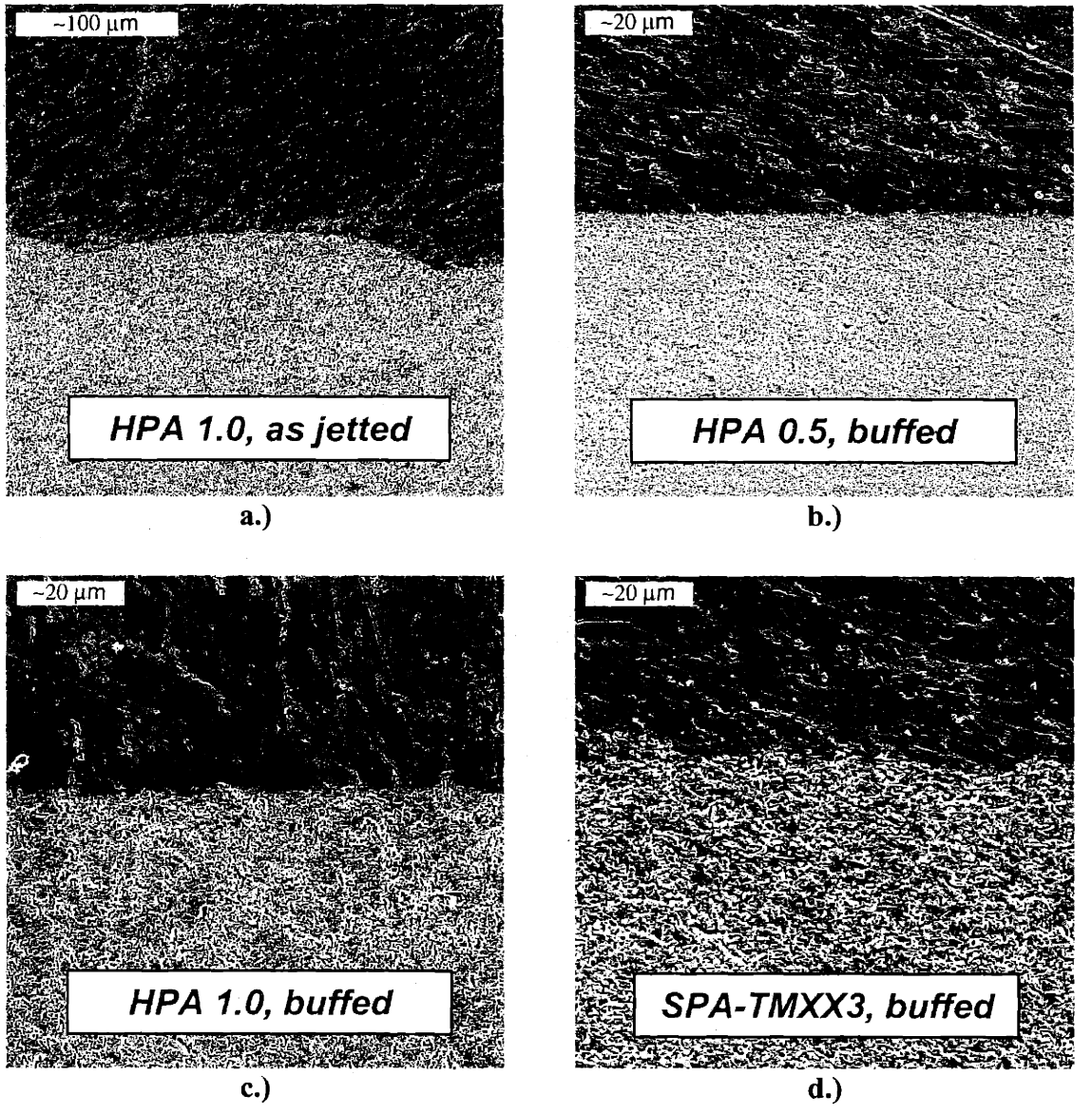

Figure 4.9: SEM photomicrographs showing the roughness of a.) the as-jetted HPA 1.0 bed, b.) the buffed HPA 0.5 bed, c.) the buffed HPA 1.0 bed, and d.) the SPA-TMXX3 bed

powder beds should reach a *greater* ultimate spreading width than HPA 0.5 or 1.0, and the trend would be opposite to that shown in Figure 4.8 a.).

4.3.5 Spreading in DoD Printing

The direct applicability of the above results to DoD printing is not entirely clear, since DoD is practiced in a completely different regime. Droplet velocities can be much slower, and the droplet generation rate is an order of magnitude slower (or more), so that the environment encountered by a droplet upon impact may be vastly different than in CJ printing.

To determine whether spreading is the active factor determining liquid extension in DoD printing, the most extreme case was examined, that of individual droplets infiltrating independent of other printed drops. Droplets of aqueous 2.4 vol.% PAA binder solution (with glycerol) were formed using a Hewlett Packard inkjet print head (model 51626A) from which the ink had been removed and which had subsequently been cleaned with DI H_2O. The waveform chosen to drive the print head was a 2.5 μs square pulse having an amplitude of 13.9 V. This waveform was chosen because it minimized the size and number of satellite droplets (secondary droplets ejected along with the main droplet during a pulse.) The droplet diameter as measured from mass collected in a column over a given time was calculated to be 55 μm. The measured velocity of the droplets at the level of the powder bed was 4.2 m/s. The droplet velocity was measured as follows: a circular disk (~7 cm in diameter) was mounted to the drive shaft of a synchronous motor with a revolution rate of ~2700 rpm. A short vertical baffle 2 mm in height was then mounted on the surface of the disk. The printhead was positioned 1 cm above the disk surface at the edge and turned on with the disk revolving at the known rate. After ~ 1 minute the printhead was turned off. The rotation of the vertical baffle serves to sweep out a region of the binder jet that would otherwise impact the surface of the disk, i.e. a shadow region exists representing the droplets that hit the side of the baffle rather than the surface of the disk. The length of the shadow region was measured, and this length combined with the rotation rate and disk diameter (which give the rotational velocity at the surface of the disk) allows the calculation of the vertical velocity. The droplets were generated at 2 kHz, and the substrate was rastered under the print head at a speed

sufficient to produce complete separation of the deposited droplets on the powder bed (the actual spacing was ~ 750 μm between droplets at a 1.5 m/s carriage speed.) The diameter of the droplet on the surface of the powder bed was measured as a function of time using the DIOS equipment.

Figure 4.10 shows the droplet diameter on the surface of S-3DP^{TM} Al_2O_3 powder beds (Ceralox HPA 0.5 and HPA 1.0, buffed smooth) as a function of time after impact, as well as a time series of droplet images. It is clear from the plot that on both powder beds the extension of the printed liquid progresses long after impact phenomena are complete (~ 10 μs.) The spreading rates on the two powder beds (and so the time dependent drop radius r(t)) are also comparable, however infiltration of the liquid halts the spreading much earlier in the HPA 1.0 powder bed, as expected from the higher infiltration rate on beds made of this particle size powder. Also shown in Figure 4.10 is the approximate expected splat width as predicted by the Asai model (90 μm for a 54 μm droplet.) The Asai model is clearly overestimating the impact splat width for this system. As mentioned in Chapter 3, the Asai model assumes a contact angle of 90° (even though the resulting equation is fit to data having lower contact angles, as was found to not depend on the surface). However a lower contact angle results in a lower surface energy penalty to extend the droplet a given distance, so including the effect of the 10° contact angle would result in an even larger expected maximum splat diameter. Similarly, the modified impact model of Section 3.1.3, which *does* include the effects of contact angle as well as porosity, predicts a maximum splat diameter of 121 μm for a 54 μm droplet, again greatly overestimating the observed splat diameter (the unmodified Chandra and Avedisian model predicts a splat diameter of 142 μm). The discrepancy has as yet not been explained, but could perhaps be related to the time needed for the equilibrium contact angle to be realized (i.e. the effective contact angle at impact may be different from the observed static values, due to adsorption of ions or polymer molecules at the three-phase interface as the liquid advances). In addition, thermal effects, droplet oscillation effects, the morphology of the solid-liquid interface, and the shape of the liquid-vapor interface at the pores have been neglected. The expected equilibrium spreading width is ~160 μm, well below the observed maximum spreading diameters. Figure 4.11 is an SEM image of an actual single drop HPA 0.5 primitive retrieved after these experiments.

4.3.5.1 Model of Droplet Spreading Kinetics

The spreading rate of small droplets on a solid surface is typically characterized by an equation of the following form:[61,62]

$$r(t) = Qt^n \qquad \text{Eqn. 4.5}$$

where:

r = time dependent droplet radius

Q, n = constants

Reported experimental and theoretical values of n generally fall between 0.1 and 0.14,[61,62] however this experimental data is for a somewhat limited range of materials (e.g. silicone oil spreading on glass.) Experimental values of n well outside this range have been reported with other material systems, from as low as 0.033 to as large as 0.314.[63] It is expected that the value of n depends on temperature, humidity, pH, the presence of electrolytes, and surface charges, among others, as well as the roughness of the surface.[63] The majority of the literature data is also for smooth surfaces, and as such the spreading rate has been modeled as limited either by bulk viscous forces in the core of the drop (for which n is predicted to be 0.1) or by molecular dynamics (limited by the rate of attachment of liquid "particles" to the solid surface, for which n = 0.14.)[62,61] Both mechanisms are probably active in real (smooth) systems, and the dominant mechanism may change as spreading progresses.[62] The rate limiting factor for a rough, porous surface, however, could be expected to be different than for a smooth surface. The fact that spreading is interrupted by infiltration of the liquid (i.e. the spreading and infiltration rates are comparable) may indicate that the rate of spreading is at least in part controlled by the micro-topography of the porous surface,[64] and as such could depart from the predicted low values of n, particularly after the initial rapid spreading stage. It has even been predicted that once the spreading becomes controlled completely by the surface topography, the spreading rate should become essentially constant, resulting in a linear increase of r with time (n = 1.)

Eqn. 4.5 clearly assumes an initial contact radius of zero, which is not actually the case (here we assume t = 0 at the point where the impact process ceases, and spreading technically begins.) An alternative form of Eqn. 4.5 has been proposed to account for a non-zero initial radius:[65]

$$r(t) = a(b + t)^n \qquad \text{Eqn. 4.6}$$

where a and b are constants, and n is as in Eqn. 4.5. A curve of this type was fit to the combined early-stage HPA 0.5 data (t < ~1.6 ms) and the early stage HPA 1.0 data (t < ~0.8 ms) in Figure 4.10, with a = 54.073, b = 0.038914, and n = 0.176, and is shown in terms of diameter by the blue curve. The R^2 for this fit is 0.96. 1.6 ms was chosen as the cutoff for the HPA 0.5 data simply because it appears to be in this region that the spreading width begins to plateau; 0.8 ms was similarly chosen for the HPA 1.0 data because it is here that the droplet width begins to recede.

4.3.5.2 Model of Droplet Infiltration

The time-dependent radius of a single drop infiltrating into a porous medium has been developed in reference 59, and is given by Eqn. 4.7:

$$r(t) = r_0\left(1 - \sqrt{\frac{t}{\tau}}\right) \qquad \text{Eqn. 4.7}$$

where:

r_0 = the initial droplet radius

τ = the total infiltration time

This form of r(t) assumes that the droplet starts as a spherical cap initially at its equilibrium radius (given by the droplet volume and contact angle), and recedes from this point as the liquid infiltrates. A modification must thus be made to account for the initially increasing contact radius due to spreading observed in the data of Figure 4.10 (otherwise the drawing area for infiltration will be overestimated in the early stages, resulting in an overestimate of

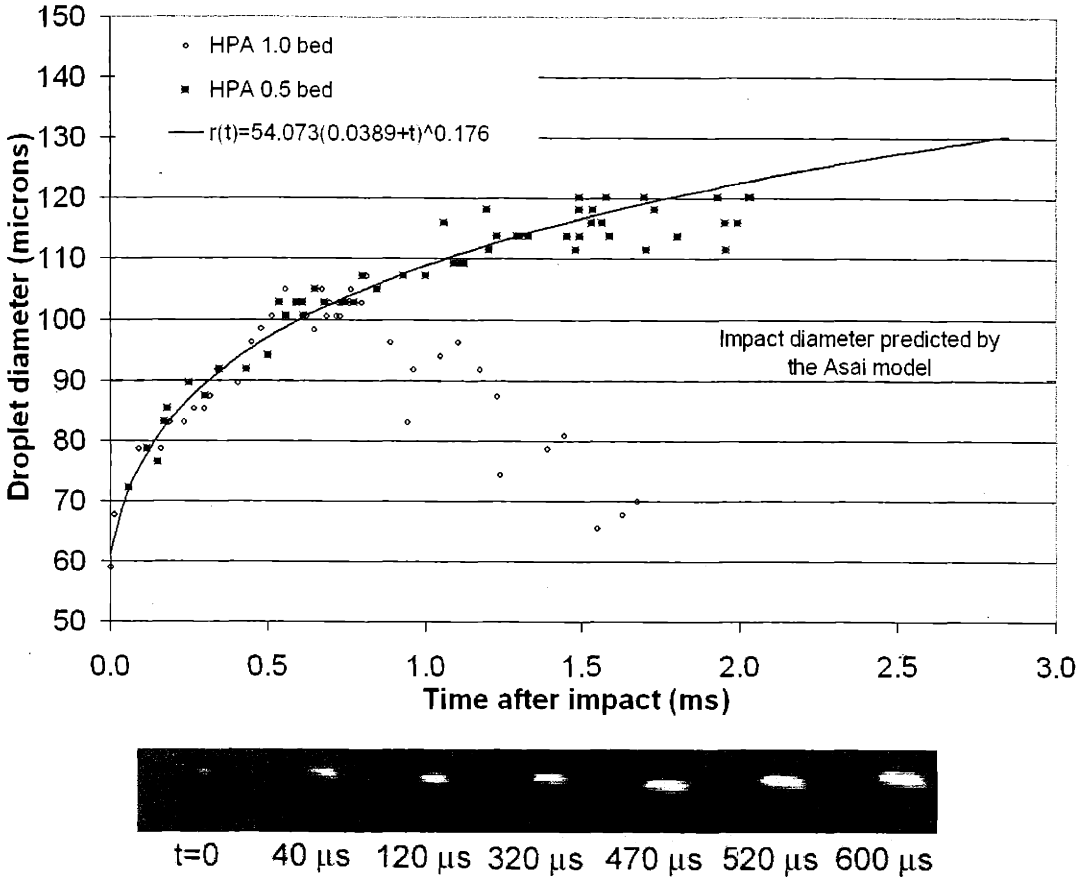

Figure 4.10: Plot of the extension (increase in diameter) of DoD-printed 55 µm single drops of aqueous 2.4 vol.% PAA 60000 binder solution (with glycerol) as a function of time after impact on HPA 0.5 and 1.0 powder beds (see text for details); a time series of droplet images is also shown.

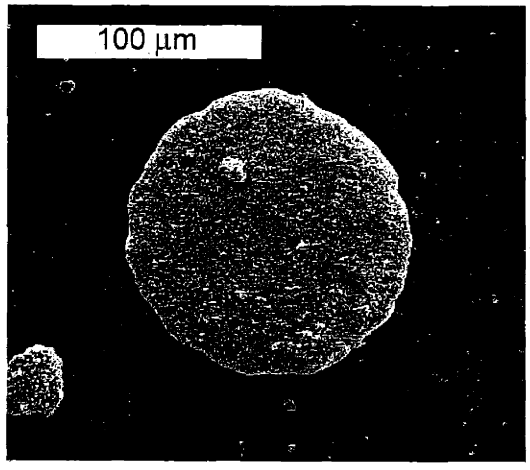

Figure 4.11: Single drop HPA 0.5 primitive retrieved after the experiments in Figure 4.10.

the infiltration rate.) Thus proceeding from the original analysis in reference 59, the differential volume of liquid dV_p drawn into the pores in an annulus between r and r + dr is given by the following equation:

$$dV_p = \pi R_{pore}^2 \cdot dh_p \cdot \rho_p \cdot 2\pi r \cdot dr \qquad \text{Eqn. 4.8}$$

where:

R_{pore} = the pore radius (assumed here to be the mean pore radius from porosimetry)

dh_p = the differential penetration depth into a pore

ρ_p = the areal density of pores (number per unit area)

Eqn. 4.8 is simply the product of the volume of liquid drawn into a single pore within the annulus and the number of pores in the annulus. Taking the time derivative of the Washburn equation results in an expression for dh_p:

$$dh_p = \sqrt{\frac{\gamma_{LV} \cos\theta \cdot R_{pore}}{2\eta \cdot t}} \cdot dt \qquad \text{Eqn. 4.9}$$

ρ_p is equal to the area fraction of pores a_p (taken as equal to the volume fraction) divided by the area of a single pore (πR_{pore}^2.)[59] Making these substitutions into Eqn. 4.8 results in the following form for dV_p:

$$dV_p = \kappa \frac{r}{\sqrt{t}} \cdot drdt \qquad \text{Eqn. 4.10}$$

where:

$$\kappa = \pi a_p \sqrt{\frac{\gamma_{LV} \cos\theta \cdot R_{pore}}{2\eta}} \qquad \text{Eqn. 4.11}$$

Thus the total volume infiltrated $V_p(t)$ is given by the following double integration:[59]

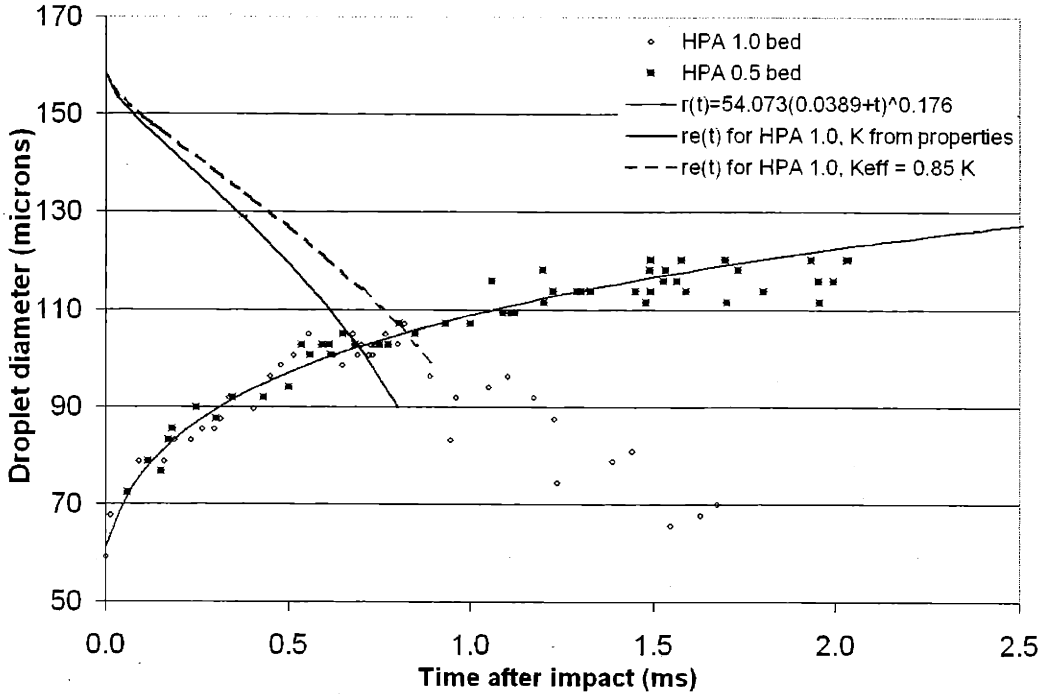

Figure 4.12: Plot showing the expected equilibrium drop radius $r_e(t)$ for the volume of liquid remaining on the surface as a function of time for κ as calculated from the bed properties (solid black curve) and for an effective κ, $\kappa_{eff} = 0.85\kappa$ (dotted black curve); the intercept with the general spreading curve gives the ultimate spread width predicted by the model developed in the text.

$$V_p(t) = \kappa \int_0^t \int_0^{r(t')} \frac{r}{\sqrt{t'}} dr dt' \qquad \text{Eqn. 4.12}$$

Integration over r results in the following equation:

$$V_p(t) = \frac{\kappa}{2} \int_0^t \frac{r^2(t')}{\sqrt{t'}} dt' \qquad \text{Eqn. 4.13}$$

At this point a functional form of the droplet radius as a function of time, r(t), during spreading is needed. r(t) has already been expressed during spreading by Eqn. 4.6, so this term can be substituted directly into Eqn. 4.13:

$$V_p(t) = \frac{\kappa}{2} \int_0^t \frac{\left(54.073(0.038914 + t')^{0.176}\right)^2}{\sqrt{t'}} dt' \qquad \text{Eqn. 4.14}$$

Eqn. 4.14 can now be used to calculate the volume of liquid infiltrated as a function of time during the spreading of the printed droplet. The volume remaining on the powder bed surface (i.e. the volume remaining in the spreading spherical cap of liquid) can then be determined from the initial droplet volume. At the point at which spreading stops the contact angle should pass from the advancing value through the static contact angle and to the receding contact angle. Thus the liquid should for this one instant have the expected equilibrium shape, and the radius will equal the equilibrium value for the volume of liquid remaining on the surface at time t, $V_s(t)$; after this instant the liquid will begin to recede. The equilibrium radius $r_e(t)$ for the remaining liquid volume $V_s(t)$ can therefore be plotted as a function of time using Eqn. 4.1, and the point where it intercepts the general spreading curve given by Eqn. 4.6 will give an estimate of the expected maximum droplet extension r* for a given value of κ, as calculated by Eqn. 4.11. This curve (in terms of diameter) is plotted in Figure 4.12 (the black solid curve) for the HPA 1.0 powder using experimentally determined values of the various parameters in Eqn. 4.11, along with the spreading curve and the original width data; the integration in Eqn. 4.14 was carried out numerically using Mathcad™. The

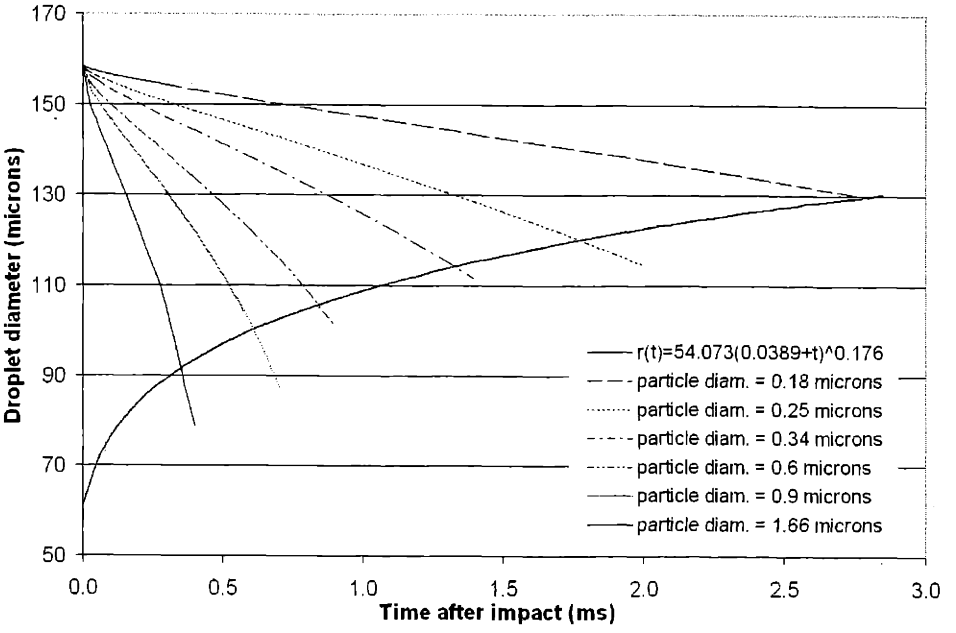

Figure 4.13: Predicted $r_e(t)$ curves (equilibrium radius for the volume of liquid remaining) for various Al_2O_3 particle sizes produced from the model outlined in the text, using the adjusted κ_{eff} (=0.85κ.)

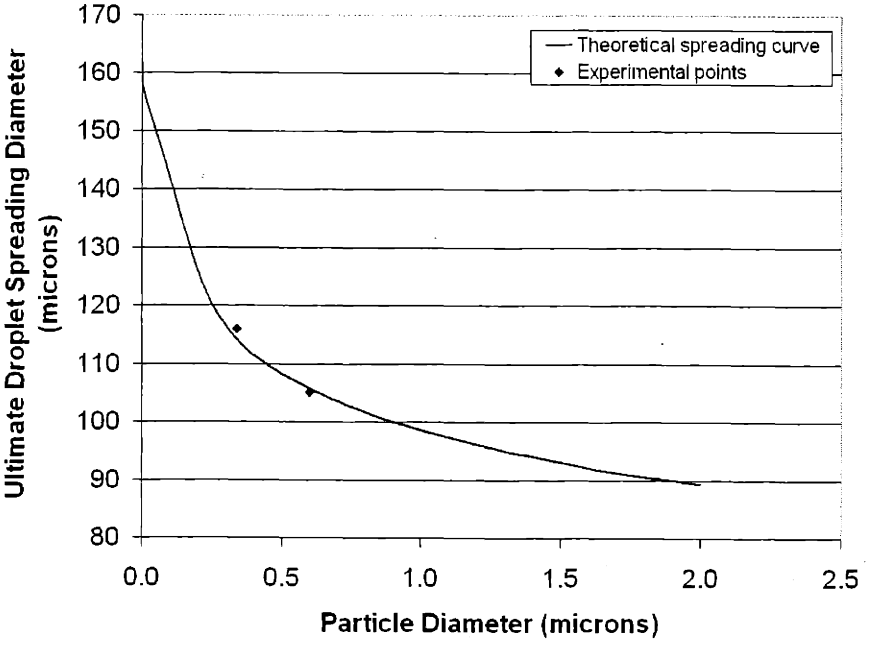

Figure 4.14: Theoretical ultimate spread diameter of a 54 μm drop on an Al_2O_3 powder bed as a function of particle size; two experimental points are shown for comparison.

ultimate spread width as predicted by the intercept of these two curves slightly underestimates the actual observed ultimate spread width. This is most likely attributable to the use of the mean pore radius as determined from Hg porosimetry in calculating κ, which typically results in overestimates of the powder bed permeability. Using an effective value of κ, $\kappa' = 0.85\ \kappa$, however, produces the correct ultimate spread width, as shown by the black dotted curve in Figure 4.12. This is equivalent to simply using an effective permeability. The κ correction can now be used to generate similar curves for various particle sizes, assuming estimates of the pore size and pore fraction can be made based on the particle size, i.e. expressions can be formed of the type $R_{pore} = f(R_{particle})$ and $X_{pore} = f(R_{particle})$.

The pore size in the powder bed is expected to vary ~linearly with particle size, which is confirmed by experimental values of the particle and pore sizes for the HPA 0.5, HPA 1.0, and SPA-TMXX3 powders and powder beds. Thus a simple relation $R_{pore} = f(R_{particle})$ can be used to predict the pore size for a particular particle size. The relation between pore fraction and particle size is however much more complex. The green density (and so the pore fraction) depends on the casting rate, particle size distribution, particle shape, etc., so no clear relationship between X_{pore} and $R_{particle}$ may exist. The general trend however is that the green density increases as $R_{particle}$ decreases, in part because of the longer casting times that result from the smaller pore radii. Therefore, lacking a true functional relationship between green density and particle size, a linear relationship was assumed. The error that results from this assumption is believed to be small over the range of known data, particularly in light of the relatively small differences in pore fraction involved. It does however make extrapolation outside the range of known data (i.e. particle sizes outside of the range 0.34 to 1.66 μm) somewhat more questionable.

Using linear forms for R_{pore} and X_{pore} as a function of particle size obtained from experimental data for HPA 0.5, HPA 1.0, and SPA-TMXX3, $\kappa(R_{particle})$ can be estimated, and so a series of $r_e(t)$ curves (the equilibrium radius for the remaining liquid volume as a function of time) can be produced for various particle sizes, a few of which are shown in Figure 4.13. The intercepts of these curves with the general spreading curve are then used to generate the ultimate spread diameter as a function of particle size, as shown in Figure 4.14. Also plotted

in Figure 4.14 are the experimental points for droplet spreading on Al_2O_3 powder beds, and the agreement between theory and experiment is quite good.

4.3.5.3 Effect of Contact Angle

The apparent contact angle of the printed binder solution on the powder bed would seem to be one of the most effective means of controlling the line width. The strong effect of θ at equilibrium on the spread width is clear from Figure 4.1. The effect of the equilibrium contact angle θ_e during the early stages of spreading is however less clear, and has not received much treatment in the literature. This is because the spreading rate depends not strictly on θ_e, but rather on the difference between the instantaneous advancing contact angle $\theta_a(t)$ and θ_e. The majority of the literature has therefore focused on the variation of $\theta_a(t)$ with time, often completely disregarding the effects of θ_e by using completely wetting materials ($\cos\theta_e = 1.$) A number of treatments however eliminate $\theta_a(t)$ from the rate expressions via the following geometric approximation for θ_a in terms of the instantaneous spherical cap radius r_s and the total volume of liquid V:[65,66]

$$\theta_a \approx \frac{4V}{\pi r_s^3} \qquad \text{Eqn. 4.15}$$

which is a reasonable approximation for small droplets (i.e. gravity effects can be neglected) at contact angles < 90°.[66] Summ et al., assuming bulk viscous force controlled spreading and making use of Eqn. 4.15, have proposed the following expression for radial spreading of a droplet in cases of incomplete spreading:[66]

$$\frac{dr}{dt} = \frac{16V^3\gamma_{LV}}{\kappa\pi^3\eta r^9}\left[1 - \left(\frac{\pi\theta_e r^3}{4V}\right)^2\right] \qquad \text{Eqn. 4.16}$$

From Eqn. 4.15 it is clear that the second term in brackets in Eqn. 4.16 represents the square of the ratio of the equilibrium contact angle θ_e to the advancing contact angle θ_a. During the early stages of spreading (when $\theta_e << \theta_a$), the second term is expected to be quite small for relatively small equilibrium contact angles, and so the effect of equilibrium contact angle on

the spreading rate is also expected to be small (θ_a is taken to be 90° at the onset of spreading, i.e. upon the completion of impact.) The effect of contact angle on spreading rate (and thus on cap radius) is however much stronger as θ_a approaches θ_e, and for large values of θ_e. This is of course clear when considering the effect of contact angle on the final (equilibrium) cap radius. A quantitative application of Eqn. 4.16 to the conditions found in DoD printing in S-3DP™ is of little utility, since among other simplifying assumptions, Eqn. 4.16 assumes purely bulk viscous force controlled spreading kinetics, for which n in Eqn.'s 4.5 and 4.6 should take a value of 0.1. It can however give a picture of the expected qualitative behavior.

More insight is perhaps gained simply by examining the effect of θ_e on the equilibrium spread diameter, which represents an upper limit on droplet size. For example, engineering of the surface chemistry to produce an effective equilibrium contact angle of 55° results in an equilibrium spherical cap diameter of 90 μm for a 54 μm droplet. This is almost 50 % smaller than the current equilibrium value, and is 13 μm and 28 μm smaller than the maximum spread diameter (*including* the effects of infiltration) measured on HPA 1.0 and HPA 0.5 powder beds, respectively; infiltration of the liquid should in turn result in even smaller maximum spread diameters. The only real upper limit on the choice of contact angle is the requirement that the liquid still infiltrate (i.e. $\theta_e < 90°$), although the infiltration rate will decrease at large contact angles, which could result in impractically slow droplet generation rates if complete infiltration between droplets is desired. As an example, increasing the ideal contact angle on the particle surface from 30° to 55° increases the infiltration time by ~1/3, while an increase from 30° to 80° triples the infiltration time.

4.3.5.4 Effect of Volume on Spreading

The radius of the spreading spherical cap as a function of time $r_s(t)$ is predicted to scale with droplet volume as $\sim V^{0.3}$ for incomplete wetting ($\theta_e > 0°$) for the case of bulk-viscous force limited spreading dynamics.[61-63,65,66] This of course may not be the rate limiting factor in the current case, but could still provide some insight into the expected behavior of the maximum droplet extension with droplet radius. A spreading time series was carried out with a DoD droplet diameter of ~ 63 μm. This data is plotted in Figure 4.15 along with the original spreading data for a 54 μm droplet, the original spreading master curve (r(t) vs. t),

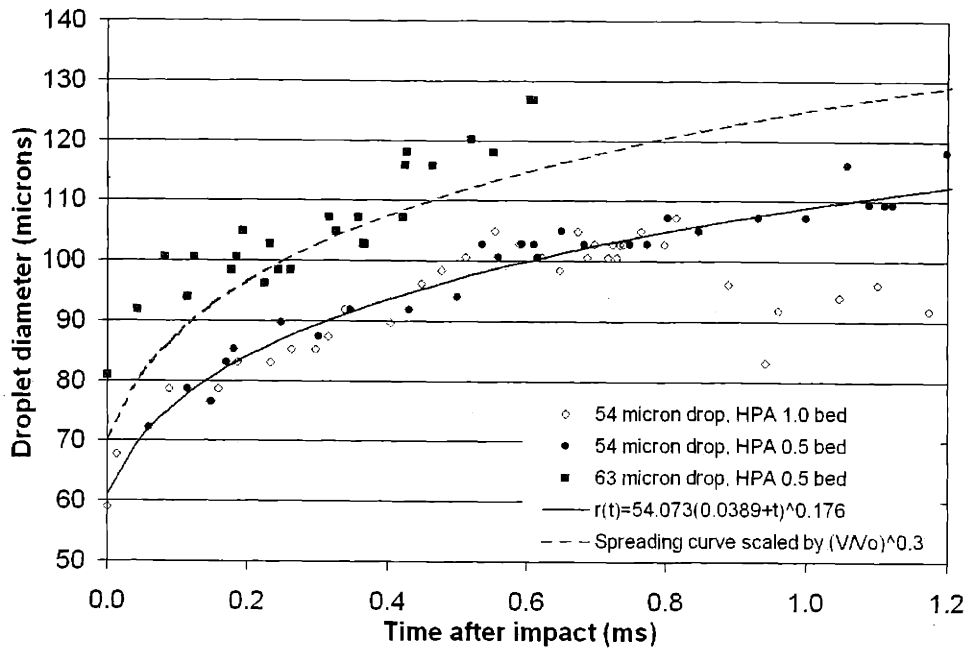

Figure 4.15: Comparison of the droplet radius as a function of time for droplets having initial radii of 54 μm and 63 μm, respectively, showing the effect of droplet volume on spreading. The dotted red curve results from scaling the previously defined scaling curve for a 54 μm droplet (solid blue curve) by the expected $V^{0.3}$ dependence.

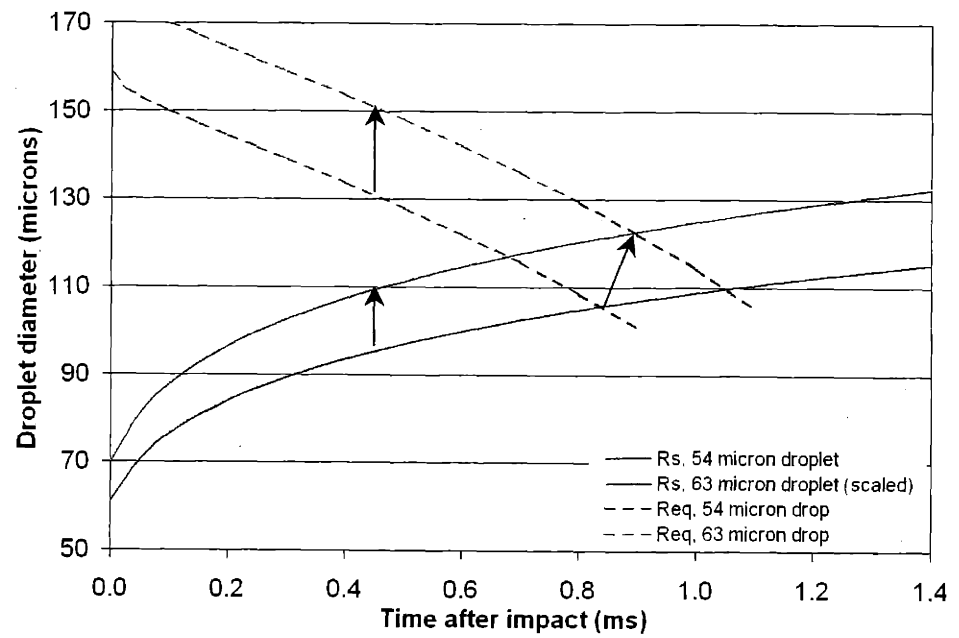

Figure 4.16: Plot showing the effect of increasing the droplet diameter from 54 to 63 μm on both the spreading curve ($r_s(t)$) and the equilibrium radius curve ($r_e(t)$), and thus on the predicted maximum spread diameter, i.e. the intercept of the two curves.

and the expected spreading curve for a 63 μm droplet based on the $V^{0.3}$ dependence. It appears that a $V^{0.3}$ dependence may slightly underestimate the effect of droplet size on spreading rate, at least in the early stages of spreading (a $V^{0.4}$ dependence appears to more closely approximate the experimentally observed dependence, however there is no theoretical justification for this value). Continuing from the predicted $V^{0.3}$ dependence, the equilibrium radius as a function of time can then be predicted from the volume of a 63 μm droplet and integration of the volume of liquid infiltrated over the new r(t) curve, as was done previously for a 54 μm droplet. The effect of changing the droplet size from 54 μm to 63 μm on the spreading curve r(t) and the equilibrium radius curve $r_e(t)$ is shown in Figure 4.16. The new intercept between r(t) and $r_e(t)$ is ~ 17 μm higher than for the 54 μm droplet. Of particular interest is the fact that the ratio of the predicted maximum spreading diameters is almost identically equivalent to the ratio of the initial drop diameters (1.17 in both cases), indicating that the maximum spread diameter may scale ~linearly with droplet size even though both the spreading and infiltration curves are shifted. The radius at equilibrium similarly scales as $V^{1/3}$, as shown in Eqn. 4.1, and so the equilibrium spherical cap radius scales linearly as the initial drop radius, which is again very similar to the observed behavior. Ultimately, this result simply illustrates the need to start with the smallest droplets possible. It also indicates that the optimum set of printing conditions (e.g. droplet generation frequency) may be those that give complete infiltration of an individual droplet before the next droplet is deposited, i.e. the volume of liquid spreading on the surface at any given time is always kept to a minimum. By avoiding conditions where several overlapping droplets are allowed to coalesce prior to complete infiltration the effective maximum liquid spread width can be reduced to approximately the maximum spread diameter of a single isolated droplet.

4.4 Summary

The results presented in this chapter show that spreading of the printed binder solution (driven by simple wetting) on the powder bed surface after impact and coincident with the liquid infiltration determine the ultimate extent of the binder solution (printed liquid line width or droplet diameter) in both CJ printing of lines and DoD printing of drops on S-3DP™

beds. This is contrary to what had previously been supposed, namely that impact phenomena largely dictated printed line width. It was also successfully shown that the printed line width could be controlled by varying the liquid infiltration time, e.g. by changing the mean pore size in the powder bed (as was done in this study.) Two extremes in behavior can be predicted, namely infiltration rate limited (total spreading), which would give the widest width as given by the equilibrium contact angle, and spreading rate limited (zero spreading due to very rapid infiltration), which would give a primitive width controlled by the impact splat width. It is also apparent that simply minimizing the droplet size via DoD may be a necessary but *insufficient* step toward obtaining the smallest possible primitive widths. It is also desirable to minimize the volume of spreading liquid at a given time. The printing of isolated droplets that infiltrate *completely* prior to the impact of the next droplet (rather than many overlapping droplets coalescing and collectively spreading) may present the means of obtaining the ultimate in narrow primitive width, other things being equal, because the smallest volume of liquid is spreading. This will effectively limit the observed ultimate spread width to that of a single droplet spreading independently of the others. Engineering of the surface chemistry to produce a large effective contact angle on the powder bed surface will result in still further decreases in liquid extension.

The effect that changing the particle or pore size has on the binder solution *within* the pore space of the powder bed (i.e. during and after infiltration) remains to be examined. Characterization of this effect is accomplished by looking at the actual primitives retrieved from the powder beds used in the above experiments. This is addressed in the next chapter, where the effects of surface area and particle surface chemistry on the resulting primitive structure are examined in detail.

Chapter 5: Polymer Adsorption during Infiltration

The focus up to this point has been on processes occurring mainly on the surface of the powder bed. We turn in this chapter to the processes occurring *within* the powder bed during infiltration of the printed polymeric binder solution. This study began after large differences in primitive size (cross sectional area) and shape were observed between different ceramic materials, even when the systems had similar packing density, particle size and particle surface area, and identical printing conditions were employed. Primitives in SiO_2 powder beds, for example, are much larger than the corresponding primitives in Al_2O_3 powder beds, while the size of TiO_2 primitives are intermediate between the two. It was initially attributed to drainage in the pore space, however the Al_2O_3 primitives under certain conditions are *smaller* than the size necessary to just accommodate the volume of liquid printed (i.e. smaller than the size that would indicate 100% saturation of the available pore space.) The SiO_2 primitives on the other hand are much *larger* than the size expected at 100% saturation. Similar differences were later observed within a single ceramic system but with different particle sizes (and thus surface areas.) Primitives in Al_2O_3 powder beds composed of smaller particles are much smaller than when more coarse powders are used. The shape differences among primitives could perhaps have been attributed to differences in wetting (wider spreading on the surface should produce a thinner primitive and thus the observed shape differences), however this would not account for the large variations in primitive cross sectional area (volume per unit length.) This chapter presents a hypothesis that was developed to explain this behavior based on polymer adsorption and then tests the hypothesis from several different standpoints.

5.1 Polymer-Ceramic Surface Interaction

The surface of a ceramic particle takes on a charge when in contact with an aqueous solution, the exception being when the pH of the medium corresponds to the isoelectric point,

or IEP, of the ceramic surface.[†] The charge can arise for example from unequal dissolution of the ionic species making up the solid.[69] The sign and magnitude of this charge depends on how far from (and on which side of) the IEP the pH of the solution is. The surface charge is positive at pH values below the IEP, and negative above the IEP. It will thus be energetically favorable from an electrostatic standpoint for charged species in the solution with a charge opposite to that of the surface to adsorb to the ceramic at pH's away from the IEP. This is the source of the double layer of charge and is the basis for electrostatic stabilization of ceramic suspensions.[56,69]

The polyacrylic acid used as a binder in S-3DP™ partially dissociates in solution, resulting in negatively charged polymer chains. The resulting pH of aqueous PAA solutions is typically ~2-3 depending on PAA concentration. A strong (positive or negative) electrostatic interaction should therefore be expected between the ceramic surface and the charged polymer chains when the surface is submerged in the low pH PAA solution (unless the solution pH happens to be very close to the IEP of the ceramic surface.) The interaction/adsorption of charged polymer molecules onto a surface is somewhat more complex than with simple ions due to conformational issues, multiple binding sites on a given molecule (the molecule can be anchored to the surface at several sites along the chain), entropic considerations, et al.[69] The topic has however received extensive treatment in the literature.[70-75]

5.1.1 Filtration by Adsorption

A hypothesis to explain the differences in primitive shape and cross sectional area was developed based on interaction between charged ceramic surfaces and the charged polymer (PAA) chains. The ceramic surface will become charged upon contact with the binder solution (assuming the solution pH is not at the IEP of the ceramic), and as infiltration progresses, the charged polymer molecules adsorb to the ceramic surface. They are thus effectively "filtered" from the binder solution, lowering the local polymer concentration

---

[†] Technically, the charge of the ceramic surface is zero at the zero point of charge, or ZPC, while the IEP is the point where the potential at the shear plane is zero, and the two are not quite the same. See e.g. references 67 and 68 for a detailed explanation of the difference. The IEP is what is measured in the electrokinetic sonic amplitude apparatus (ESA) used in this research, so the IEP will be considered here.

remaining. This continues as infiltration progresses until at some point the solution becomes too dilute to bind the ceramic particles. The primitive size would thus be defined not by the extent of the infiltrating liquid, but by the location of this boundary surface where the polymer concentration drops below some critical value. This process is illustrated schematically in Figure 5.1. Differences in the amount of PAA that can adsorb on various ceramic surfaces (due to the affinity of the polymer for the surface, the amount of surface area available, etc.) would then have a direct effect on primitive size.

5.1.2 Approach

The validity of the adsorption mechanism was tested from two standpoints. Three ceramic systems were selected with very different surface chemistries: Al_2O_3, TiO_2, and SiO_2. Stock powders were chosen to minimize any differences other than the surface chemistry between the systems (particle size, surface area, etc.) The adsorption of the PAA 60000 from solution was measured on each of these systems, and the primitive cross sectional area was characterized. The system capable of adsorbing the most PAA should in turn remove the polymer chains from solution more quickly, resulting in a smaller primitive, while conversely systems that adsorb little or no PAA would be expected to exhibit the largest primitive size, other things being equal. In the second part of the study, a single ceramic material was chosen (high purity Al_2O_3) and the particle size was varied to change the surface area in the powder bed (more surface to adsorb on should translate to more rapid filtration of the polymer, and thus a smaller primitive.) The sizes of primitives formed in powder beds composed of three different particle sizes (and thus different specific surface areas) were then characterized. The results of these experiments have been examined and checked for consistency with the proposed theory of filtration as a mechanism for primitive size control.

5.2 Procedure

All primitive size characterization was done on primitives cured and removed from the powder bed as has been outlined in previous chapters. Size comparisons are made based on saturation calculated from the primitive cross section and binder dose, which corrects for

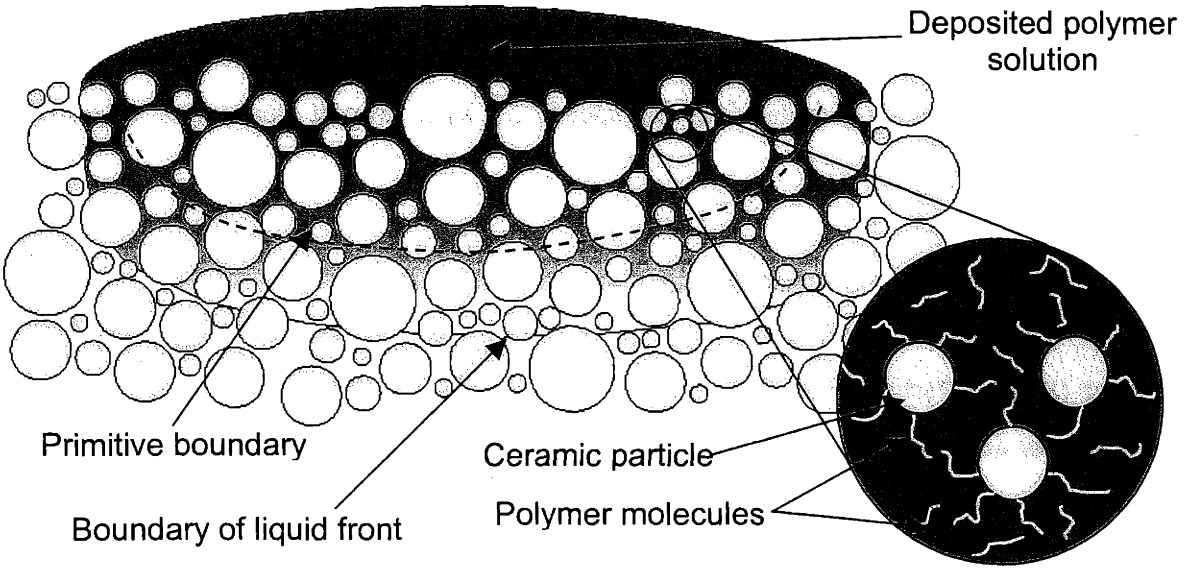

Figure 5.1: Schematic of the filtration of polymer molecules from the printed binder solution during infiltration.

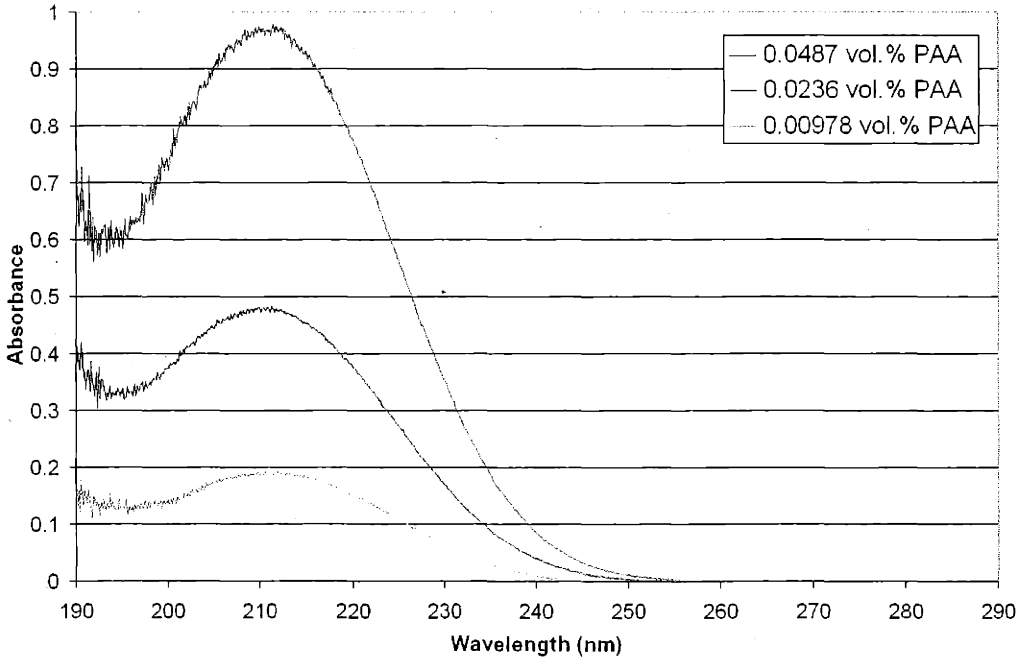

Figure 5.2: Scan of UV absorbance vs. wavelength for three different PAA 60000 (Acumer 1510) concentrations (in DI H_20), showing a characteristic peak at 211 nm.

small differences in green density from one system to the next (Chapter 2.) Primitive cross sectional area measurements are made on polished cross sections in the SEM. All experiments were carried out under standard CJ printing conditions unless otherwise noted (0.65 cc/min, 150 cm/s printhead raster speed, 37 kHz droplet generation rate, 82 μm droplets.)

5.2.1 Characterization of Stock Powders

The particle size of all powders (after milling) was measured using a particle size analyzer (Horiba Particle Size Distribution Analyzer CAPA-700.) The surface area of the powders was determined by BET analysis (Quantachrome BET.) The surface potential was measured as a function of pH for all ceramic systems under investigation using electrokinetic sonic amplitude (ESA) analysis to determine the zeta potential and IEP (Matec ESA system.)

5.2.2 PAA Adsorption Analysis

Adsorption isotherms were prepared on each of three ceramic surfaces under investigation: Al_2O_3 (Ceralox HPA 1.0), TiO_2 (Alfa Aesar), and SiO_2 (Alfa Aesar.) Spectroscopic analysis was used to determine the amount of PAA remaining in solution after contact with the powders. A characteristic peak for Acumer 1510 PAA was identified at 211 nm using UV-VIS absorbance (Beckman DU 640 Spectrophotometer), as shown in Figure 5.2 for a number of different solution concentrations. The linear relation between UV absorbance and concentration was confirmed, and a Bier's law plot (absorbance vs. concentration) was constructed from solutions of known concentration. This plot was subsequently used to determine the amount of polymer remaining in solution after adsorption onto the ceramic powder had taken place (i.e. a subtractive method.)

Ceramic slurries were prepared containing 5, 2.4, 1, 0.5, 0.3, 0.2, 0.1, and 0.05 vol.% PAA 60000 on a total liquids basis (balance DI H_2O.) The solutions were titrated to the pH of the most concentrated solution (5.0 vol.%, pH 2.05) with 1M phosphoric acid, after which 20% ceramic powder (by volume) was added. Phosphoric acid was selected because of the lack of any absorption peaks in the range of interest. A background was also made containing only water and ceramic (also titrated to pH 2.05.) The slurries were ultrasonicated 30 seconds

each with a microprobe sonicating tip at a setting of 30%. The bottles were then sealed with Parafilm and rolled on a ball mill (no media) for 20 hours. The slurries were removed from the mill and centrifuged 1.5 hours at 7000 rpm. The supernatant was withdrawn and again centrifuged for 1.5 hours at 7000 rpm. The supernatant was once more decanted and the solutions were then diluted with a known quantity of DI H_2O to bring the polymer levels within the sensitivity range of the UV-VIS spectrophotometer.

For each supernatant solution, three UV absorbance scans were run and the results averaged. The background was then subtracted, and the absorbance at 211 nm was used to determine the amount of PAA remaining. From this, one can deduce how much PAA has adsorbed onto the ceramic surface. This value was then normalized by the ceramic powder's surface area (as found by BET analysis), and the result (mg adsorbed per m^2 of surface) plotted as a function of solution concentration (i.e. an adsorption isotherm.)

5.2.3 Effect of Surface Chemistry

Primitives were CJ printed into S-3DP™ powder beds formed from each of the three ceramic systems mentioned above (Al_2O_3, TiO_2, and SiO_2.) The average cross-sectional area of the retrieved primitives was measured using SEM images of polished cross-sections and the ImageTool software, as discussed previously. The trends in primitive size were then compared to the PAA adsorption results.

5.2.4 Effect of Surface Area

Three different particle sizes of chemically identical α-Al_2O_3 powders (Ceralox HPA 0.5, HPA 1.0, and SPA-TMXX3) were used to examine the effect of surface area. Primitives were CJ printed into S-3DP™ powder beds formed from each of the three powders, and their average cross sectional area was determined as above. The trends in primitive size with surface area were then evaluated.

5.3 Results

The characteristics of the various stock powders used in this study are given in Table 5.1. The HPA 1.0 Al_2O_3 powder was used to make comparisons based on surface chemistry

Material	Powder	Particle Size (μm)	Specific Surface Area (m^2/g)
Al_2O_3	Ceralox HPA 0.5	0.3	8.6
Al_2O_3	Ceralox HPA 1.0	0.6	4.0
Al_2O_3	Ceralox SPA-TMXX3	1.7	1.2
SiO_2	Alfa Aesar 99.5%	0.7	5.1
TiO_2 (rutile)	Alfa Aesar	0.5	3.5

Table 5.1: Characteristics of the stock powders used in the PAA adsorption studies.

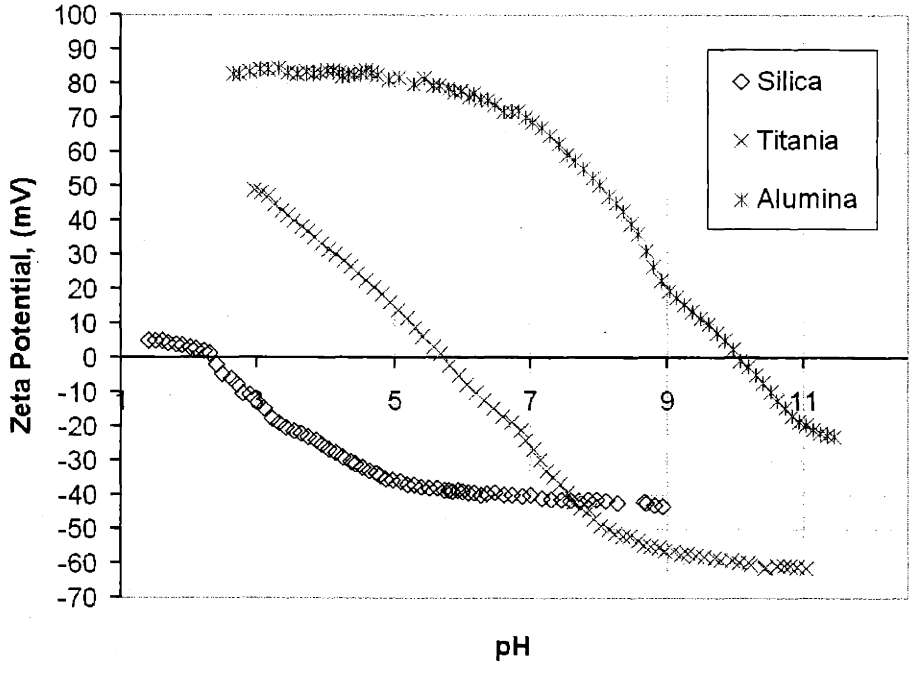

Figure 5.3: Plot of the zeta potential as a function of pH for the three powders used in the study on adsorption dependence on chemistry.

to the TiO_2 and SiO_2 powders, as it has the best match of particle size and surface area. Figure 5.3 contains a plot of the zeta potential of the Al_2O_3, TiO_2, and SiO_2 powders as a function of pH (titrated with nitric acid and potassium hydroxide.) The Al_2O_3 powder has a basic surface, exhibiting an IEP at a pH value of around 10. The Al_2O_3 surface has a strong positive potential at the low pH found in the PAA solutions (~ pH 2-3.) The TiO_2 surface is more neutral and has a lower but still positive charge at pH 2-3. The SiO_2 surface, on the other hand, is very acidic and is near neutral at pH 2-3.

5.3.1 Adsorption Isotherms of PAA

The UV absorbance at 211 nm of aqueous PAA solutions is shown as a function of PAA concentration in Figure 5.4. This graph was used to determine the PAA remaining in solution following the adsorption of some fraction onto the various ceramic surfaces. The amount adsorbed was then deduced knowing the original solution concentration. The adsorption isotherms of PAA 60000 from aqueous solutions onto Al_2O_3, TiO_2, and SiO_2 powders are shown in Figure 5.5 for a solution pH of 2.05.

The adsorption of PAA onto Al_2O_3 is characteristic of a high affinity, type I adsorption isotherm indicating chemisorption with monolayer coverage at ~1.1 mg/m^2.[69] The adsorption onto TiO_2 indicates a much weaker affinity, with adsorbed concentration rising much more slowly (reminiscent of a type II isotherm in gases.) At the concentration of our working solutions in 3DP™ (2.4 vol.% PAA), roughly half as much PAA adsorbed onto TiO_2 as onto Al_2O_3 (~ 0.55 mg/m^2.) There does not appear to be any appreciable adsorption of PAA onto SiO_2. The values calculated were actually negative (~ -0.02), which is of course non-physical. A negative adsorption was calculated because a higher UV absorbance was observed in the supernatant than would result from a solution containing only the starting amount of PAA. It is believed that this is caused by a PAA-assisted leaching of impurity ions from the SiO_2 powder, which in turn raises the solution's UV absorptivity, and being dependent on the presence of PAA, can not be subtracted via the background. This is supported by the fact that the supernatant solutions took on a light orange color which decreased in intensity with decreasing polymer content, and which was not present in the supernatant of the slurry

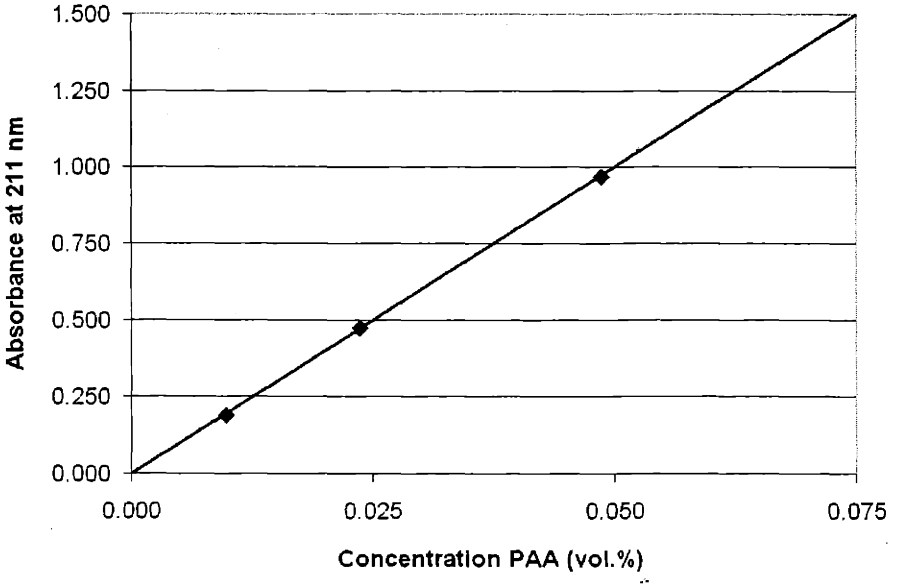

Figure 5.4: Plot showing the dependence of UV absorbance at 211 nm on the concentration of PAA 60000 in aqueous solution.

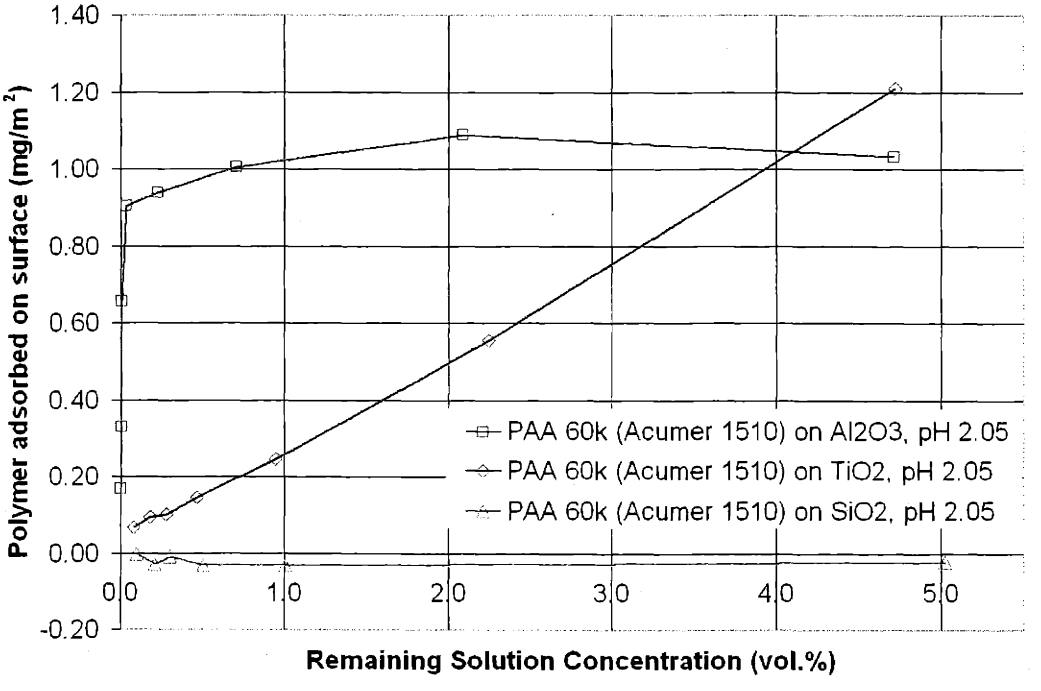

Figure 5.5: Adsorption isotherms of PAA 60000 onto Al_2O_3, TiO_2, and SiO_2 from aqueous solutions at pH 2.05.

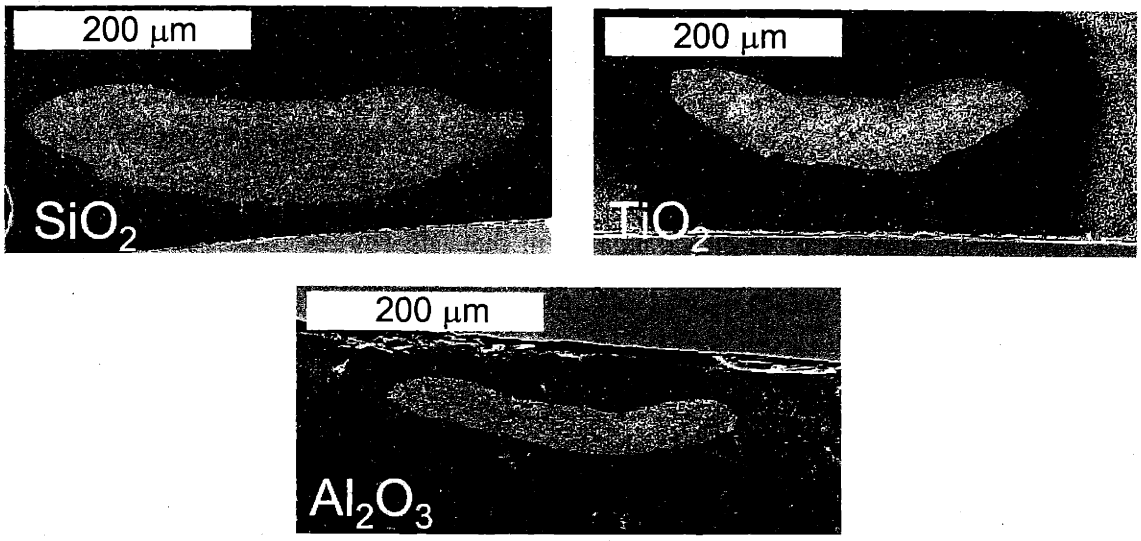

Figure 5.6: SEM's of polished cross sections of primitives printed into powder beds made from the Al_2O_3, SiO_2, and TiO_2 powders used in the PAA adsorption study.

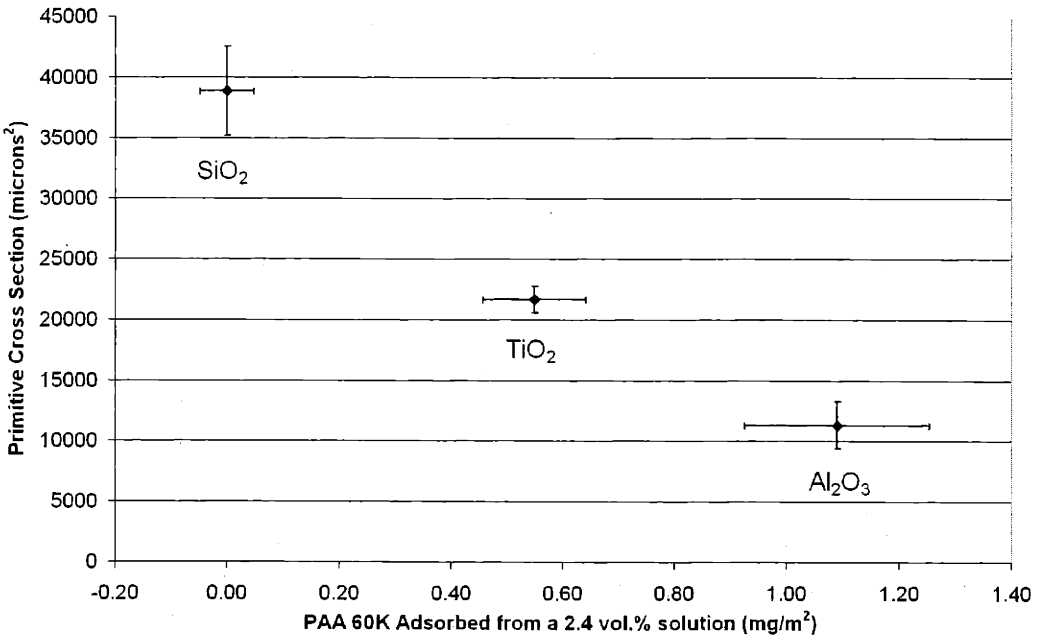

Figure 5.7: Cross sectional area of primitives versus the amount of PAA adsorbed from a 2.4 vol.% solution (normalized by the surface area.)

containing only DI H_2O, SiO_2, and phosphoric acid. The lack of adsorption onto SiO_2 was independently confirmed by total organic carbon analysis on the supernatant solutions from which the adsorption data were generated (Huffman Laboratories Inc., Golden, CO.)

Figure 5.6 contains SEM images of polished cross sections of primitives printed into each of the three systems examined above. The average cross sectional area of these primitives is illustrated in Figure 5.7. The primitive size clearly exhibits the trend expected from the above adsorption results. The system that adsorbs the most PAA at the pH of the binder solution, Al_2O_3, in turn exhibits by far the smallest primitive area. It also results in a very thin primitive, as would be expected for filtration of the binder as it progresses deeper into the powder bed. SiO_2, on the other hand, for which PAA exhibits no affinity, produces by far the largest primitive; again, the SiO_2 primitive is also the thickest, presumably because the binder solution passes down through the powder bed relatively unaffected by the ceramic surface. The behavior of TiO_2 lies intermediate between these two extremes.

5.3.2 Effect of Surface Area

The effect of surface area on primitive size was examined using Ceralox HPA 0.5, HPA 1.0, and SPA-TMXX3 high purity Al_2O_3 powders, whose specific surface areas were given in Table 5.1. Al_2O_3 was chosen because of the high affinity of PAA for the surface, which should make the effects of the filtration by adsorption most pronounced as the surface area is changed.

Figure 5.8 shows SEM's of polished cross sections of primitives CJ printed into buffed S-3DP™ powder beds. The average cross sectional area is shown as a function of surface area in Figure 5.9. The behavior is reminiscent of that shown in Figure 5.7 with variations in surface affinity. The high surface area of the HPA 0.5 powder appears to have filtered the PAA from the binder solution very quickly, resulting in a very thin primitive (~14 μm thick.) The large width of this primitive is due to the long infiltration time resulting from the fine pore size, allowing more time for spreading of the binder solution on the surface of the powder bed, as was explained in the previous chapter. The low surface area powder (SPA-TMXX3) produced the largest as well as deepest primitive, as would again be expected

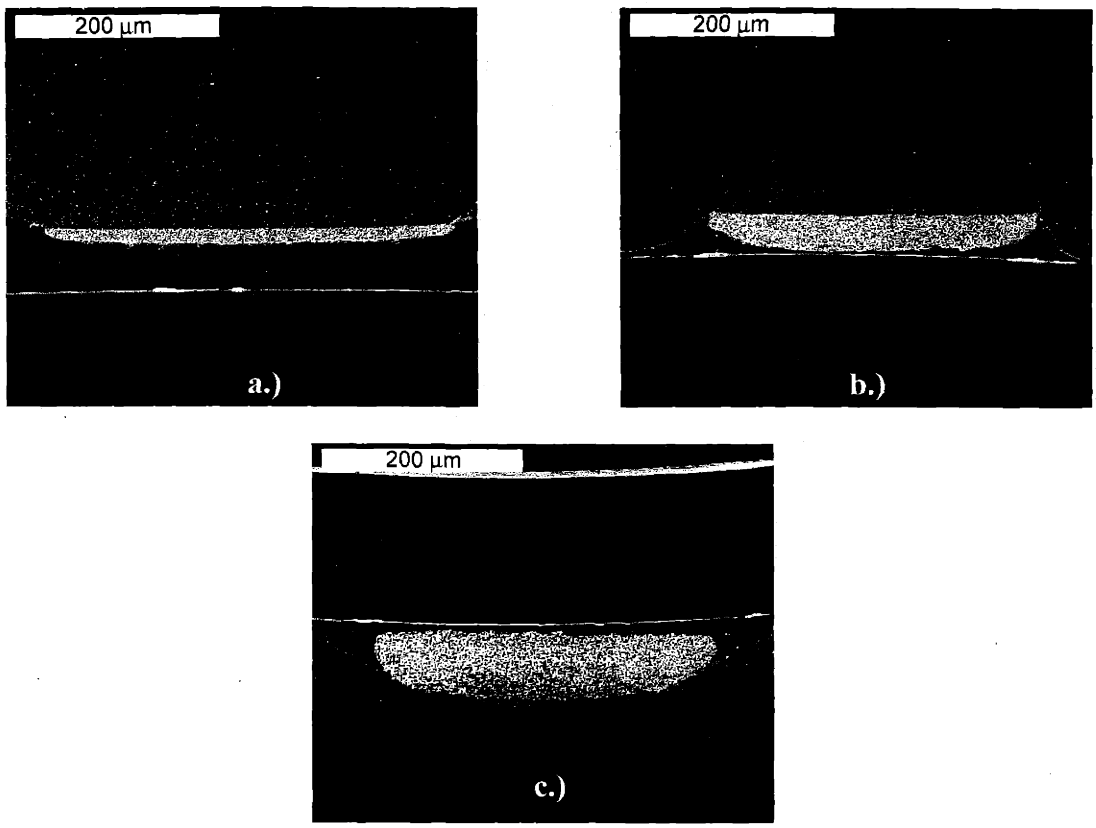

Figure 5.8: Primitives formed under identical conditions in S-3DP™ powder beds made of a.) HPA 0.5, b.) HPA 1.0, and c.) SPA-TMXX3 Al_2O_3 powders (Ceralox.)

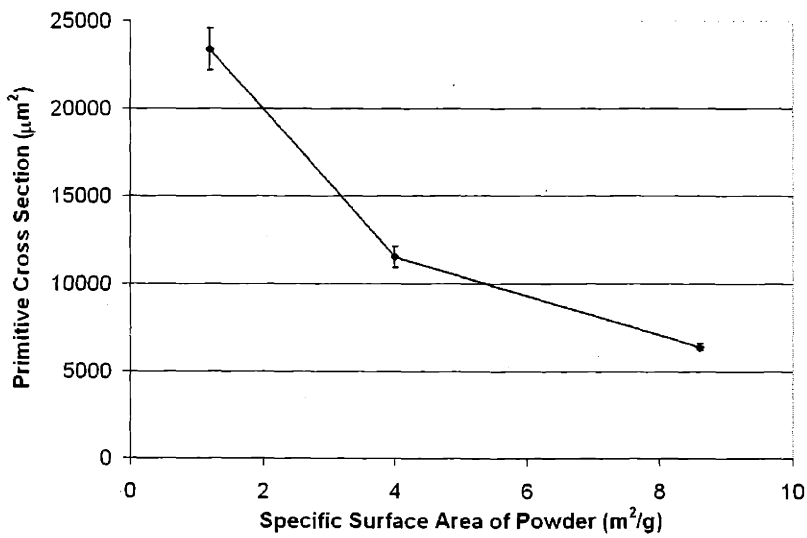

Figure 5.9: Primitive size (cross-sectional area) as a function of powder surface area (from BET analysis) in the Al_2O_3 system (PAA 60000 binder); line for visualization purposes only.

from filtration by adsorption. The powder with a surface area intermediate between these two, HPA 1.0, produced a primitive intermediate in both size and shape between the others.

5.3.3 Summary and Analysis of Results

The results of both sections 5.3.1 and 5.3.2 are in agreement with the hypothesis that filtration of the binder via adsorption during infiltration limits the total primitive size, i.e. the cross sectional area of the primitive. In both cases the ceramic surfaces capable of adsorbing the most PAA, either by way of a greater affinity of PAA for the surface or via a higher surface area, produced the smallest average primitive cross sections. The cross section increased steadily with lower capacity of the respective surfaces to hold PAA.

An alternative means of presenting this data is via the primitive saturation, as discussed in Chapter 2. The cross sectional area data are easy to visualize, however primitive saturation data facilitate meaningful comparisons between systems, because the saturation takes into account the small differences in green density between systems (primitives formed under different printing conditions can also be compared because the saturation includes the binder dose.) It was explained in Chapter 2 that for a given binder dose, a higher saturation ratio indicates a smaller primitive (the actual primitive cross section compared to the binder dose is smaller, which translates to a higher apparent saturation of the pore space.)

Figure 5.10 contains plots of the primitive saturation as a function of a.) surface area in the Al_2O_3 system and b.) PAA adsorbable on the surfaces of Al_2O_3, TiO_2, and SiO_2. The plot of the effect of surface area in the Al_2O_3 system is particularly interesting, as it exhibits a clear linear dependence. This should not be surprising, since increasing the surface area available for adsorption should increase the rate at which PAA is removed from solution by the same ratio. The lower limit of saturation should approach the value in the absence of polymer adsorption (given simply by the equilibrium distribution of the printed liquid in the pore space.) Also of interest is that the primitive saturation in the HPA 0.5 powder is nearly 300%, indicating that the primitive cross section is only 1/3 of that expected for the printed liquid just filling the pore space (in the absence of adsorption.) Conversely, the primitive saturation produced in the SPA-TMXX3 powder bed is only sixty five percent. The fact that the saturation is less than 100% (the value that would correspond to complete saturation of the

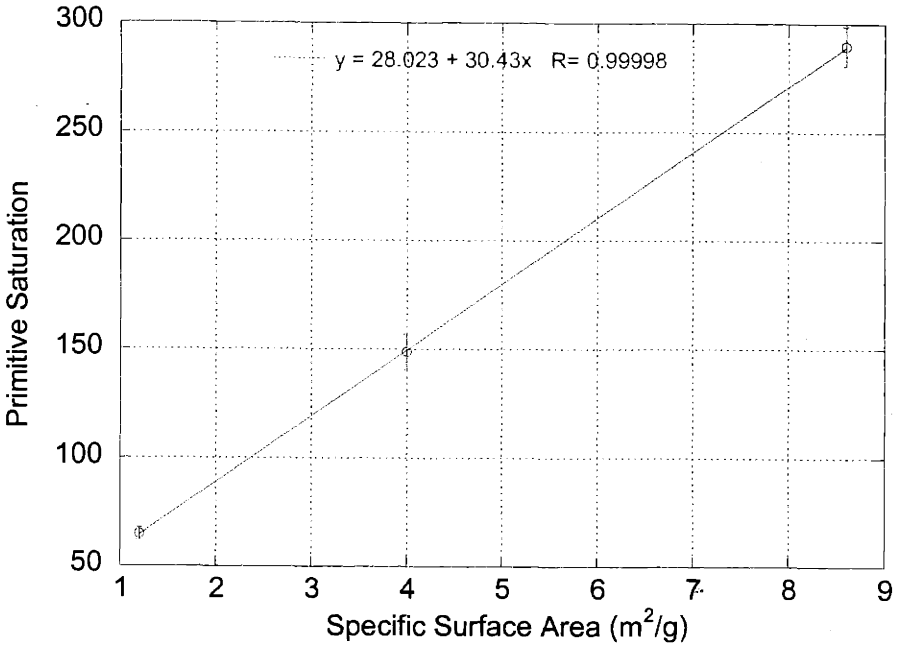

a.)

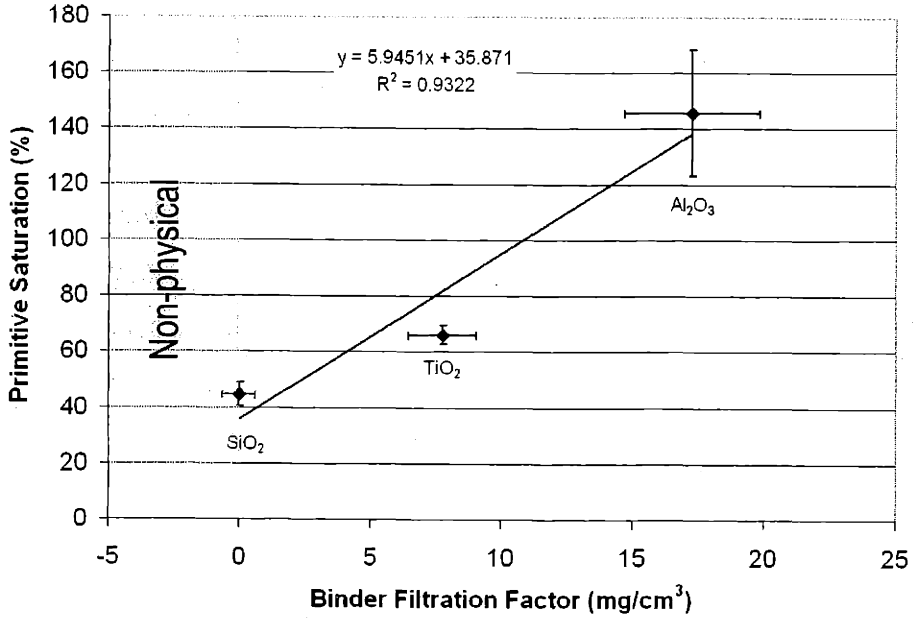

b.)

Figure 5.10: Primitive saturation as a function of a.) surface area in the Al_2O_3 system and b.) the binder filtration factor (as defined in the text) on the surface of various ceramics (binder solution is 2.4 vol.% PAA 60000, aqueous.)

pore space by the printed solution) would seem to indicate that the liquid has "fingered" out through the pore space resulting in a primitive size larger than the space-filling value. The saturation is still however larger than in the non-adsorbing system (SiO_2), which has an even larger primitive (saturation = ~45%.)

For Figure 5.10 b.) a new parameter called the "binder filtration factor," F_B, was defined to include both the differences in the amount of PAA adsorbable per unit area of surface and in the specific surface area of the Al_2O_3, TiO_2, and SiO_2 powders. F_B is defined by equation 5.1:

$$F_B = \overline{M} \cdot \overline{S} \cdot \rho \qquad \text{Eqn. 5.10}$$

where:

$\overline{M}$ = PAA adsorbed from solution at a given initial concentration and pH (mg/m^2)

$\overline{S}$ = specific surface area of the powder (m^2/g)

ρ = density of the ceramic (g/cm^3)

The units of F_B are mg/cm^3, i.e. mg of PAA adsorbable per cm^3 of solid ceramic. The effects of green density are taken into account in the primitive saturation, and so green density is not included in the expression for F_B.

The plot of primitive saturation versus F_B is expected to exhibit a linear dependence similar to the surface area dependence (other things being equal), however the observed behavior differs somewhat. This is almost certainly due to the assumptions made in defining F_B, in particular the implicit assumption of a flat adsorption isotherm. This assumption is valid for high affinity systems like Al_2O_3 - PAA, however Figure 5.5 shows that this is a poor assumption for TiO_2 – PAA. The effect this will have on F_B can be visualized from the following scenario. When the PAA solution first enters the powder bed, the concentration is 2.4 vol.% PAA and the TiO_2 surface can accommodate 0.55 mg/m_2 of PAA *at this concentration*. As soon as PAA begins to adsorb, however, the local concentration drops, and the local conditions at the advancing liquid front shift down the curve in Figure 5.5 (to lower concentrations) resulting in a lower capacity for PAA on the TiO_2 surface. This situation progresses with the net result that the removal of PAA from solution is less and less rapid, and

the effective filtration is less than predicted by F_B for a flat isotherm, producing a larger primitive than would be produced with a flat isotherm (and so the primitive saturation is lower.) This explains the negative deviation of TiO_2 from the straight line predicted for Figure 5.10 b.). One way to account for this oversimplification would be the adoption of an average $\overline{M}$ over the range of concentrations that will be encountered in the pore space (i.e. 0 to the initial PAA concentration, in this case 2.4 vol.%.) Figure 5.11 shows the effect that substituting a simple average value for $\overline{M}$ for TiO_2 of 0.28 (taken directly off the plot in Figure 5.5) has on the plot of saturation vs. filtration factor. A more sophisticated average will of course be necessary for systems where the isotherm shape is more complex. Another factor that could affect the shape of this curve is differing adsorption kinetics, for which Eqn. 5.10 would not account. A higher energy barrier for adsorption in one system would in turn result in slower adsorption,[70] as would the presence of other adsorbed species. The effects of kinetics would not be seen within a given ceramic system (e.g. Al_2O_3) because the same scaling factor would affect all results, but they would affect comparisons between systems. The final distribution of liquid in the pore space may also vary somewhat from system to system due to variations in particle size distribution, pore size distribution, particle morphology, etc.

5.3.4 Effect of Adsorption on Primitive Width

Evaluating the effects of adsorption on primitive width is slightly more complex than for cross sectional area. This is due in part because the primitive width is also affected strongly by the spreading and infiltration behavior, as illustrated in Chapter 4; varying the particle size to affect changes in surface area also changes the pore size, resulting in changes in the ultimate spread width of the printed liquid. In addition, the two effects act against each other, i.e. the small particle size desired to maximize the effects of adsorption is in conflict with the large particle size required to minimize spreading of the liquid. The effects of adsorption on width can not be simply extracted from the cross section dependence either, which is clear upon examination of the way primitive width and thickness vary with surface adsorption. The primitive thickness approaches some finite value as the effects of adsorption are diminished, controlled essentially by the equilibrium distribution of liquid in the pore

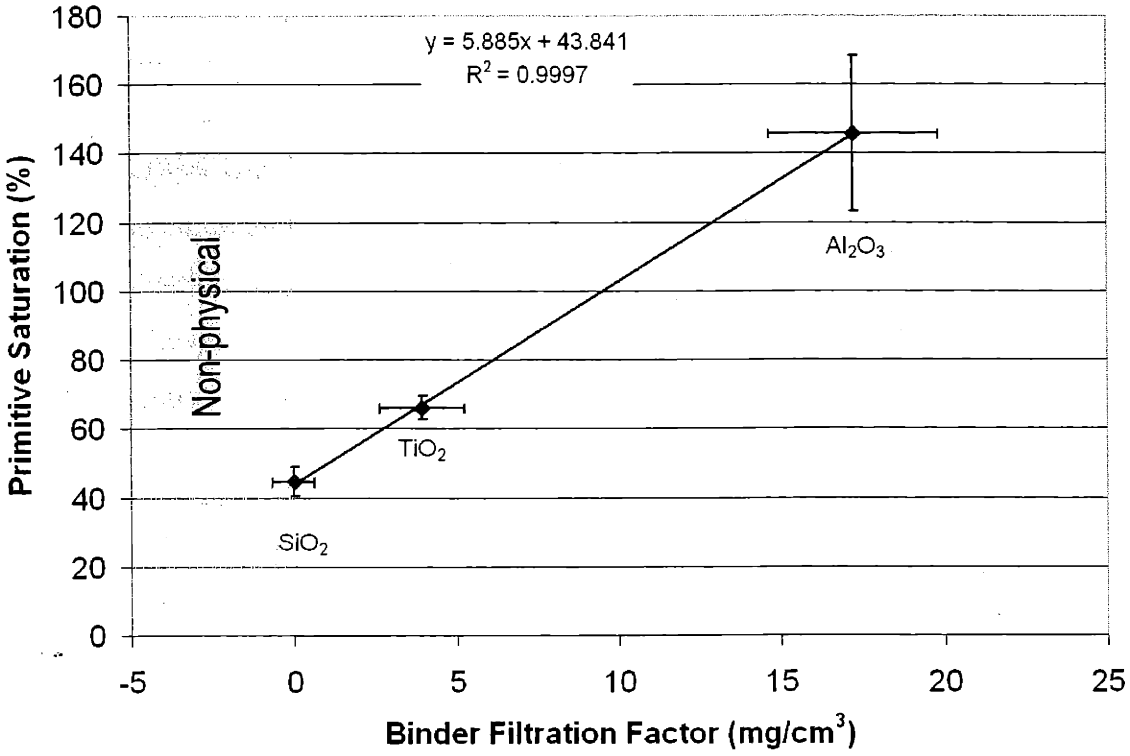

Figure 5.11: Plot of primitive saturation versus binder filtration factor F_B showing the effect of using an average $\overline{M}$ for TiO_2 rather than the value at the initial solution concentration (2.4 vol.% PAA) in order to account for a non-flat isotherm.

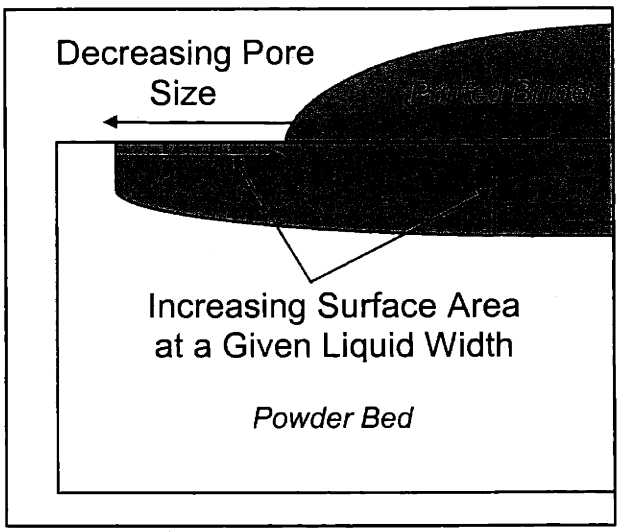

Figure 5.12: Schematic showing the competitive effects of spreading and adsorption on primitive width as the particle size, and thus pore size and surface area, are changed.

space after infiltration. However, as the adsorption effects become strong (e.g. in the limit of infinite surface area), the primitive thickness, and thus the cross sectional area, approach zero. The primitive width on the other hand will go from some finite size affected by both spreading and liquid distribution in the limit of zero adsorption, to being equivalent to the maximum spread width of the liquid in the limit of infinite adsorption (e.g. at infinite surface area, where the polymer will be completely adsorbed upon contact with the powder, producing an infinitely thin layer of finite width.) The competing effects are illustrated schematically in Figure 5.12.

One means of quantifying the effects of adsorption on primitive width separate from spreading is by examining how much wider the primitive is than the ultimate spread width of the liquid as a function of surface area. Experimental data for 2.4 vol.% PAA binder solutions on Al_2O_3 are shown in Figure 5.13 for both standard CJ-printed line primitives and the DoD printed drop primitives from Chapter 4. The data for both DoD drop primitives and CJ line primitives are comparable, indicating that the behavior is consistent over a wide range of printing conditions. The effect of surface area therefore will henceforth be assumed to be approximately independent of print style/liquid volume in developing a functional form for the effect of surface area on primitive width.

In order to develop a functional form relating the fractional increase in width over the liquid width, it is helpful to consider the behavior at the extremes of high and low surface area. As the surface area of the powder gets very small, the effects of adsorption will become negligible. The primitive size will essentially approach a constant value given by the equilibrium distribution of the printed liquid in the pore space. At the other extreme (i.e. very high surface area), the polymer molecules are removed from solution very quickly, and are completely removed at a distance much shorter than the equilibrium liquid infiltration distance. The primitive size is essentially unaffected by the final distribution of liquid in the pore space, and doubling the surface area will cut the primitive size in half (i.e. in the high surface area regime, the relation between fractional increase in size and 1/surface area will be ~ linear.) In the limit as the specific surface area goes to ∞, the increase in width over the liquid width should go to zero. One functional form that displays the same qualitative behavior is that typically used to describe the Langmuir isotherm:

$$y = y_{max} \frac{kx}{1+kx} \qquad \text{Eqn. 5.11}$$

y_{max} is the upper limit on y that is approached as x goes to infinity, and k determines how strong the dependence on x is. To fit the data in Figure 5.13 to a curve of the type given by Eqn. 5.11, the fractional increase in size is the dependent variable, with $1/\overline{S}$ [1/(specific surface area)] as the independent variable. Figure 5.14 contains the results of such a curve fit for the data in Figure 5.13. While not a perfect fit, it does provide a means for predicting the effect of surface area on primitive width with reasonable accuracy over the range of surface areas under examination.

5.3.5 Combined Effects of Spreading and Adsorption

Functional forms for the ultimate spread diameter of DoD droplets (Figure 4.13) and for the effect of surface area on primitive drop diameter (Figure 5.14) have now been found for the PAA-Al_2O_3 system, and so a combined model predicting the ultimate primitive diameter can be developed.

The curve fit in Figure 5.14 can be recast in terms of particle size using the following geometric relationship:

$$d_S = \frac{6}{\overline{S}\rho} \qquad \text{Eqn. 5.12}$$

where:

d_S = equivalent spherical particle diameter calculated from the specific surface area

ρ = density of the ceramic particle

Eqn. 5.12 is only strictly true for monosize spherical particles, and the d_S values calculated tend to underestimate the mean particle size for the Al_2O_3 powders used in these experiments. A simple linear relationship however was found to exist between the equivalent particle diameter d_S and the experimentally measured mean particle diameter. The resulting primitive-liquid width ratio curve recast in terms of particle diameter is shown in Figure 5.15, along with the ultimate spread diameter curve from Figure 4.13. This plot highlights the opposing effects of spreading and surface adsorption with varying particle size. Figure 5.16

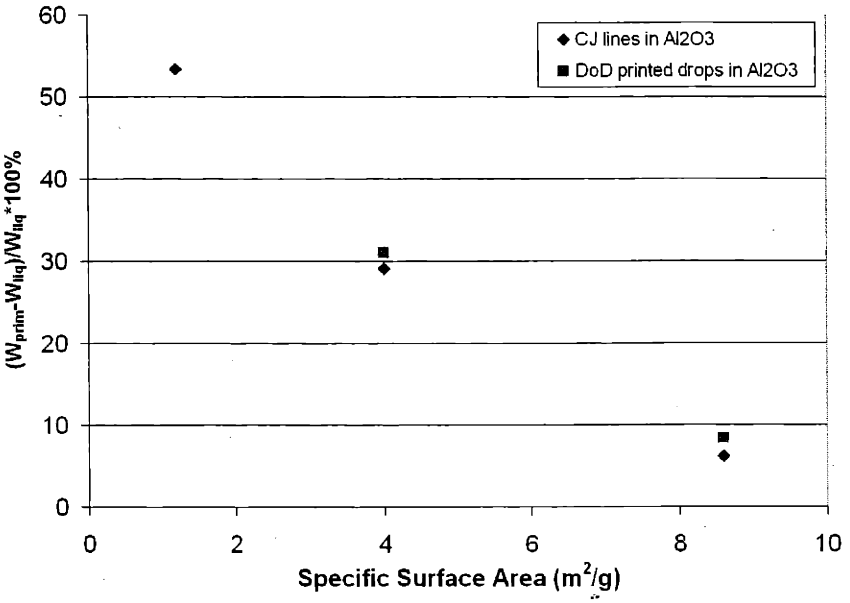

Figure 5.13: Plot relating the extent to which the CJ primitive line width (or DoD primitive drop diameter) is larger than the ultimate liquid spreading width (or diameter) as a function of powder surface area in Al_2O_3 powder beds.

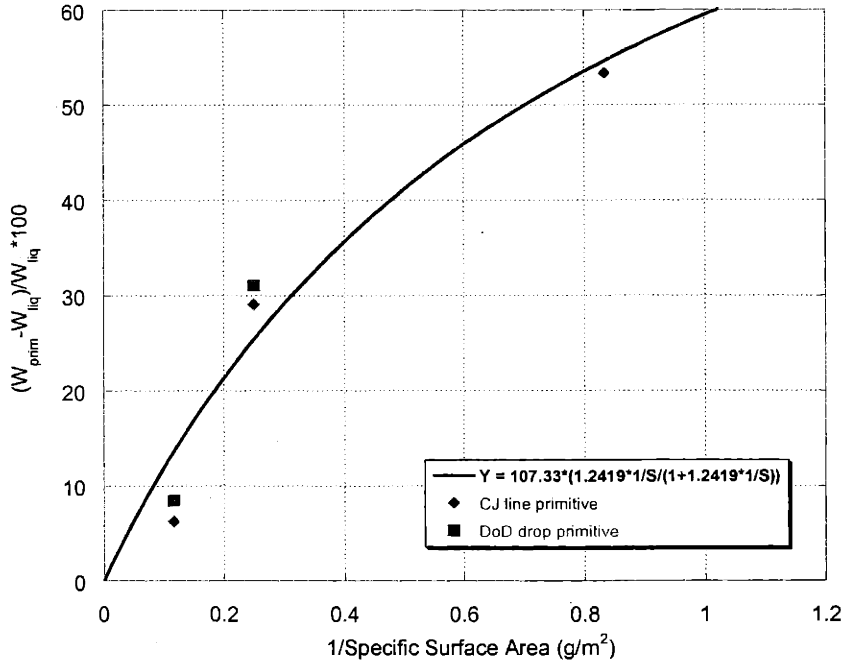

Figure 5.14: Percent difference between primitive and liquid width from Figure 5.13 versus the inverse of the specific surface area, with the curve fit (black curve) as described in the text.

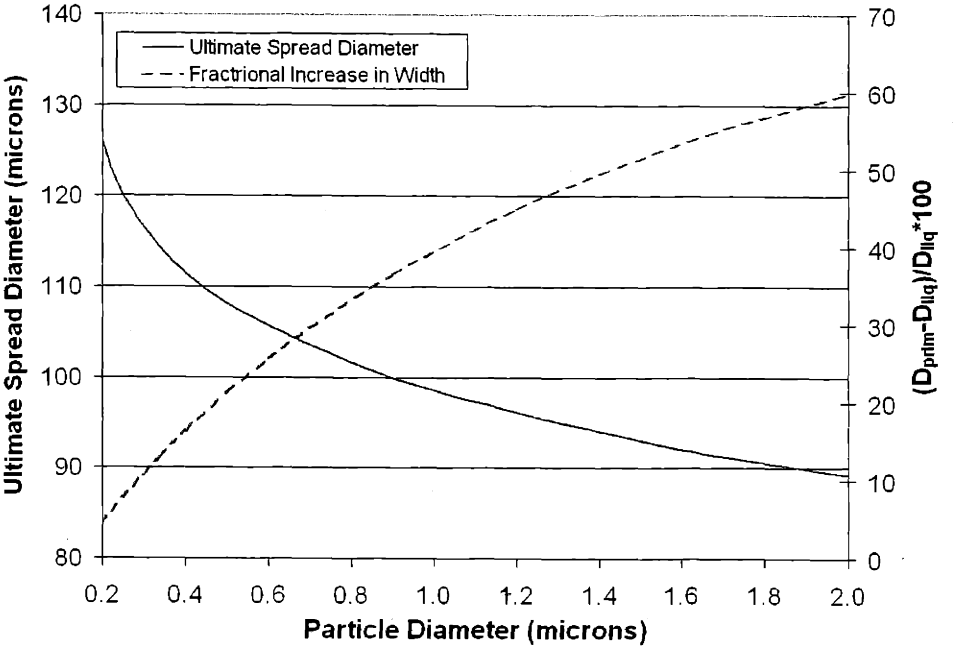

Figure 5.15: DoD droplet ultimate spread diameter and percent difference between the primitive and liquid diameter as a function of particle size showing the opposing effects.

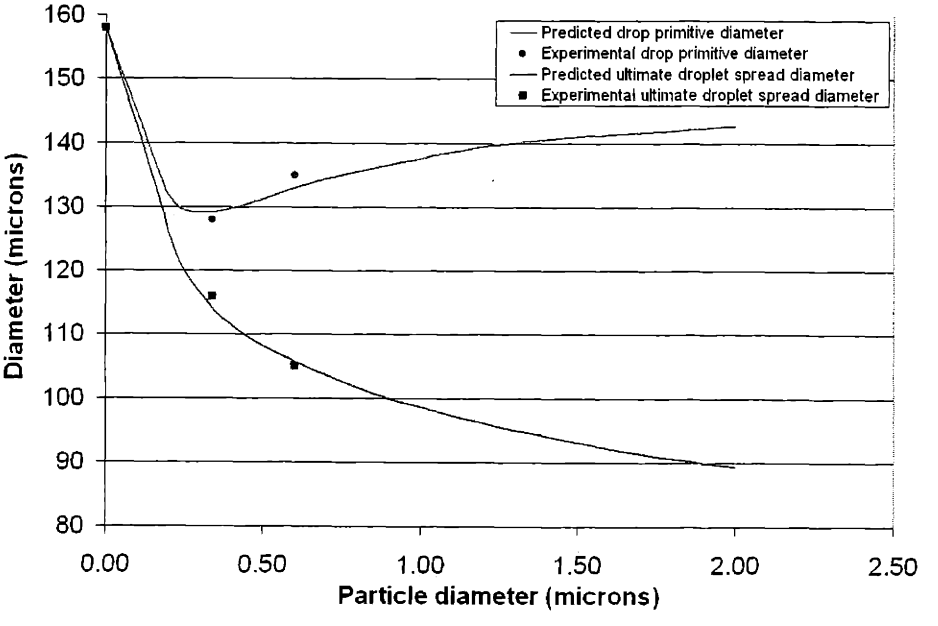

Figure 5.16: Predicted DoD primitive diameter (red curve) from the combined effects of spreading (blue curve) and adsorption (not shown); experimental points are also shown for comparison to theory.

in turn shows the predicted drop primitive diameter from the combined effects of spreading and adsorption as a function of particle size (the spreading theoretical curve and data are also included for comparison.) The two opposing factors result in the existence of a minimum in primitive size at some intermediate particle size. The experimental data for retrieved single drop primitives are also shown on this plot and agree quite well with the theoretical curve. While only two experimental points are available for comparison, the powder bed property data used to generate the curves are known up to 1.7 μm (SPA-TMXX3). The ultimate liquid spread diameter and primitive diameter in the non-physical limit of a particle diameter of 0 are assumed to be equal to the equilibrium spread diameter given by the drop volume and contact angle; this is reasonable because a.) infinitely small particles imply infinitely small pores, so the infiltration time will be infinite, and b.) infinitely small particles imply infinite surface area, so the primitive diameter is expected to simply be equal to the diameter of the spread liquid.

The existence of the minimum in Figure 5.16 illustrates that both spreading and adsorption must be considered when selecting the conditions that will produce the finest possible primitive width. Binder solutions with higher polymer concentration will shift the minimum to lower particle size (essentially diminishing the effects of adsorption at a given surface area/particle size.) Decreasing affinity of the polymer for the ceramic, in addition to resulting in a general increase in primitive width, will have a similar effect, shifting the minimum to lower particle sizes (more surface area is required to achieve a given size.) At zero surface affinity, however, the effects of adsorption are eliminated, so no minimum in primitive diameter is expected (it will be controlled entirely by spreading, and so the largest practical particle size should be used.) This also suggests that with decreasing surface affinity the primitive diameter curve will change shape, and at some point will go through an inflection point beyond which no minimum with particle size will be realized.

Figure 5.17 contains experimental primitive width and ultimate spread width data for CJ printed lines, as well as the DoD data of Figure 5.16 for comparison. The primitive line width data clearly exhibit a minimum with increasing particle size, however the optimum particle size is larger than for DoD-printed droplets. Thus while the same general behavior is expected for both regimes, the optimum particle size will depend on print style.

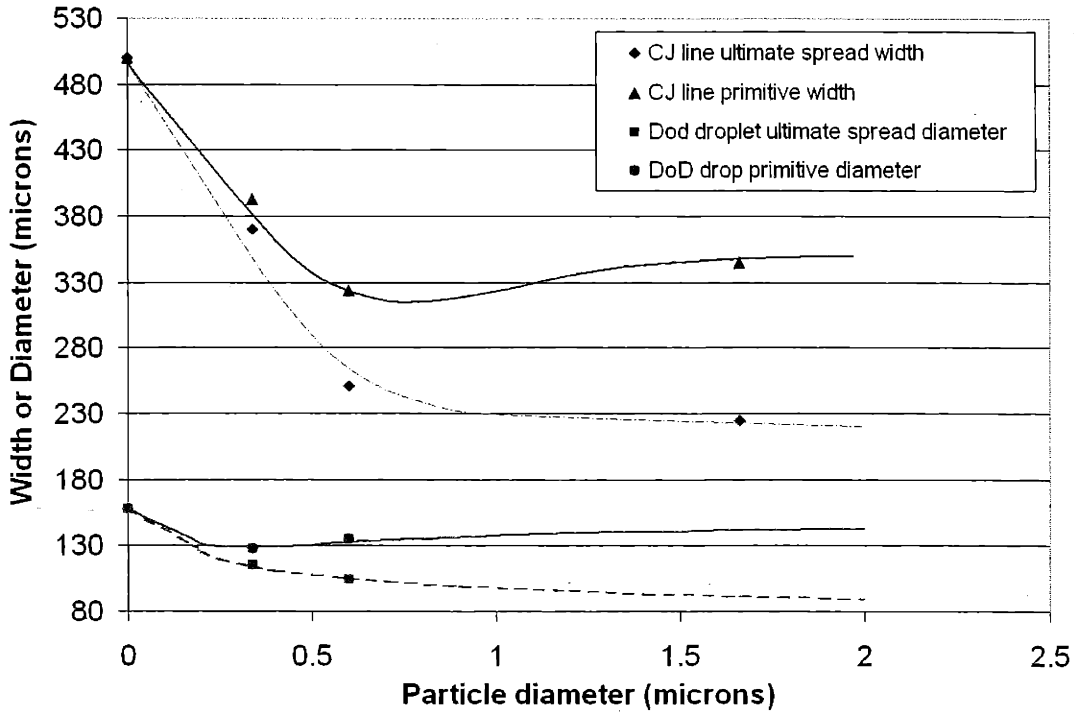

Figure 5.17: Experimental primitive width (diameter) and ultimate spread width (diameter) for CJ line primitives (DoD drop primitives); the curves through the experimental DoD data are the theoretical curves from Figure 5.16, while the curves through the CJ data are for visualization purposes only.

This chapter has evaluated the role of polymer adsorption in the evolution of the primitive structure. A theory based on adsorptive filtration was developed and confirmed experimentally. A higher capacity for PAA adsorption on the surface of the ceramic as determined via adsorption isotherms results in a smaller primitive cross sectional area, and the primitive cross section decreases with increasing specific surface area in the ceramic for the high-affinity Al_2O_3-PAA system. From the results above, it is also clear that primitive width is a complex function of surface adsorption phenomena combined with the spreading phenomena outlined in Chapter 4. Chapter 6 examines the overall implications of this research, and gives suggestions for future directions based on this work.

Chapter 6: Conclusions

6.1 Summary of Results

The primitive size and shape in the slurry-based Three Dimensional Printing process (S-3DP^{TM}) for ceramics is controlled primarily by two factors: the spreading of the printed binder solution on the surface of the powder bed before infiltration of said liquid is complete, and an adsorptive filtering (or lack thereof) of the polymeric binder during infiltration. Impact of the printed binder solution with the surface of the powder bed was not found to play a role in determining primitive size under the operating conditions typically encountered in S-3DP^{TM} of ceramics. The ultimate width of the printed liquid binder line results from simple wetting phenomena on the rough powder bed surface. The time scales of spreading and infiltration were shown to be comparable, and so the exact extent of the liquid spreading is determined primarily by a balance between spreading time and infiltration time. It was shown that by changing the infiltration time of the binder solution (via the effect of pore size on permeability of the powder bed), the extent of spreading of the printed binder line could be modified. Longer infiltration times translate to more time available for the liquid to spread, and as such a wider printed line results.

Adsorption of the polymeric binder system (polyacrylic acid, PAA, MW 60000) onto the surface of certain ceramic systems was shown to effectively filter the polymer from the infiltrating binder solution. This has the result of limiting the primitive size (cross sectional area) by diluting the binder solution as it passes deeper into the powder bed. The adsorption of the PAA binder was characterized on various ceramics (with differing surface chemistries), and the primitive cross sectional area was shown to correlate well with the affinity of PAA for the surface. The higher the affinity of PAA for the surface, the smaller the resulting primitive cross section. The primitive cross section was also shown to vary with surface area of the powder in the Al_2O_3 ceramic system, for which PAA has a high affinity. This behavior is of course expected if filtration of the binder by the ceramic surface is limiting primitive size. The resulting primitive saturation ratio exhibited the expected linear dependence on surface area.

6.2 *Implications for the Future*

The preceding chapters have outlined various factors that affect primitive size and shape in ceramics S-3DP™. The next few sections discuss the implications of this work and provide suggestions for future directions of the research.

6.2.1 Minimizing Feature Size (Primitive Width)

The primitive size and shape under the current standard practice is a complex function of wetting and spreading, infiltration, and polymer adsorption. The optimal powder characteristics to minimize spreading of the printed binder solution on the powder bed surface are in general contrary to the characteristics desirable to maximize the beneficial adsorption effects. The optimal powder will represent a tradeoff between these two factors, and will also depend on the print style.

The combination of binder system and ceramic should be chosen so as to maximize the positive effects of adsorption in limiting primitive size. The smallest primitives to date occur in the PAA-Al_2O_3 system because the charges of the ceramic surface and the polymer are vastly different. A similar situation could be induced e.g. in SiO_2 if a basic polymeric binder system with a positive charge in solution were employed. Thus in high pH binder solutions the SiO_2 surface would attain a large negative charge, attracting the binder molecules in analog to the PAA-Al_2O_3 system. The chief obstacle to this approach is the identification of new polymeric binder systems that satisfy all of the requirements of the S-3DP™ process (ideally aqueous, relatively non-toxic, cross-linkable to make them insoluble during part retrieval, cross linkable at low temperatures for thermally cross linked systems to minimize degradation of the polyethylene glycol additive, relatively high strength, appropriate wetting properties[44], etc..)

DoD printing represents the best approach for producing the maximum resolution in S-3DP™. The smaller volumes of binder solution involved will inherently result in smaller primitives regardless of infiltration and adsorption effects, and in addition will allow the effects of spreading to be kept at a minimum: a smaller quantity of liquid will infiltrate faster, not only because of its smaller volume, but also because the infiltration rate decreases with increasing infiltrated depth, and a smaller dose will naturally have a smaller equilibrium

spread width. The natural ultimate extension of this approach is to allow complete infiltration of individual printed droplets before the next droplet is deposited, as was introduced in Chapter 4. This results in the minimum possible volume of liquid spreading at any given time, and the width of the individual droplets would then naturally be unaffected by the presence of any pre-existing liquid already on the surface (because there would be none.) The liquid extension is therefore limited to that of the single isolated droplets, and the effective ultimate spread width of the line becomes of the order of the spreading diameter of a single droplet (rather than of many overlapping droplets, i.e. a line.) This approach can no longer depend on the coalescence of the droplets into a bead to produce a smooth-edged primitive, so droplet overlap must be sufficient to prevent "scalloping" of the edge. It also unfortunately has the disadvantage of requiring relatively slow droplet generation rates, increasing printing times. For low volume and/or small components, however, this may well be a non-issue. The low droplet generation rates required to allow complete infiltration are outside the range of CJ printing, and thus necessitate the use of DoD printing.

Another attractive approach to minimizing the spreading contribution to primitive size is to engineer the binder solution-ceramic systems to produce a high apparent contact angle between the solution and the surface of the powder bed. The current contact angle is quite low (~10°), so great improvements in ultimate spread diameter are possible, as discussed in Chapter 4. One possibility is the use of a polymer coating or adsorbed layer to minimize the wettability. This would of course almost certainly eliminate the positive effects of adsorption, however the greatly decreased spread width could outweigh this negative aspect if the contact angle were large enough. The only stipulation is that the contact angle be low enough to allow infiltration of the binder solution, and that the infiltration time not be impractically long.

The best possible combination to produce the minimum primitive width should therefore encompass the following criteria: The binder solution should have a relatively large contact angle on the powder bed surface to minimize spreading. The polymeric binder should have a high affinity for the ceramic surface at the binder solution pH to maximize the positive effects of adsorption. DoD printing should be employed using the smallest possible droplet size, and the droplet generation rate should be chosen so as to allow complete infiltration of a

deposited droplet prior to the impact of the subsequent droplet. Finally, the particle size should be chosen to obtain the best tradeoff between spreading and infiltration. Other areas to explore include textured or nano-porous powders to maximize the surface area for a given particle size, and the factors affecting the equilibrium distribution of the printed liquid in the pore space (which could prove particularly useful in systems where no suitable adsorbing polymeric binder can be found.)

6.2.2 Minimizing Primitive Size Variability

A large degree of variability in the primitive size (width) has been observed throughout the course of this research. This results in part within a given system from the fact that S-3DP™ currently operates in a regime where primitive width is controlled by a fine balance between spreading and infiltration, and in part due to variations in adsorption between systems. The observed variability in primitive width/shape makes the formation of components with accurate dimensions difficult (if the primitive size varies from day to day, so will the part dimensions.) Eliminating this variability should be a second focus of future work in this area.

6.2.2.1 Minimizing Spreading Variations

Working in a controlled environment where temperature and humidity variations can be eliminated should improve reproducibility of the primitive width; this however is only an option for applications where this is economically feasible. Another possible solution would be to shift the operating parameters to a regime where only one process is active. An extremely rapid infiltration rate could "freeze in" the width that results from the impact-related splatting of the liquid, removing liquid spreading from the equation. This has the advantage of producing the narrowest possible ultimate spread width. It will however in general be difficult or impossible to implement, because the pore size can only be made so big via particle size before sintering times become impractically long. Decreasing the amount of liquid deposited per unit time offers an attractive alternative, e.g. via DoD printing. Assuming that the error in the spread width scales approximately as the total width, the size

error could in theory be brought within tolerances via binder dose even if spreading remains the dominant factor.

The opposite approach could also be taken, i.e. infiltration could be slowed down so much that complete spreading takes place. This would of course mean that the widest possible spread width would always be attained (not necessarily the most attractive proposition if this value is large.) Extremely fine particle size powders are one means to this end, but only if they are available in the system of interest (often not the case), and in very fine powders, cracking of the printed slurry layers can become an issue.[44] Another option is to change the wetting properties of the powder, e.g. by a polymeric coating or adsorbed layer on the powders. This could be done in the ceramic slurry or perhaps as a separate printing step prior to printing of the binder solution. Making the powders less wettable by the binder solution would slow infiltration while simultaneously decreasing the equilibrium spreading width, which could be the best of both worlds. Care must be exercised, however, because the added polymer may affect slurry stability and the green density of the powder bed, and represents additional organic content that must be removed during the burnout stage. However this coupled with the smallest possible droplet size and allowing complete infiltration between droplet impacts may provide a tenable solution for producing a primitive width in ceramics S-3DP™ that is both small and reproducible.

6.2.2.2 Variations in PAA Adsorption

A complication that arises from the adsorption results of Chapter 5 is that the primitive size varies from one system to the next, and must therefore be characterized in detail each time a new ceramic system is adopted. The resolution and printing parameters of the S-3DP™ process thus become system dependent, which could be problematic when multiple materials exist within a given build. Coating of all powders with a given polymer to make them non-adsorbing (or to make the exchange on the surface of the coating polymer for PAA too slow to be a factor) would make S-3DP™ resolution more system independent. This of course assumes that the spread width were also made system independent, which could be achieved in part by the same polymer coating employed to bar adsorption of the PAA (as mentioned above), and also neglects any green density or pore-size effects. This would

essentially bring the primitive cross section in all systems to its maximum value, eliminating any positive effects of adsorption on limiting the feature size (as is the case in the PAA-Al_2O_3 system.)

The possibility of a polymer blend in the binder solution containing both adsorbing and non-adsorbing polymer systems (i.e. oppositely charged polymers) may represent another path to a more "universal" S-3DP^{TM} binder system; only one species would be attracted to a given ceramic surface, and as such the other (non-adsorbing) species would determine primitive size. This could allow the use of a single binder "cocktail" with a range of ceramic surfaces, with similar primitive cross-sections across systems. The polymer systems must of course not react with one another, and enough of each system must be present to produce a cohesive structure when the other system has completely adsorbed.

6.3 New Challenges

The project with TDK USA Corp. has presented a number of new and particularly challenging applications for the S-3DP^{TM} process. The area of ceramic electronics requires particularly high shape accuracy, and the ever-present push to miniaturization places high demands on the shape-forming process. One application already presented in this thesis is the microwave frequency band pass filter. While the results obtained so far with S-3DP^{TM} are impressive, they still fall short of the level of resolution and accuracy required. The integration of DoD printing in the MIT-TDK S-3DP^{TM} machine is the first step toward achieving the feature size goals because of the smaller binder dose that can be achieved with this style of printing as compared to CJ. The variability observed in primitive size may still need to be addressed if the ultimate in dimensional accuracy is to be achieved. Other applications may push the limits of even what DoD is capable of. One such example is the plasma display panel, or PDP. Such panels are found for example in large HDTV sets. The structure of interest in 3DP^{TM} consists of long parallel barrier ribs on a substrate. The space between the ribs contains the red, green, and blue phosphor materials as well as the noble gas/gas blend in which the plasma is formed, and the ribs serve to separate and isolate the three color regions. A section of this structure is shown schematically in Figure 6.1. This application requires long straight walls ~ 100 μm tall by ~ 50 μm wide or smaller, which may

require the adoption of new printing methods. Initial results with a modification of the CJ process have been promising (Figure 6.2), but much work remains. It is the belief of the author that applying the principles related to solution spreading and infiltration as well as polymer adsorption during infiltration will play a key role in achieving the stringent requirements of these applications both in terms of resolution and tolerances (repeatability of the primitive size.)

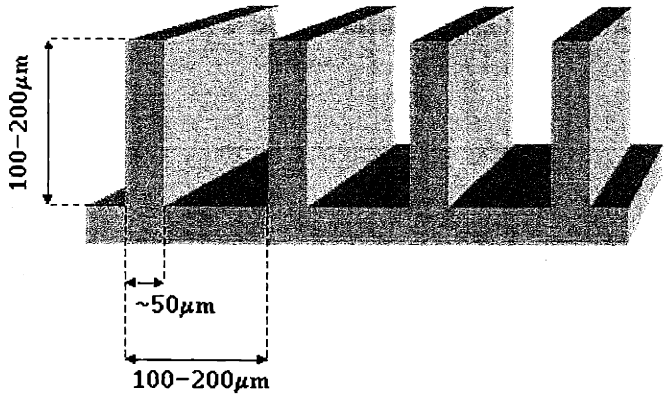

Figure 6.1: Schematic of s section of the barrier rib structure that contains the phosphors and gas in a plasma display panel.[76]

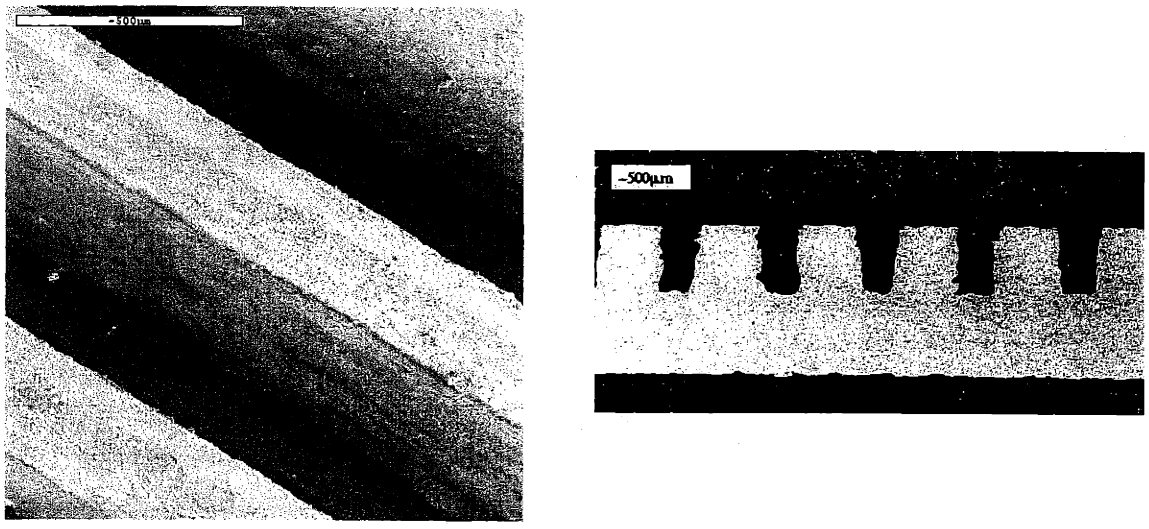

a.) **b.)**

Figure 6.2: SEM's of the initial prototype S-3DP™ Al_2O_3 barrier ribs for plasma display devices (ribs are shown in the green state), a.) in an oblique view, and b.) in cross section perpendicular to the ribs.[76]

Appendix I

Forward Finite Difference Heat Transfer Code (C++)

```
/*  This program performs a forward finite difference heat transfer*/
/*  simulation on a 300 x 30 micron liquid drop cooling in contact */
/*  with a 1440 x 600 micron alumina substrate, with the liquid */
/*  bounded on the sides by convection.  The alumina-air surface is */
/*  bounded by convection, and the other surfaces are defined as the */
/*  initial temp.  */


#include "math.h"
#include "stdio.h"

int init_T_liq(float (*T_array)[10], float init_value, int xsize, int
ysize)

{
      int i,j;
      printf("\nbeginning init_T_liq\n");
      for (i=0;i<xsize;i++) {
//          printf("\nIn outer init_T loop\n");
          for(j=0;j<ysize;j++) {
//              printf("\nIn inner init_T loop before assignment\n");
              T_array[i][j]=init_value;
//              printf("\nIn inner init_T loop after assignment\n");
              }
      }
      printf("\nEnding init_T_liq\n");
      return 0;
};


int init_T_al2o3(float (*T_array)[200], float init_value, int xsize, int
ysize)

{
      int i,j;
      printf("\nbeginning init_T_al2o3\n");
      for (i=0;i<xsize;i++) {
//          printf("\nIn outer init_T loop\n");
          for(j=0;j<ysize;j++) {
//              printf("\nIn inner init_T loop before assignment\n");
              T_array[i][j]=init_value;
//              printf("\nIn inner init_T loop after assignment\n");
              }
```

```
        }
        printf("\nEnding init_T_al2o3\n");
        return 0;
};


int runsim(float (*T0_liq)[10], float (*T1_liq)[10], float
(*T0_al2o3)[200], float (*T1_al2o3)[200], float M_liq, float N_liq, float
M_al2o3, float N_al2o3, long int iter, float T_air)

{
        long int step;
        int i,j;

        for(step=1; step<=iter; step++) {

          /*  liquid corners  */

          T1_liq[0][0] = 2./M_liq*(T0_liq[1][0] + T0_liq[0][1]) +
4.*N_liq/M_liq*T_air + (1. - 4./M_liq - 4.*N_liq/M_liq)*T0_liq[0][0];
          T1_liq[79][0] = 2./M_liq*(T0_liq[78][0] + T0_liq[79][1]) +
4.*N_liq/M_liq*T_air + (1. - 4./M_liq - 4.*N_liq/M_liq)*T0_liq[79][0];

          /*  liq vertical edge at interface with al2o3  */

          T1_liq[0][9] = 1./M_liq*(T0_liq[0][8] + T0_al2o3[200][0] +
2.*T0_liq[1][9]) + 2.*N_liq/M_liq*T_air + (1. - 2.*N_liq/M_liq -
4./M_liq)*T0_liq[0][9];
          T1_liq[79][9] = 1./M_liq*(T0_liq[79][8] + T0_al2o3[279][0] +
2.*T0_liq[78][9]) + 2.*N_liq/M_liq*T_air + (1. - 2.*N_liq/M_liq -
4./M_liq)*T0_liq[79][9];


          /*  liq. interface not at edge, then liq horiz edge, then liq
interior  */

          for(i=1; i<=78; i++)  {

              T1_liq[i][9] = 1./M_liq*(T0_liq[i-1][9] + T0_liq[i+1][9] +
T0_liq[i][8] + T0_al2o3[i+200][0]) +(1.-(4./M_liq))*T0_liq[i][9];
              T1_liq[i][0] = 1./M_liq*(T0_liq[i-1][0] + T0_liq[i+1][0] +
2.*T0_liq[i][1]) + 2.*N_liq/M_liq*T_air + (1 - 2.*N_liq/M_liq -
4./M_liq)*T0_liq[i][0];

              for(j=1; j<=8; j++)  {

                T1_liq[i][j] = 1./M_liq*(T0_liq[i+1][j] + T0_liq[i-1][j] +
T0_liq[i][j+1] + T0_liq[i][j-1]) + (1. - 4./M_liq)*T0_liq[i][j];

              }

          }

          /*  liq-air vertical surfaces, not incl. al2o3 interface  */
```

```
        for(j=1; j<=8; j++)  {

            T1_liq[0][j] = 1./M_liq*(T0_liq[0][j-1] + T0_liq[0][j+1]
+2.*T0_liq[1][j]) + 2.*N_liq/M_liq*T_air + (1. - 2.*N_liq/M_liq -
4./M_liq)*T0_liq[0][j];
            T1_liq[79][j] = 1./M_liq*(T0_liq[79][j-1] + T0_liq[79][j+1] +
2.*T0_liq[78][j]) + 2.*N_liq/M_liq*T_air+(1.-2.*N_liq/M_liq-
4./M_liq)*T0_liq[79][j];

        }

        /*  al2o3 horizontal air surface, two parts  */

        for(i=1; i<=199; i++)  {

            int ii;
            ii = i + 279;

            T1_al2o3[i][0]=1./M_al2o3*(T0_al2o3[i-
1][0]+T0_al2o3[i+1][0]+2.*T0_al2o3[i][1])+2.*N_al2o3/M_al2o3*T_air+(1.-
2.*N_al2o3/M_al2o3-4./M_al2o3)*T0_al2o3[i][0];
            T1_al2o3[ii][0]=1./M_al2o3*(T0_al2o3[ii-
1][0]+T0_al2o3[ii+1][0]+2.*T0_al2o3[ii][1])+2.*N_al2o3/M_al2o3*T_air+(1.-
2.*N_al2o3/M_al2o3-4./M_al2o3)*T0_al2o3[ii][0];

        }

        /*  al2o3 interface qith liq  */

        for(i=200; i<=279; i++)  {

            T1_al2o3[i][0] = 1./M_al2o3*(T0_al2o3[i-1][0] +
T0_al2o3[i+1][0] + T0_al2o3[i][1] + T0_liq[i-200][9]) + (1. -
4./M_al2o3)*T0_al2o3[i][0];

        }

        /*  al2o3 interior  */

        for(i=1; i<=478; i++)  {

            for(j=1; j<=198; j++)  {

              T1_al2o3[i][j] = 1./M_al2o3*(T0_al2o3[i+1][j] + T0_al2o3[i-
1][j] + T0_al2o3[i][j+1] + T0_al2o3[i][j-1]) + (1. -
4./M_al2o3)*T0_al2o3[i][j];

            }

        }
      /*  place the t=1 arrays into the t=0 positions for the next
iteration  */
          for(i=0;i<80;i++)  {
              for(j=0;j<10;j++)
                  T0_liq[i][j] = T1_liq[i][j];
```

```
        }

        for(i=0;i<480;i++)  {
            for(j=0;j<200;j++)
                T0_al2o3[i][j] = T1_al2o3[i][j];
        }

    }
    return 0;
};


void main()

{
    float liq_T_t1[80][10];          /*liquid temp array at current time,
t1*/
    float liq_T_t0[80][10];          /*liquid temp array at prev time, t*/
    float al2o3_T_t1[480][200];      /*al2o3 temp at t1*/
    float al2o3_T_t0[480][200];      /*al2o3 temp at t*/
    float T_0_liq;                       /*initial liquid temp,  make user
input*/
    float T_0_al2o3;                     /*initial al2o3 temp, make user
input*/
    float T_air;                         /*air temp*/
    float dt;                              /*time step*/
    float dz;                          /*distance step*/
    float cp_liq, k_liq, rho_liq, alpha_liq, h_liq;
    float cp_al2o3, k_al2o3, rho_al2o3, alpha_al2o3, h_al2o3;
    float M_liq, N_liq, M_al2o3, N_al2o3;
    float time;                          /*total simul. time*/
    int i,j;
    long int iter;                         /*number of iterations*/
/*    int init_T(float**, float, int, int);                      /*function
to init temps*/
/*    int runsim(float**, float**, float**, float**, float, float, float,
float, long int, float);     /*function that actually runs simul*/
    FILE *al2o3out;
    FILE *liqout;

/*  Initialize all the material constants  */

    cp_liq = 4.2;                                /*  J/g-K  */
    k_liq = 0.6;                                 /*  W/m-K  */
    rho_liq = 1.0;                                   /*  g/cc   */
    alpha_liq = k_liq/(rho_liq*cp_liq)*pow(100.0,-3);   /*  m^2/s  */
    h_liq = 10.0;                              /*  W/m^2-K */
    T_0_liq = 30.0;                                  /*  C      */
    cp_al2o3 = 0.765;                            /*  J/g-K  */
    k_al2o3 = 36.0;                              /*  W/m-K  */
    rho_al2o3 = 3.96;                            /*  g/cc   */
    alpha_al2o3 = k_al2o3/(rho_al2o3*cp_al2o3)*pow(100.0,-3);
    h_al2o3 = 10.0;                              /*  W/m^2-K */
    T_0_al2o3 = 20.0;
    dz = 3.0*pow10(-6.0);                        /*  m      */
```

```
    dt = 1.0*pow10(-7.0);                                   /*  s       */
    M_liq = dz*dz/(alpha_liq*dt);
    N_liq = h_liq*dz/k_liq;
    M_al2o3 = dz*dz/(alpha_al2o3*dt);
    N_al2o3 = h_al2o3*dz/k_al2o3;
    T_air = 20.0;

/*    These values NEED to be user input  */

    printf("Please enter the total simulation time in micro-seconds:");
    scanf("%f",&time);
    time = time/1000000.;
    iter = (long int) (time/dt);

/* ------------------------------------ */

/*  Call the function to initialize the arrays  */

    printf("\nabout to make first function call to init_T\n");

    init_T_liq(liq_T_t0,T_0_liq,80,10);
    init_T_liq(liq_T_t1,T_0_liq,80,10);
    init_T_al2o3(al2o3_T_t0,T_0_al2o3,480,200);
    init_T_al2o3(al2o3_T_t1,T_0_al2o3,480,200);


/*  call the function to do the actual simulation  */

runsim(liq_T_t0,liq_T_t1,al2o3_T_t0,al2o3_T_t1,M_liq,N_liq,M_al2o3,N_al2o3,
iter,T_air);

/*  Write the resulting T-matrices to files  */
    liqout = fopen("liqout.txt","w");
    fprintf(liqout,"Final liquid Temp data for time = %f microseconds
\n\n", time*1000000.);
    fprintf(liqout,"float size: %d\n",sizeof(float));
    for(j=0;j<10;j++) {
        for(i=0;i<80;i++)
            fprintf(liqout, "%f  ",liq_T_t1[i][j]);
        fprintf(liqout,"\n");
    }
    fclose(liqout);
    al2o3out = fopen("al2o3out.txt","w");
    fprintf(al2o3out,"Final Al2O3 Temp data for time = %f microseconds
\n\n", time*1000000.);
    for(j=0;j<200;j++) {
        for(i=0;i<480;i++)
            fprintf(al2o3out, "%f  ",al2o3_T_t1[i][j]);
        fprintf(al2o3out,"\n");
    }
    fclose(al2o3out);

};
```

References

1. McEntire, B. J., "Dry Pressing," Engineered Materials Handbook Volume 4: Ceramics and Glasses, pp. 141-146, 1991.
2. Reed, J., Introduction to the Principles of Ceramic Processing, New York, 1988.
3. Oezkan, N. and B. J. Briscoe, "Characterization of Die-Pressed Green Compacts," *Journal of the European Ceramic Society*, **17**, pp. 697-711, 1997.
4. Carlstroem, E., "Surface and Colloid Chemistry in Ceramics: An Overview," Surfactant Science Series Volume 51: Surface and Colloid Chemistry in Advanced Ceramics Processing, pp. 1-28, 1994.
5. Schilling, C. H. and I. A. Aksay, "Slip Casting," Engineered Materials Handbook Volume 4: Ceramics and Glasses, pp. 153-160, 1991.
6. Persson, M., "Surface and Colloid Chemistry in Ceramic Casting Operations," Surfactant Science Series Volume 51: Surface and Colloid Chemistry in Advanced Ceramics Processing, pp. 279-307, 1994.
7. Lehman, R. L., "Overview of Ceramic Design and Process Engineering," Engineered Materials Handbook Volume 4: Ceramics and Glasses, pp. 29-37, 1991.
8. Rak, S. R., "Advanced Shaping Techniques in Advanced Ceramics," *Ceramic Forum International*, **77 [6]**, pp. 6-16, 2000.
9. Howatt, G. N., R. G. Breckenridge, and J. M. Brownlow, "Fabrication of Thin Ceramic Sheets for Capacitors," *Journal of the American Ceramic Society*, **30 [8]**, pp. 237-242, 1947.
10. Evans, J. R. G., "Injection Moulding of Fine Ceramics," Advanced Ceramic Processing and Technology, v. 1, pp. 215-254, 1990.
11. Cannell, D. and P. Trigg, "Processing of Electronic Ceramics," Advanced Ceramic Processing and Technology, v. 1, pp. 95-121, 1990.
12. Edirisinghe, M. J., and J. R. G. Evans, "Review: Fabrication of Engineering Ceramics by Injection Moulding II: Techniques," *International Journal of High Technology Ceramics*, **2**, pp. 249-278, 1986.
13. Mistler, R. E., "Tape Casting: Past, Present, and Future," *The American Ceramic Society Bulletin*, **77 [10]**, pp. 82-86, 1998.
14. Klocke, F., "Modern Approaches for the Production of Ceramic Components," *Journal of the European Ceramic Society*, **17**, pp. 457-465, 1997.
15. Helsinki University of Technology, http://www.cs.hut.fi/~ado/rp/subsection3_6_1.html, Feb. 2001.
16. Griffith, M. L. and J. W. Halloran, "Freeform Fabrication of Ceramics via Stereolithography," *Journal of the American Ceramic Society*, **79 [10]**, pp. 2601-2698, 1996.
17. Ahmad, L., L. Eckstrand, and J. Pantarotto, "Rapid Prototyping and Solid Freeform Manufacture," *Canadian Ceramics Quarterly*, **66 [2]**, 1997.
18. Sigmund, W. M. et al, "Novel Powder-Processing Methods for Advanced Ceramics," *Journal of the American Ceramic Society*, **83 [7]**, pp. 1557-1574, 2000.
19. Wang, G. and V. D. Krstic, "Rapid Prototyping of Ceramic Components - Review," *Canadian Ceramics*, **67 [3]**, pp. 52-58, 1998.

20. University of Dayton, http://www.udri.udayton.edu/rpdl/Paper_Austin96/figures2.htm, Feb. 2001.
21. Klosterman, D. A. et al, "Direct Fabrication of Ceramics, CMC's by Rapid Prototyping," *The American Ceramic Society Bulletin*, **77 [10]**, pp. 69-74, 1998.
22. Griffin, C., J. Daufenbach and S. McMillin, "Desktop Manufacturing: LOM vs. Pressing," *The American Ceramic Society Bulletin*, **73 [8]**, pp. 109-113, 1994.
23. Klosterman, D. A. et al, "Curved Layer LOM of Ceramics and Composites," *Proceedings of the Solid Freeform Fabrication Symposium*, pp. 671-680, 1998.
24. CAM-LEM Inc., http://www.camlem.com/camlemprocess.html, Feb. 2001.
25. Cawley, J. D. et al, "Computer-Aided Manufacturing of Laminated Engineering Materials," *The American Ceramic Society Bulletin*, **75 [5]**, 1996.
26. Agarwala, M. K., "FDC, Rapid Fabrication of Structural Components," *The American Ceramic Society Bulletin*, **75 [11]**, pp. 60-65, 1996.
27. Rutgers University, http://www.caip.rutgers.edu/sff/acers95/pict12.jpg, Feb. 2001.
28. Griffin, A., "Rapid Prototyping with Engineered Ceramics," *Ceramic Industry*, **147 [4]**, pp. 86-88, 1997.
29. University of Texas, Austin, http://lff.me.utexas.edu/sls.html, Feb. 2001.
30. Bourell, D. L., et al., "Selective Laser Sintering of Metals and Ceramics," *International Journal of Powder Metallurgy*, **28 [4]**, pp. 369-381, 1992.
31. Subramanian, P. K., and H. L. Marcus, "Selective Laser Sintering of Alumina Using Aluminum Binder," *Materials and Manufacturing Processes*, **10 [4]**, pp. 689-706, 1995.
32. Serdy, J., *personal communication*.
33. Wu, B., Microstructural Control During Three Dimensional Printing of Polymeric Medical Devices, Ph.D. Dissertation, Department of Materials Science and Engineering, Massachusetts Institute of Technology, 1998.
34. Sachs, E., M. Cima, et al., "Three Dimensional Printing: Rapid Tooling and Prototypes Directly from a CAD Model," *Journal of Engineering for Industry (Transactions of the ASME)*, **114 [4]**, pp. 481-488, 1992.
35. Grau, J., M. Cima, and E. Sachs, "Fabricating Alumina Moulds for Slip Casting with 3-D Printing," *Ceramic Industry*, **146 [7]**, pp. 22-27, 1996.
36. Sachs, E., et al., "CAD-Casting: Direct Fabrication of Ceramic Shells and Cores by Three Dimensional Printing," *Manufacturing Review*, **5 [2]**, pp. 117-126, 1992.
37. Yoo, J., Fabrication and Microstructural Control of Advanced Ceramic Components by Three Dimensional Printing, Ph.D. Dissertation, Department of Materials Science and Engineering, Massachusetts Institute of Technology, 1996.
38. Khanuja, S., Origin and Control of Anisotropy in Three Dimensional Printing of Structural Ceramics, Ph.D. Dissertation, Department of Materials Science and Engineering, Massachusetts Institute of Technology, 1996.
39. Uhland, S., Fabrication of Advanced Ceramic Components Using Slurry-Based Three Dimensional Printing, Ph.D. Dissertation, Department of Materials Science and Engineering, Massachusetts Institute of Technology, 2000.
40. Chiang, Y., D. Birnie and W. Kingery, Physical Ceramics, v. 2, New York, 1997.
41. Kingery, W., H. Bowen and D. Uhlmann, Introduction to Ceramics, v. 2, New York, 1976.

42. Herring, C., "Effect of Change of Scale on Sintering Phenomena," *Journal of Applied Physics*, **21 [301]**, 1950.
43. Boschi, A. O., E. Gilbart, "Wet Forming Processes as a Potential Solution to Agglomeration Problems," Advanced Ceramic Processing and Technology, v. 1, pp. 73-93, 1990.
44. Grau, J., Fabrication of Engineered Ceramic Components by the Slurry-Based Three Dimensional Printing Process, Ph.D. Dissertation, Department of Materials Science and Engineering, Massachusetts Institute of Technology, 1998.
45. Asai, Akira, Makota Shioya, Shinichi Hirasawa, and Takeshi Okazaki, *Journal of Imaging Science and Technology*, vol. 37, n. 2, pp. 205-207, 1993.
46. Chandra, S. and C. Avedisian, *Journal of the Royal Society of London A*, vol. 432, pp. 13-41, 1991.
47. Fan, T., Droplet – Powder Impact Interaction in Three Dimensional Printing, Ph.D. Dissertation, Department of Mechanical Engineering, Massachusetts Institute of Technology, 1995.
48. Knezevic, V., Effect of Binder Droplet Placement Strategy on Surface Finish of Fine Ceramic Parts by 3D Printing, MS Thesis, Department of Mechanical Engineering, Massachusetts Institute of Technology, 1998.
49. Arthur, T., Factors Limiting the Surface Finish of Three Dimensional Printed Parts, MS Thesis, Department of Mechanical Engineering, Massachusetts Institute of Technology, 1994.
50. Stow, C., and M Hadfield, *Proceedings of the Royal Society of London A*, vol. 373, pp. 419-441, 1981.
51. Young, R. J., and P. A. Lovell, Introduction to Polymers, 2nd Ed., Chapman and Hall, London, 1991.
52. Incropera, F. P., and D. P. DeWitt, Fundamentals of Heat Transfer, John Wiley and Sons, New York, 1981.
53. Masterson, W. L., and Cecile N. Hurley, Chemistry: Principles and Reactions, Saunders College Publishing, Philadelphia, 1989.
54. Chow, T. S., "Wetting of Rough Surfaces." *Journal of Physics: Condensed Matter*, **10**, pp L445-L451, 1998.
55. Zhou, X. B., and J. Th. M. De Hosson, "Influence of Surface Roughness on the Wetting Angle," *Journal of Materials Research*, **10 [8]**, pp. 1984-1992, 1995.
56. Adamson, A. W., and A. P. Gast, Physical Chemistry of Surfaces, 6th ed., John Wiley and Sons, Inc., New York, 1997.
57. Washburn, E. W., "The Dynamics of Capillary Flow," *The Physical Review*, **XVII [3]**, pp. 273-283, 1921.
58. Marmur, A., "Penetration of a Small Drop into a Capillary," *Journal of Colloid and Interface Science*, **122 [1]**, pp. 209-219, 1988.
59. Denesuk, M., et al., "Capillary Penetration of Liquid Droplets into Porous Materials," *Journal of Colloid and Interface Science*, **158**, pp. 114-120, 1993.
60. Wong, P., "Flow in Porous Media: Permeability and Displacement Patterns," *MRS Bulletin*, pp. 32-38, May 1994

61. Summ, B. D., and V. M. Samsonov, "Concepts of Rehbinder's School and Modern Theories of Spreading," *Colloids and Surfaces A: Physiochemical and Engineering Aspects*, **160**, pp. 63-77, 1999.
62. De Coninck, J., M. J. de Ruijter, and M. Voué, "Dynamics of Wetting," *Current Opinion in Colloid & Interface Science*, **6**, pp. 49-53, 2001.
63. Kistler, S. F., "Hydrodynamics of Wetting," in Surfactant Science Series v. 49: Wettability, J. C. Berg, ed., Marcel Dekker, Inc., New York, 1993.
64. Denesuk, M., et al., "Dynamics of Incomplete Wetting on Porous Materials," *Journal of Colloid and Interface Science*, **168**, pp. 142-151, 1994.
65. Dodge, F. T., "The Spreading of Liquid Droplets on Solid Surfaces," *Journal of Colloid and Interface Science*, **121 [1]**, pp. 154-160, 1988.
66. Summ, B. D., V. S. Yushchenko, and E. D. Shchukin, "Hydrodynamic and Physicochemical Aspects of Spreading," *Colloids and Surfaces*, **27**, pp. 43-55, 1987.
67. Hachisu, S., "Surface Electricity," Surfactant Science Series Volume 15: Electrical Phenomena at Interfaces, Fundamentals, Measurements, and Applications, pp. 3-14, Marcel Dekker, Inc., New York, 1984.
68. Usui, S., "Electrical Double Layer," Surfactant Science Series Volume 15: Electrical Phenomena at Interfaces, Fundamentals, Measurements, and Applications, pp. 15-46, Marcel Dekker, Inc., New York, 1984.
69. Shaw, D. J., Introduction to Colloid & Surface Chemistry, 4th ed., Butterworth-Heinemann Ltd., Oxford, 1992.
70. Hoogeveen, N. G., M. A. C. Stuart, and G. J. Fleer, "Polyelectrolyte Adsorption on Oxides: I. Kinetics and Adsorbed Amounts," *Journal of Colloid and Interface Science*, **182**, pp. 133-145, 1996.
71. Hoogeveen, N. G., M. A. C. Stuart, and G. J. Fleer, "Polyelectrolyte Adsorption on Oxides: II. Reversibility and Exchange," *Journal of Colloid and Interface Science*, **182**, pp. 146-157, 1996.
72. Isrealachvili, J. Intermolecular and Surface Forces with Application to Colloidal and Biological Systems, Academic Press, London, 1985.
73. Netz, R. R., and J.-F. Joanny, "Adsorption of Semiflexible Polyelectrolytes on Charged Planar Surfaces: Charge Compensation, Charge Reversal, and Multilayer Formation," *Macromolecules*, **32 [26]**, pp. 9013-9025, 1999.
74. Vermeer, A. W. P., F. A. M. Leermakers, and L. K. Koopal, "Adsorption of Weak Polyelectrolytes on Surfaces with a Variable Charge: Self-Consistent-Field Calculations," *Langmuir*, **13 [16]**, pp. 4413-4421, 1997.
75. Shubin, V. and P. Linse, "Self-Consistent-Field Modeling of Polyelectrolyte Adsorption on Charge-Regulating Surfaces," *Macromolecules*, **30 [19]**, pp. 5944-5952, 1997
76. Yawen Li, *personal communication.*